Title	Elucidation of Magnetic Relaxation Mechanisms of Four-coordinate Mononuclear Transition Metal Complexes Having Rigid Bidentate Ligands
Author(s)	石崎, 聡晴
Citation	大阪大学, 2020, 博士論文
Version Type	VoR
URL	https://doi.org/10.18910/76378
rights	
Note	

Elucidation of Magnetic Relaxation Mechanisms of Four-Coordinate Mononuclear Transition Metal Complexes Having Rigid Bidentate Ligands

剛直な２座配位子を持つ４配位単核錯体の示す

磁気緩和現象の機構解明

Toshiharu Ishizaki

Department of Chemistry, Graduate School of Science, Osaka University,

Toyonaka, Osaka 560-0043, Japan.

Contents

Chapter 3 The effect of intermolecular interactions on slow magnetic relaxations of a mono-nuclear tetrahedral four-coordinate Cobalt(II) complex with bidentate ligands comprised of pyrrolopyrrole and benzothiazole moieties

3-1 Introduction

3-2 Experimental section

3-3 Results and Discussion

Chapter 4. Synthesis and observations of slow magnetic relaxation phenomena of a tetrahedral four-coordinate mononuclear copper(II) complex consisting of bis-phenyl-bisisoindole-aza-methene ligands

4-1 Introduction

4-2 Experimental Section

4-3 Results and Discussion

Chapter 1

General introduction

1-1 Retention of molecular magnetization in exchange-coupled transition metal clusters

In 1993, Sessoli *et al.* reported the slow magnetic relaxations of paramagnetic dodecanuclear mixed-valence manganese clusters based on the large spin ground state and magnetic anisotropy.[1] After this report, one of these group showed the retention of magnetization after removal of external static magnetic field for order of months at 2.0 K of $[Mn_{12}O_{12}(CH_3COO)_{16}(H_2O)_4]$ (Mn$_{12}$ac, Figure 1-1(a)).[2,3] In addition, the molecule exhibits the quantum mechanical relaxations owing to matching of the energy of spin sublevels (Figure 1-1(b)).[4] Therefore, the phenomena are expected for molecular-based magnets[5] and quantum computings.[6] Since this paramagnetic compound has the ground spin state of $S = 10$ and large easy-axis type of magnetic anisotropy, the two lowest $M_S = \pm 10$ substates are partitioned by a spin reversal barrier expressed as $U = |D|S^2$ (for half-integer systems $U = |D|(S-1/4)^2$), where D is the second-order axial magnetic anisotropy parameter and S is spin quantum number (Figure 1-1(c)). Since the relaxation times analysis indicated that the magnetic relaxations are through the reversal energy barrier U, transition metal clusters with large ground spin were focused.[7-14] Until now, extreme large spin ground states have been reported, for example, an $S = 83/2$ manganese-based cluster $[Mn_{19}(\mu^4\text{-}O)_8(\mu^3,\eta^1\text{-}N_3)_8(HL)_{12}(MeCN)_6]\text{-}Cl_2\cdot10MeOH\cdot MeCN$ (1; H$_3$L=2,6-bis(hydroxymethyl)-4-methyl-phenol)[15] and an $S = 45$ iron-based cluster $[\{Fe(Tp)(CN)_3\}_{24}\{Fe(H_2O)_2\}_6\{Fe(dpp)(H_2O)\}_{12}\cdot6CF_3SO_3]\cdot18H_2O$ (where dpp = 1,3-di(4-pyridyl)propane and Tp = hydrotris(pyrazolyl)borate).[16] Nevertheless, the improvement of the spin reversal barrier had not reported until 2007, for $S = 12$ $[Mn_6O_2(Et\text{-}sao)_6(O_2CPh(Me)_2)_2(EtOH)_6]$,[17] because of the difficulty of achieving large ground spin state and large magnetic anisotropy, simultaneously.
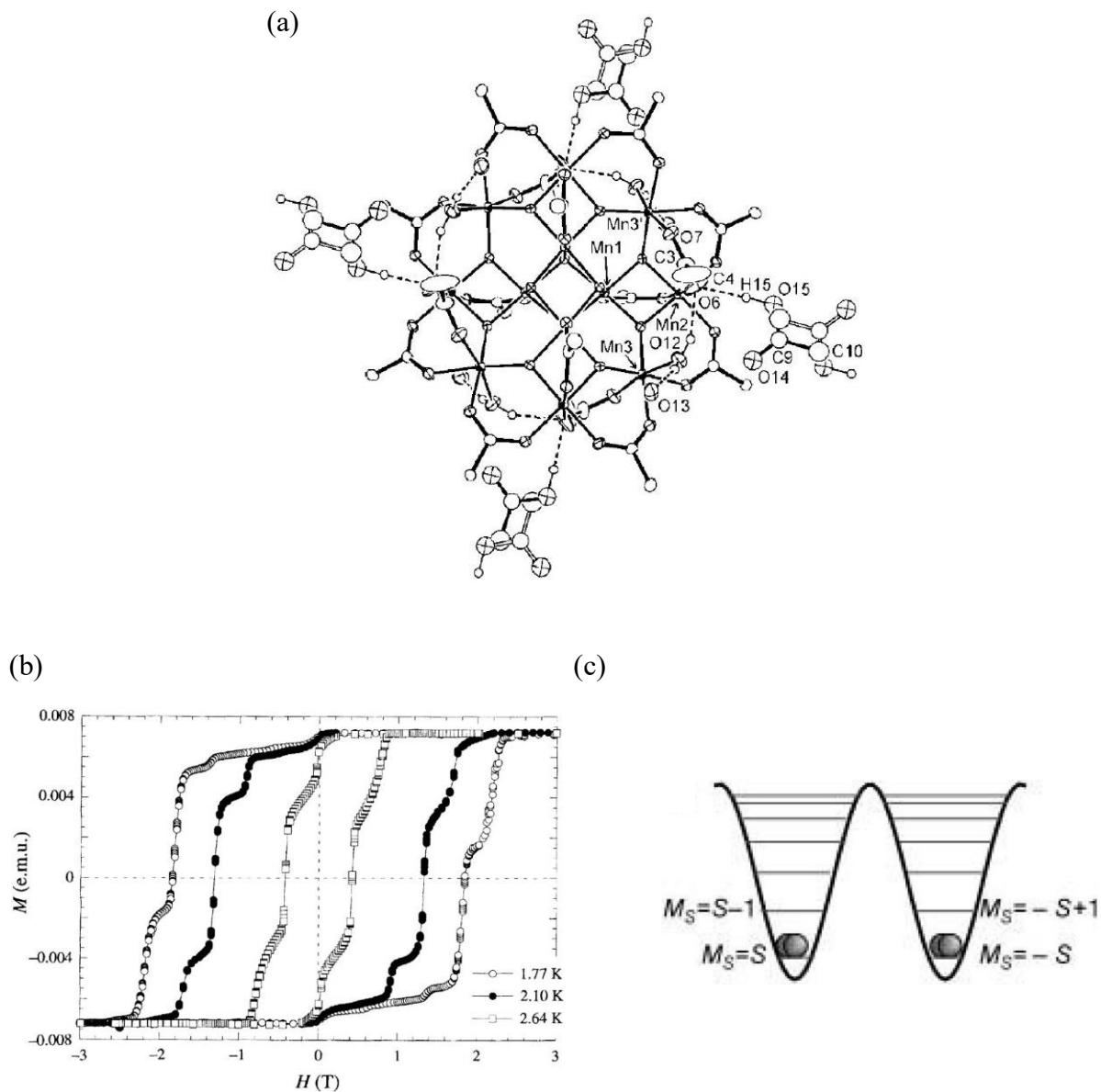
Figure 1-1. (a) Structure of $[Mn_{12}O_{12}(CH_3COO)_{16}(H_2O)_4]$ ($Mn_{12}ac$) and, (b) plot of magnetization vs. magnetic field of $Mn_{12}Ac$ at indicated temperatures and (c) pictorial description for splitting of sublevels of spin states M_S with easy-axis type of magnetic anisotropy of manganese clusters.

1-2 Large magnetic anisotropy and slow magnetic relaxation of mononuclear lanthanide complexes

The electronic states of lanthanide ions can be well-described by using the total angular momentum quantum number, J, rather than the individual L and S due to the large spin−orbit couplings. Ishikawa *et al*, reported the splitting of the sublevels M_J of later lanthanide(III) ions [LnPc$_2$]$^-$, (Ln = Tb, Dy, Ho, Er, Tm or Yb, H$_2$Pc = phthalocyanine) composed of two phthalocyanato ligands (Figure 1-2(a,b)),[18] and some of the complexes with large ground M_J values exhibited the slow magnetic relaxations, and retention of their magnetizations in zero dc field were observed at low temperature (Figure 1-2(c,d)).[19] In the case of [TbPc$_2$]$^-$, the energy gap between the ground and second lowest sublevels $|J_z\rangle = |\pm6\rangle$ and $|\pm5\rangle$, respectively, was estimated to be more than 400 cm^{-1} (Figure 1-2(b)).[18] Since the large $|J_z|$ for the ground states is equivalent to the easy-axis type anisotropy, while the large energy gap between the neighboring $|J_z\rangle$ states is related to the energies required to flip the magnetic moments, [TbPc$_2$]$^-$ shows slow magnetic relaxations at temperatures even higher than 40 K. However, the relaxation time analysis revealed much lower relaxation energy barrier compared with the energy gap, which implies relaxation through real excited states is not dominated in the system even at high temperatures. The discovery of the large magnetic anisotropies of lanthanide-based complexes opened a new way of developing mononuclear complexes that exhibit the slow magnetic relaxation phenomena.[20-22]

Recent progress on Dy(III) complexes having two cyclopentadienyl derivatives have reached the temperature which can retain the magnetization in no applied dc field higher than that of liquid nitrogen owing to the extremely large easy-axis type of magnetic anisotropy of the dysprosium ions.[23-25]
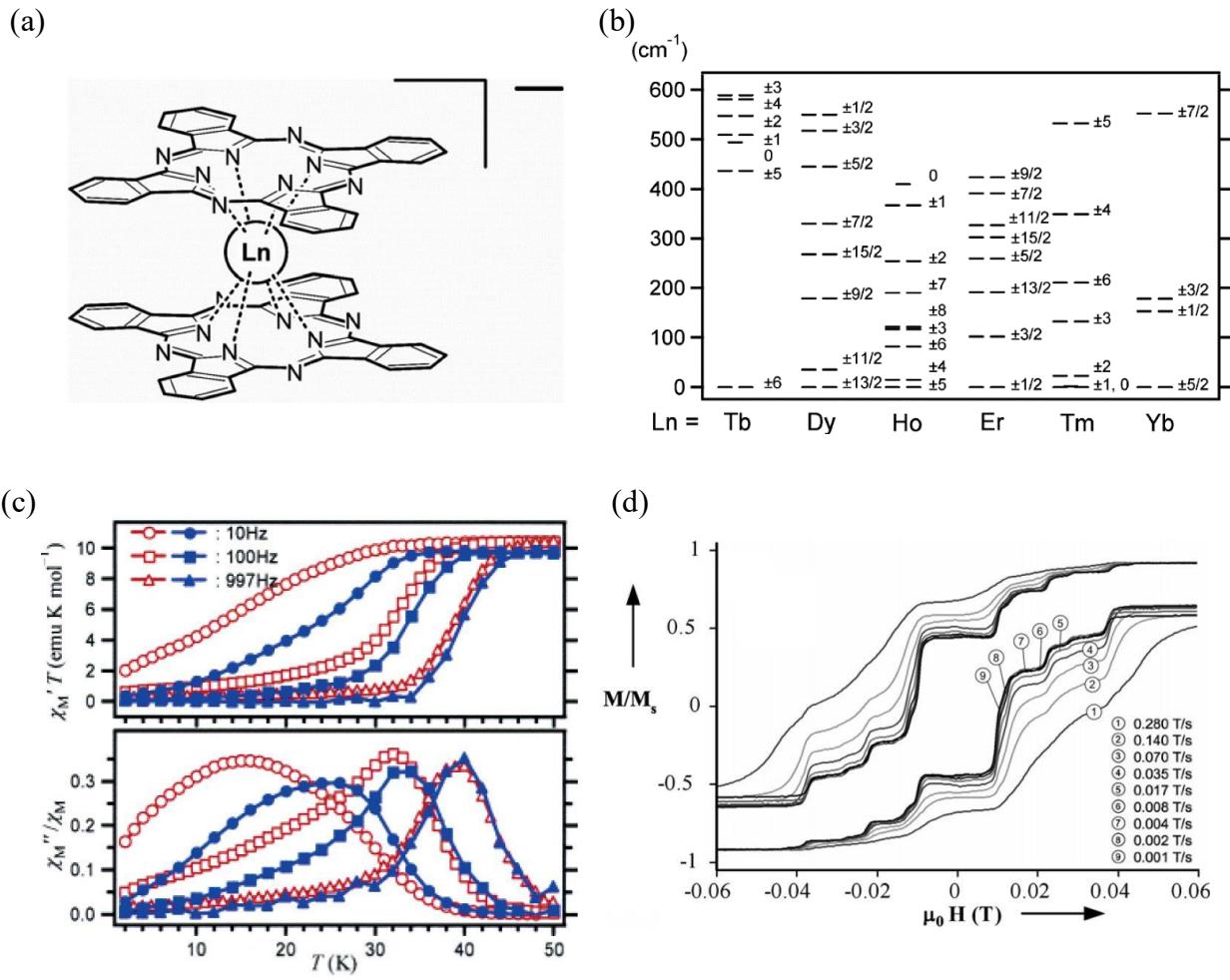
Figure 1-2. (a) Structure of lanthanide phthalocyanato double-decker complex [LnPc$_2$] and (b) splitting of M_J sublevels of a series of later lanthanide(III) complexes in phthalocyanato D_{4d} ligand field. (c) Plots of (top) $\chi_M'T$ and (bottom) χ_M''/χ_M vs. temperature T of [TbPc$_2$]$^-$ (open marks) and [Tb$_{0.02}$Y$_{0.98}$Pc$_2$]$^-$ (filled marks) measured in an oscillating magnetic field of 3.5 Oe at indicated frequencies. (d) Plot of magnetization vs. magnetic field of [Tb$_{0.02}$Y$_{0.98}$Pc$_2$]$^-$ at 0.04 K measured at indicated sweep rates.

1-3 Slow magnetic relaxation of mononuclear transition metal complexes

The concept of the enhancement of magnetic anisotropy of single paramagnetic ion through spin-orbit coupling afforded transition metal based mononuclear complexes that exhibit slow magnetic relaxations.[26-28] Attentions toward mononuclear transition metal complexes stemmed from a mononuclear trigonal pyramidal four-coordination Fe(II) complex reported by Long and coworkers, in which partially remained orbital angular momentum is facilitate the easy-axis type of magnetic anisotropy and exhibited slow magnetic relaxation in a small applied static magnetic field of 1500 Oe (Figure 1-3(a,b)).[29] Since then, various mononuclear systems including Cr(II),[30] Mn(III),[31-34] Fe(I),[35-37] Fe(II),[29,38,39] Fe(III),[40,41] Co(I),[42] Co(II),[43,44] Ni(I),[45] Ni(II)[46] complexes have been reported to exhibit slow magnetic relaxation phenomena. However, most of these need exhibit applied static magnetic fields to observe slow magnetic relaxations, due to the dominant fast quantum tunneling magnetization (QTM) in no applied static magnetic field. In addition, reported effective energy barriers are much smaller than those of the energy difference between the spin sublevels (zero-field splitting). And recently, slow magnetic relaxations on $S = 1/2$ systems are reported,[45,47] despite no accessible reversal energy barriers even at room temperature. For that reasons, the rationalizations of slow magnetic relaxation phenomena have not been fully achieved yet.
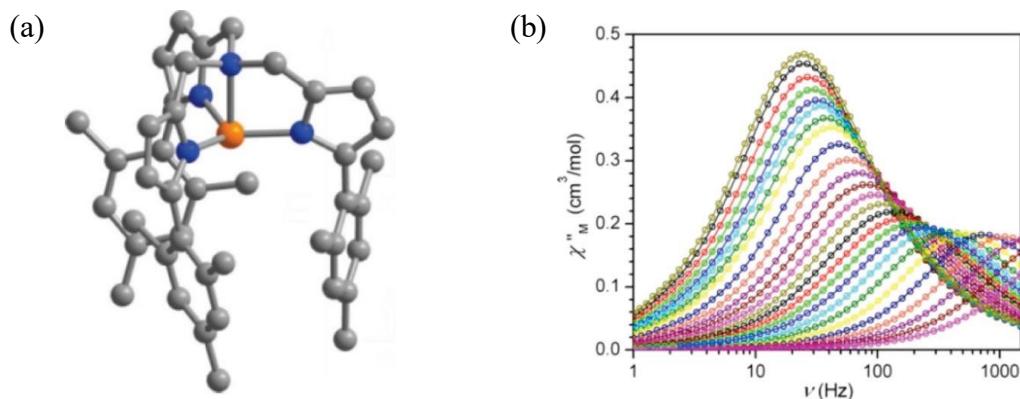
Figure 1-3. (a) Structure of [Fe(tpa^{Mes})]$^-$ and (b) ac frequency dependence out-of-phase magnetic susceptibilities collected in an applied static field of 1500 Oe between 1.8 – 6.0 K.

1-4 Magnetic relaxations of paramagnetic ions

Since 1930s, magnetic relaxations of paramagnetic salts have been studied both experimentally and theoretically.[48] The spin-lattice relaxations are explained through the energy exchange between the spin systems and lattice vibrations for relaxing the magnetizations, and several processes are known.[49] The direct process dominate at low temperature is occurs through the creation and annihilation of a photon simultaneously. The relaxation process exhibits significant static magnetic field dependence expressed $\tau^{-1} \propto H^5 \coth(g\mu_B H/2k_B T)$, where H and T are magnetic field and absolute temperature, respectively. The Raman process dominate at relatively high temperature occurs through absorbing a phonon and excite to the vibration state. The rate of the process is followed exponential dependence on absolute temperature ($\tau^{-1} \propto T^n$, where n are coefficient of Raman process, and for Kramers systems theoretically $n = 9$). The Orbach process dominate at higher temperatures occur through the excitation to excited states by absorbing a photon. The relaxation process follows the Arrhenius behavior proportional to by $\tau^{-1} \propto \exp(\Delta E/kT)$.

As mentioned in chapter 1-1, the quantum tunneling of magnetization (QTM) relaxation mechanism have also been observed. The quantum mechanical relaxations are occurred through the mixing the populated quantum states and is facilitated through intermolecular dipolar interaction, transverse anisotropy of molecules (E) and hyperfine interactions between electronic and nuclear spins.[8, 50] The first is reduced by isolation of the paramagnetic molecules, for example, magnetic dilution by diamagnetic analogues. In addition, the mixing through the transvers anisotropy is theoretically forbidden in Kramers systems, therefore, half-integer spin systems are expected for good candidates to observe the slow magnetic relaxations.[50]

1-5 This thesis

In this dissertation, the structures, static and dynamic magnetic properties of three four-coordinate mononuclear first-row transition metal complexes comprised of rigid bidentate ligands are reported, and the mechanisms of these magnetic relaxation behaviors are discussed in detail.

In chapter 2, the synthesis and magnetic properties of a tetrahedral four-coordinate mononuclear Co(II) complex comprised of bisisoindole-aza-methene ligands [Co(half-Pc)$_2$] (**1**) are reported. The complex exhibited the slow magnetic relaxation even in no applied static magnetic field, and the magnetic anisotropy arise from the splitting between the $M_S = \pm 3/2$ and $\pm 1/2$ substates is unambiguously determined by the high-field, multi-frequency electron spin resonance (ESR) measurements. The magnetic relaxation mechanisms are discussed through the comparison between the zero-field splitting and the spin relaxation energy barrier.

In chapter 3, the dynamic magnetic properties of a tetrahedral four-coordinate mononuclear Co(II) complex comprised of bidentate ligands synthesized through the dehydration reactions of pyrrolopyrrole and benzothiazole moieties [Co(L)$_2$] (**2**) that have intermolecular hydrogen-bond networks through heteroatoms of the ligands are reported. The complex **2** exhibited slow magnetic relaxations in applied static magnetic field, and the effect of intermolecular interactions on magnetic relaxations were investigated through comparing ac signals of magnetically diluted **2**. In addition, the relaxation mechanisms of molecular **2** were considered by the fitting of relaxation times of investigated entire temperature and static field by Orbach, Raman and direct spin-lattice relaxation processes and quantum tunneling process.

In chapter 4, the dynamic magnetic relaxations of $S = 1/2$ tetrahedral four-coordinate Cu(II) mononuclear complex with bis-pheyl-bisisoindole-aza-methene ligands [Cu(half-Pc$_{Ph}$)$_2$] (**3**) are

reported. This complex exhibited slow magnetic relaxations only in an applied static magnetic field. For $S = 1/2$ systems, because there are no accessible excited states for spin inversions, Orbach relaxation process is not expected. The relaxation times were considered by employing spin-lattice direct, Raman and quantum tunneling processes.

1-6 References

1. Sessoli, R.; Gatteschi, D.; Caneschi, A.; Novak, M. A. Magnetic bistability in a metal-ion cluster. *Nature* 1993, 365, 141−143.

2. Sessoli, R.; Tsai, H.-L.; Schake, A. R.; Wang, S.; Vincent, J. B.; Folting, K.; Gatteschi, D.; Christou, G.; Hendrickson, D. N. High-Spin Molecules: [$Mn_{12}O_{12}(O_2CR)_{16}(H_2O)_4$]. *J. Am. Chem. Soc.* **1993**, *115*, 1804-1816.

3. Lis, T. Preparation, Structure, and Magnetic Properties of a Dodecanuclear Mixed-Valence Manganese Carboxylate. *Acta Cryst. B*, **1980**, *36*, 2042-2046.

4. Thomas, L.; Lionti, F.; Ballou, R.; Gatteschi, D.; Sessoli, R.; Barbara, B. Macroscopic quantum tunnelling of magnetization in a single crystal of nanomagnets. *Nature* **1993**, *383*, 145-147.

5. Sessoli, R. Single-atom data storage. *Nature* **2017**, *543*, 189-190.

6. Ladd, T. D.; Jelezko, F.; Laflamme, R.; Nakamura, Y.; Monroe, C.; O'Brien, J. L. *Nature Quantum computers*. **2010**, *464*, 45-53.

7. Oshio, H.; Hoshino, N.: Ito, T. Superparamagnetic Behavior in an Alkoxo-Bridged Iron(II) Cube. *J. Am. Chem. Soc.* **2000**, *122*, 12602-12603.

8. Gatteschi, D.; Sessoli, R. Quantum Tunneling of Magnetization and Related Phenomena in Molecular Materials. *Angew. Chem. Int. Ed.* **2003**, *42*, 268-297.

9. Oshio, H.; Hoshino, N.; Ito, T.; Nakano, M. Single-Molecule Magnets of Ferrous Cubes: Structurally Controlled Magnetic Anisotropy. *J. Am. Chem. Soc.* **2004**, *126*, 8805-8812.

10. Yang, E.-C.; Hendrickson, D. N.; Wernsdorfer, W.; Nakano, M.; Zakharov, L. N.; Sommer, R. D.; Rheingold, A. L.; Ledezma-Gairaud, M.; Christou, G. Cobalt single-molecule magnet. *J. Appl. Phys.* **2002**, *91*, 7382-7384.

11. Magnetization Density in an Iron(III) Magnetic Cluster. A Polarized Neutron Investigation. *J. Am. Chem. Soc.* **1999**, *121*, 5342-5343.

12. Single-Molecule Magnet Behavior of a Tetranuclear Iron(III) Complex. The Origin of Slow Magnetic Relaxation in Iron(III) Clusters. *J. Am. Chem. Soc.* **1999**, *121*, 5302-5310.

13. Sañudo, E. C.; Wernsdorfer, W.; Abboud, K. A.; Christou, G. Synthesis, Structure, and Magnetic Properties of a Mn_{21} Single-Molecule Magnet. *Inorg. Chem.* **2004**, *43*, 4137-4144.

14. Cadiou, C.; Murrie, M.; Paulsen, C.; Villar, V.; Wernsdorfer, W.; Winpenny, R. E. P. Studies of a nickel-based single molecule magnet: resonant quantum tunnelling in an $S = 12$ molecule. *Chem. Commun.* **2001**, *24*, 2666-2667

15. Ako, A. M.; Hewitt, I. J.; Mereacre, V.; Clérac, R.; Wernsdorfer, W.; Anson, C. E.; Powell, A. K. A Ferromagnetically Coupled Mn_{19} Aggregate with a Record $S=83/2$ Ground Spin State. *Angew. Chem.* **2006**, *118*, 5048 –5051.

16. Kang, S.; Zheng, H.; Liu, T.; Hamachi, K.; Kanegawa, S.; Sugimoto, K.; Shiota, Y.; Hayami, S.; Mito, M.; Nakamura, T.; Nakano, M.; Baker, M. L.; Nojiri, H.; Yoshizawa, K.; Duan, C.; Sato, O. A ferromagnetically coupled Fe_{42} cyanide-bridgednanocage. *Nat. Commun.* **2015**, *6*, 5955.

17. Milios, C. J.; Vinslava, A.; Wernsdorfer, W.; Moggach, S.; Parsons, S.; Perlepes, S. P.; Christou, G.; Brechin, E. K. A Record Anisotropy Barrier for a Single-Molecule Magnet. *J. Am. Chem. Soc.* **2007**, *129*, 2754-2755.

18. Ishikawa, N.; Sugita, M; Tomoko, O.; Tanaka, N.; Iino, T.; Kaizu, Y. Determination of Ligand-Field Parameters and f-Electronic Structures of Double-Decker Bis(phthalocyaninato)lanthanide Complexes. *Inorg. Chem.,* **2003,** *42*, 2440-2446.

19. Ishikawa, N.; Sugita, M.; Ishikawa, T.; Koshihara, S.; Kaizu, Y. Lanthanide Double-Decker Complexes Functioning as Magnets at the Single-Molecular Level. *J. Am. Chem. Soc.*, **2003**, *125*, 8694-8695.

20. Woodruff, D. N.; Winpenny, R. E. P.; Layfield, R. A. Lanthanide Single-Molecule Magnets. *Chem. Rev.* **2013**, *113*, 5110−5148.

21. Layfield, R. A. Organometallic Single-Molecule Magnets. *Organometallics* **2014**, *33*, 1084−1099.

22. Feltham, H. L. C.; Brooker, S. Review of purely 4f and mixed-metal nd-4f single-molecule magnets containing only one lanthanide ion. *Coord. Chem. Rev.* **2014**, *276*, 1−33.

23. Guo, F.-S.; Day, B. M.; Chen, Y.-C.; Tong, M.-L.; Mansikkamäki, A.; Layfield. R. A. A Dysprosium Metallocene Single-Molecule Magnet Functioning at the Axial Limit. *Angew. Chem. Int. Ed.*, **2017**. *56*. 11445-11449.

24. Goodwin, C. A. P.; Ortu, F.; Reta, D.; Chilton, N. F.; Mills, D. P. *Nature*, Molecular magnetic hysteresis at 60 kelvin in dysprosocenium. **2017**, *548*, 439-442.

25. Guo, F.-S.; Day, B. M.; Chem, Y.-C.; Tong, M.-L.; Mansikkamäki, A.; Layfield. R. A. Magnetic hysteresis up to 80 kelvin in a dysprosium metallocene single-molecule magnet. *Science*, **2018**, *362*, 1400-1403.

26. Craig, G. A.; Murrie, M. 3d single-ion magnets. *Chem. Soc. Rev.*, **2015**, *44*, 2135-2147.

27. Frost, J. M.; Harriman, K. L. M.; Murugesu, M. The rise of 3-d single-ion magnets in molecular magnetism: towards materials from molecules? *Chem. Soc.*, 2016, 7, 2470-2491.

28. Feng, M.; Tong. M. -L. Single Ion Magnets from 3d to 5f: Developments and Strategies. *Chem. Eur. J.*, **2018**, *24*, 7574-7594.

29. Freedman, D. E.; Harman, W. H.; Harris, T. D.; Long, G. J.; Chang, C. J.; Long. J. R. Slow Magnetic Relaxation in a High-Spin Iron(II) Complex. *J. Am. Chem. Soc.*, 2010, **132**, 1224-1225.

30. Deng, Y.-F.; Han, T.; Wang, Z.; Ouyang, Z.; Yin, B.; Zheng, Z.; Krzystek, J.; Zheng, Y.-Z. Uniaxial magnetic anisotropy of square planar chromium(II) complexes revealed by magnetic and HF-EPR studies. *Chem. Commun.* **2015**, *51*, 17688−17691.

31. Ishikawa, R.; Miyamoto, R.; Nojiri, H.; Breedlove, B. K.; Yamashita, M. Slow Relaxation of the Magnetization of an Mn^{III} Single Ion. *Inorg. Chem.* **2013**, *52*, 8300−8302.

32. Sato, R.; Suzuki, K.; Minato, T.; Shinoe, M.; Yamaguchi, K.; Mizuno, N. Field-induced slow magnetic relaxation of octahedrally coordinated mononuclear Fe(III)-, Co(II)-, and Mn(III)-containing polyoxometalates. *Chem. Commun.* **2015**, *51*, 4081−4084.

33. Chen, L.; Wang, J.; Liu, Y.-Z.; Song, Y.; Chen, X.-T.; Zhang, Y.- Q.; Xue, Z.-L. Slow Magnetic Relaxation in Mononuclear Octahedral Manganese(III) Complexes with Dibenzoylmethanide Ligands. *Eur. J. Inorg. Chem.* **2015**, 271−278.

34. Pascual-Álvarez, A.; Vallejo, J.; Pardo, E.; Julve, M.; Lloret, F.; Krzystek, J.; Armentano, D.; Wernsdorfer, W.; Cano, J. Field-Induced Slow Magnetic Relaxation in a Mononuclear Manganese(III)-Porphyrin Complex. *Chem. - Eur. J.* **2015**, *21*, 17299−17307.

35. Zadrozny, J. M.; Xiao, D. J.; Atanasov, M.; Long, G. J.; Grandjean, F.; Neese, F.; Long, J. R. Magnetic blocking in a linear iron(I) complex. *Nat. Chem.* **2013**, *5*, 577−581.

36. Werncke, C. G.; Bunting, P. C.; Duhayon, C.; Long, J. R.; Bontemps, S.; Sabo-Etienne, S. Two-Coordinate Iron(I) Complex [Fe{N(SiMe$_3$)$_2$}$_2$]$^-$: Synthesis, Properties, and Redox Activity. *Angew. Chem., Int. Ed.* **2015**, *54*, 245−248.

37. Samuel, P. P.; Mondal, K. C.; Amin Sk, N.; Roesky, H. W.; Carl, E.; Neufeld, R.; Stalke, D.; Demeshko, S.; Meyer, F.; Ungur, L. Chibotaru, L. F.; Christian, J.; Ramachandran, V.; van Tol, J.; Dalal, N. S. Electronic Structure and Slow Magnetic Relaxation of Low-Coordinate Cyclic Alkyl(amino) Carbene Stabilized Iron(I) Complexes. *J. Am. Chem. Soc.* **2014**, *136*, 11964−11971.

38. Feng, X.; Mathonière, C.; Jeon, I.; Rouzières, M.; Ozarowski, A.; Aubrey, M. L.; Gonzalez, M. I.; Cl'erac, R.; Long, J. R. Tristability in a Light-Actuated Single-Molecule Magnet. *J. Am. Chem. Soc.* **2013**, *135*, 15880-15884.

39. Zadrozny, J. M.; Atanasov, M.; Bryan, A. M.; Lin, C.-Y.; Rekken, B. D.; Power, P. P.; Neese, F.; Long, J. R. Slow magnetization dynamics in a series of two-coordinate iron(II) complexes. *Chem. Sci.* **2013**, *4*, 125−138.

40. Mossin, S.; Tran, B. L.; Adhikari, D.; Pink, M.; Heinemann, F. W.; Sutter, J.; Szilagyi, R. K.; Meyer, K.; Mindiola, D. J. A Mononuclear Fe(III) Single Molecule Magnet with a 3/2↔5/2 Spin Crossover. *J. Am. Chem. Soc.* **2012**, *134*, 13651−13661.

41. Feng, X.; Hwang, S. J.; Liu, J.-L.; Chen, Y.-C.; Tong, M.-L.; Nocera, D. G. Slow Magnetic Relaxation in Intermediate Spin $S = 3/2$ Mononuclear Fe(III) Complexes. *J. Am. Chem. Soc.* **2017**, *139*, 16474−16477.

42. Meng, Y.-S.; Mo, Z.; Wang, B.-W.; Zhang, Y.-Q.; Deng, L.; Gao, S. Observation of the single-ion magnet behavior of d^8 ions on two coordinate Co(I)−NHC complexes. *Chem. Sci.* **2015**, *6*, 7156−7162.

43. Jurca, T.; Farghal, A.; Lin, P.; Korobkov, I.; Murugesu, M.; Richeson, D. S. Single-Molecule Magnet Behavior with a Single Metal Center Enhanced through Peripheral Ligand Modifications. *J. Am. Chem. Soc.* **2011**, *133*, 15814-15817.

44. Habib, F.; Luca, O. R.; Vieru, V.; Shiddiq, M.; Korobkov, I.; Gorelsky, S. I. Takase, M. K.; Chibotaru, L. F.;, Hill, S.; Crabtree, R. H.; Murugesu, M. Influence of the ligand field on slow magnetization relaxation versus spin crossover in mononuclear cobalt complexes. *Angew. Chem. Int. Ed.* **2013**, *52*, 11290-11293.

45. Poulten, R. C.; Page, M. J.; Algarra, A. G.; Le Roy, J. J.; López, I.; Carter, E.; Llobet, A.; Macgregor, S. A.; Mahon, M. F.; Murphy, D. M.; Murugesu, M.; Whittlesey, M. K. Synthesis, Electronic Structure, and Magnetism of $[Ni(6\text{-}Mes)_2]^+$: A Two-Coordinate Nickel(I) Complex Stabilized by Bulky N-Heterocyclic Carbenes. *J. Am. Chem. Soc.* **2013**, *135*, 13640−13643.

46. Miklovič, J.; Valigura, D.; Boča, R.; Titiš, J. A mononuclear Ni(II) complex: a field induced single-molecule magnet showing two slow relaxation processes. *Dalton Trans.* **2015**, *44*, 12484−12487.

47. W. Lin, T. Bodenstein, V. Mereacre, K. Fink, A. Eichhöfer. Field-Induced Slow Magnetic Relaxation in the Ni(I) Complexes $[NiCl(PPh_3)_2]\cdot C_4H_8O$ and $[Ni(N(SiMe_3)_2)(PPh_3)_2]$. *Inorg. Chem.* **2016**, *55*, 2091−2100.

48. Vleck, J. H. V. Paramagnetic Relaxation Times for Titanium and Chrome Alum. *Pys. Rev.* **1940**, 57, 426-447.

49. Vroomen, A. C. D.; Lijphart, E. E.; Poulis, N. J. Electron spin-lattice relaxation of Cu^{++} in zinc ammonium tutton salt. *Pysica* **1970**, *47*, 458-484.

50. Zadrozny, M.; Long. J. R. Slow Magnetic Relaxation at Zero Field in the Tetrahedral Complex $[Co(SPh)_4]^{2-}$. *J. Am. Chem. Soc.*, **2011**, *133*, 20732-20734.

Chapter 2

Synthesis and determination of slow magnetic relaxation phenomena of a tetrahedral four-coordinate mononuclear cobalt(II) complex comprised of bisisoindole-aza-methene ligands

2-1 Introduction

2-1-1 Mononuclear transition metal complexes that show slow magnetic relaxation under no applied static field

Despite various mononuclear first-row transition metal complexes have been reported, most of these need an applying static magnetic field to observe the slow magnetic relaxations due to the fast quantum tunneling of magnetization (QTM) in an absence of applied static field.[1-3] In 2013, a tetrahedral four-coordinate Co(II) complex (PPh$_4$)$_2$[Co(SPh)$_4$] was firstly reported to exhibit the slow magnetic relaxations even in the absence of applied static field in mononuclear transition metal complexes, which utilize half-integer spin $S = 3/2$ and second-order spin-orbit coupling.[4] So far, trigonal prismatic six-coordinate Co(II),[5-8] pseudo-octahedral six-coordinate Co(II),[9] pseudo-tetrahedral four-coordinate Co(II)[4,10-17] and linear two-coordinate Fe(I)[18,19] and Co(II)[20,21] complexes have been reported to exhibit the phenomena in no applied static magnetic fields.

Interestingly, the relaxation energy barriers of these mononuclear complexes are considerably smaller than the axial zero-field splitting (ZFS) energy.[1-3] For example, the absolute value of the axial ZFS parameter $|D|$ of a series of four-coordinate Co(II) complexes, (PPh$_4$)$_2$[Co(XPh)$_4$], where X = O, S, or Se, increases with increasing the size of the X (-11, -62, and -83 cm^{-1} for X = O, S, and Se, respectively), although the experimentally estimated relaxation energy barriers are less sensitive to the $|D|$ value (ca. 20 cm^{-1} for any X's).[10] However, the relationship between the $|D|$ value and the relaxation energy barrier is still unclear.

2-1-2 High-field, multi-frequency electron spin resonance (ESR)

To get better understanding on magnetic relaxations, the magnetic anisotropy of molecules is very important. In transition metal clusters, the second-order axial and rhombic anisotropic parameters D and E are generally determined through electron spin resonance (ESR) measurements using sub-THz light.[22,23] Nevertheless, the method is no longer valid in mononuclear systems with large magnetic anisotropy arising from large spin-orbit couplings.[11] In most cases, their anisotropies have been determined by static magnetic measurements only.[1-3] However, the method is less not sensitive to both the sign and magnitude of the axial anisotropic parameter.[23] Recently, the determinations of anisotropic parameters of mononuclear systems through high-field, multi-frequency ESR measurements are reported.[23-26] However, the determinations of anisotropy parameters by using several THz light have not been reported.

2-1-3 Bisisoindole-aza-methene ligands

Fukuda and coworkers reported the novel mono- and multi-nuclear complexes composed of the bisisoindole-aza-methene (half-Pc) skeltons which synthesized through the reactions of 1,2-dicyanobennzene and alkoxide formed in the mixture of lithium and alcohol solutions in moderate conditions.[27-29] The half-Pc structure has high rigidity and planarity due to the π-conjugated isoindole dimer bridged by a nitrogen atom. The coordination geometries are dependent on metal source. The mononuclear Cu(II) and Ni(II) complexes have square-planer coordination geometries on central metal ions, while the Co(II) and Zn(II) ions are expected to form the favorable tetrahedral four-coordination geometries with the ligands.

2-2 Experimental section

2-2-1 Synthesis of [Co(half-Pc)$_2$], **1**

  1,2-dicyanobenzene (2.0 g, 15.6 mmol) was added to dry methanol solution (70 mL) of Li (250 mg) and refluxed for 10 min under an argon atmosphere. Cobalt(II) dichloride (420 mg, 3.24 mmol) was added to the yellow reaction mixture, and further refluxed for 40 min. The resultant orange precipitate was filtrated and purified by silica gel column chromatography (eluent: CH$_2$Cl$_2$ / MeOH = 40 : 1 (v/v) to give pure **1** as an orange powder in 11.3% yield. MS (ESI): m/z: 698.18018 [CoC$_{36}$H$_{30}$N$_8$O$_4$] + H$^+$. Anal. Calcd (%) for C$_{36}$H$_{30}$N$_8$O$_4$Co: C 61.98, H 4.33, N 16.06. Found: C 61.87, H 4.34, N 15.91.

2-2-2 Synthesis of [Zn(half-Pc)$_2$]

1,2-dicyanobenzene (2.0 g, 15.6 mmol) was added to dry methanol solution (70 mL) of Li (250 mg) and refluxed for 10 min under an argon atmosphere. Zinc(II) dichloride (450 mg, 3.30 mmol) was added to the yellow reaction mixture, and further refluxed for 40 min. The resultant yellowish green precipitate was filtrated and purified by recrystallization to give [Zn(half-Pc)$_2$] in 49.8% yield. MS(ESI) m/z [ZnC$_{36}$N$_8$H$_{30}$O$_4$] + H$^+$: 703.17524.

2-2-3 Preparation of [Co$_{0.03}$Zn$_{0.97}$(half-Pc)$_2$], **dil.1**

A mixture of **1** and [Zn(half-Pc)$_2$] in the molar ratio of 3 : 97 was dissolved in CH$_2$Cl$_2$ and passed through a celite column. The eluent was collected, concentrated in vacuo and dried under reduced pressure at 50 °C for 1 day.

2-2-4 Measurements

Absorption spectra were measured by a SHIMAZU UV-1650PC spectrometer at room temperature. Elemental analysis was performed by a YANACO CHN Corder MT-6 analyzer. Mass spectra were obtained using a Thermo Fisher Scientific Orbitrap XL (ESI-LIT-orbitrap) spectrometer. Single crystal X-ray diffractions were collected with a Rigaku R-AXIS VII diffractometer using filtered Mo Kα ($\lambda = 0.71075$ Å) radiation. The refinement with full-matrix least-squares techniques was carried out with SHELXL-2014/7.[31]

Static magnetic properties were collected by a Quantum Design MPMS-XL7AC SQUID magnetometer. The sample was prepared by wrapping 6.96 mg (9.98×10^{-6} mol) of **1** in an aluminum foil of 40.97 mg and fixed by eicosane (12.4 mg). Diamagnetic components were estimated using the Pascal constants,[32] and the contribution from the aluminum foil was corrected on the basis of the blank measurement. Ac measurements were performed by Quantum Design MPMS-XL7AC and PPMS-9 magnetometers for the low (0.1-1340 Hz) and high (100-10000 Hz) frequency range, respectively. Oscillating magnetic fields of 3.9 Oe (MPMS) and 5 Oe (PPMS) were employed. The undiluted sample was prepared by fixing 18.8 mg of **1** in a gelatin capsule using eicosane. The diluted sample was prepared by fixing 133.4 mg of **dil.1** in a plastic straw using eicosane.

High-field, multi-frequency ESR measurements were performed on a locally developed system at the Center for Advanced High Magnetic Field Science (AHMF), Osaka University, in which a 55 T short pulsed magnet and an Edinburgh far-infrared laser were equipped with a magnetically tuned InSb detector and a homemade transmission-type cryostat. Measurements were performed in the frequency range between 0.584 and 2.522 THz in pulsed magnetic fields of up to 55 T with a duration of 6 ms. The sample was prepared by adding powder of **1** into a cylindrical Teflon container (2 mm in diameter and 3 mm in length). 1,1-Diphenyl-2-picrylhydrazyl (DPPH) radical was employed as an ESR standard ($g \approx 2.0023$).

Ab initio quantum calculations were conducted on the ORCA 4.0 program package.[33-35] The resolution of identity (RI) approximation technique was employed with the def2-TZVPP basis set and def2/JK auxiliary basis set implemented in ORCA. The complete active space self-consistent field (CASSCF) calculations were performed on specified seven active electrons in five Co-based 3d orbitals. For state interaction calculations, 10 quartets and 35 doublets were included. Dynamic correlations were recovered by N-electron valence state perturbation theory (NEVPT2).

2-3 Results and Discussion

2-3-1 Synthesis and characterizations

  The preparation of **1** is followed by the generation of half-Pc ligand which is formed by the reaction of 1,2-dicyanobenzen and lithium methoxide in dry methanol at 70 °C. Since the free half-Pc ligand was unstable, cobalt(II) chloride was added to the reaction mixture directly (**Scheme 1**). The orange residue was chromatographed by a short silica gel column to give the pure complex. The absorption spectrum of **1** dissolved in CH_2Cl_2 is depicted in Figure 2-1. Characteristic peaks in the visible range (600-800 nm) known as the Q-band of pthalocyanines were not observed, suggesting the lack of large cyclic π-conjugation on the ligands.
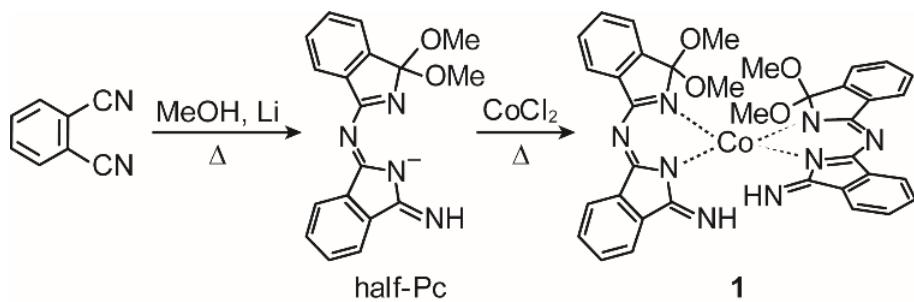
Scheme 1. Synthesis of [Co(half-Pc)$_2$] (**1**).
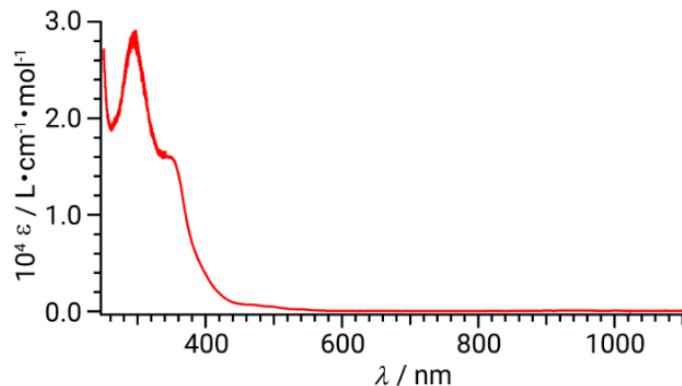
Figure 2-1. Absorption spectrum of **1** in CH_2Cl_2.

Single crystals of **1** were prepared by slow diffusion of hexane into the CH_2Cl_2 solution of **1**. The complex is composed of a cobalt ion and two half-Pc ligands, in which the half-Pc consists of two isoindole moieties bridged by a nitrogen atom (Figure 2-2). The terminal part of the ligand has either one nitrogen or two methoxy groups. The cobalt(II) atom is coordinated by four isoindole nitrogens of the two half-Pc ligands, and the two half-Pc ligands are arranged almost perpendicular to each other to render the pseudotetrahedral coordination geometry. The two half-Pcs are crystallographically equivalent, and **1** has the 2-fold rotation axis. No counterions are found in the crystals, suggesting the cobalt ion is divalent, and the complex is neutral in total. The Co1-N1 and Co1-N3 bond lengths are 1.9773(12) and 1.9750(15) Å, respectively. The N1−Co1−N3 angle of 91.02(5)° is smaller than that of the ideal tetrahedral coordination (109.5°), while the N1−Co1−N1′ and N3−Co1−N3′ angles are wider (129.66(6)° and 110.01(6)°, respectively), indicating that the rigid nature of the half-Pc ligand effectively distorts the coordination geometry from the ideal tetrahedron to give pseudotetragonal ligand fields. As a consequence, the coordination sites around the cobalt are elongated along the bisector of the N1−Co1−N3 angle. The intermolecular π−π interactions are observed between the benzene rings in the crystals. The shortest Co−Co distance in the crystals is 8.1997(2) Å (Figure 2-3).
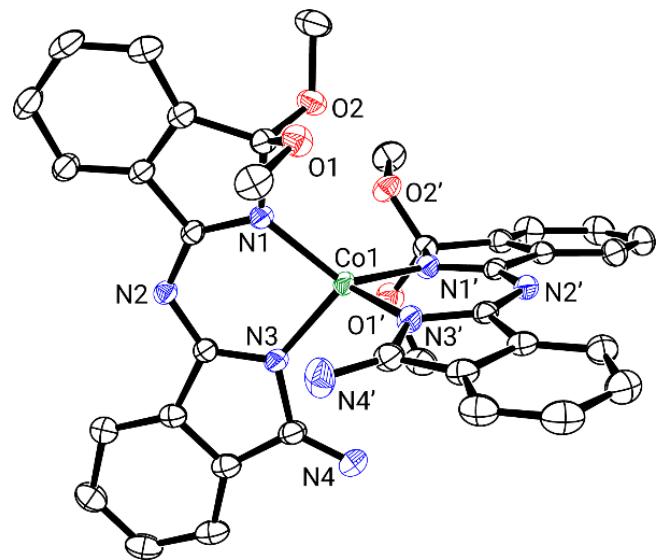
Figure 2-2. Ortep diagram of **1** (50% ellipsoids). Hydrogen atoms are omitted for clarity.
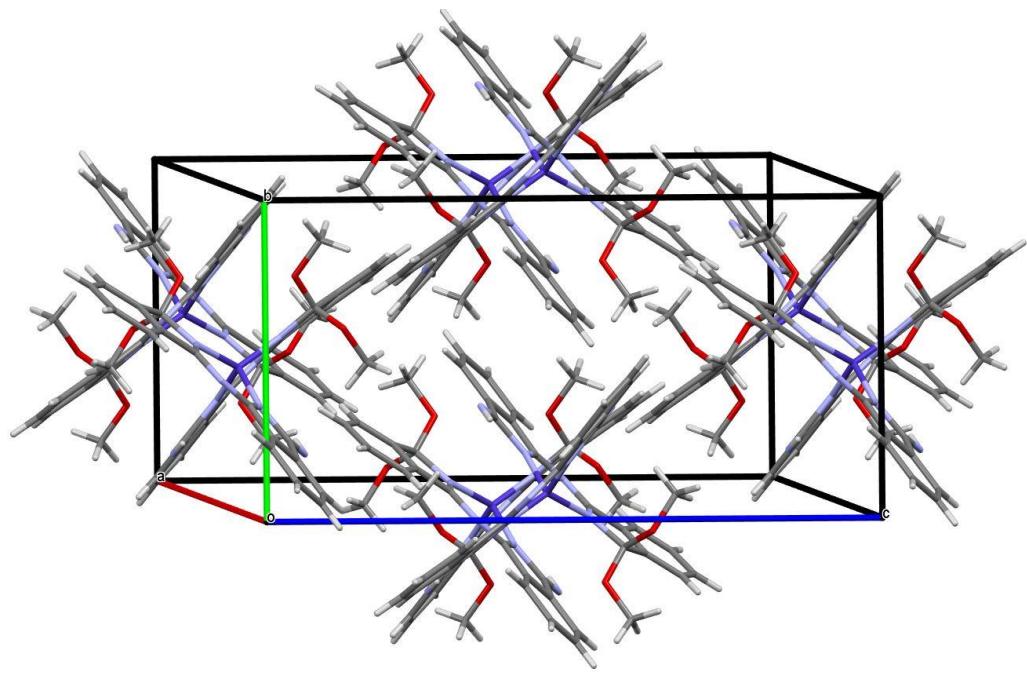
Figure 2-3. Crystal packing and intermolecular π-π interactions among **1** molecules.

25

Table 2-1. Selected crystal structural parameters for [Co(half-Pc)$_2$] (**1**) and [Zn(half-Pc)$_2$].

	[Co(half-Pc)$_2$], **1**	[Zn(half-Pc)$_2$]
Empirical Formula	C$_{36}$H$_{30}$CoN$_8$O$_4$	C$_{36}$H$_{30}$ZnN$_8$O$_4$
Formula Weight	697.62	704.06
Crystal System	*monoclinic*	*monoclinic*
a / Å	16.2676(5)	16.3467(3)
b / Å	10.1081(3)	10.0762(3)
c / Å	19.290(2)	19.263(2)
β / °	103.214(7)	103.214(7)
V / Å^3	3088.0(4)	3088.9(4)
Space Group	*I*2/*a* (No.15)	*I*2/*a* (No.15)
Z value	4	4
D_{calc}/ g cm^{-3}	1.500	1.514
Temperature / °C	−73.0	−73.0
No. of Observations	3526	3530
R_1	0.0350	0.0355
wR_2	0.0871	0.1077

Table 2-2. Bond lengths for **1**.

Co1-N1	1.9773(12)	O1-C17	1.433(2)
Co1-N3	1.9750(15)	O2-C18	1.428(2)
O1-C1	1.3878(19)	N1-C8	1.326(2)
O2-C1	1.411(2)	N2-C9	1.3272(19)
N1-C1	1.485(2)	N3-C16	1.423(2)
N2-C8	1.342(2)	C1-C2	1.529(2)
N3-C9	1.344(2)	C2-C7	1.382(3)
N4-C16	1.267(2)	C4-C5	1.384(3)
C2-C3	1.385(2)	C6-C7	1.382(2)
C3-C4	1.393(3)	C9-C10	1.472(2)
C5-C6	1.390(3)	C10-C15	1.387(2)
C7-C8	1.475(2)	C12-C13	1.390(3)
C10-C11	1.383(2)	C14-C15	1.384(3)
C11-C12	1.391(3)	C13-C14	1.389(3)
C15-C16	1.478(3)		

Table 2-3. Bond angles for **1**.

N1-Co1-N1′	129.66(6)	N1-Co1-N3	91.02(5)
N1-Co1-N3′	118.04(6)	N1′-Co1-N3	118.04(6)
N1′-Co1-N3′	91.02(5)	N3-Co1-N3′	110.01(6)
C1-O1-C17	115.46(13)	C1-O2-C18	115.42(14)
Co1-N1-C1	127.77(10)	Co1-N1-C8	122.98(11)
C1-N1-C8	109.21(12)	C8-N2-C9	121.69(13)
Co1-N3-C9	123.87(11)	Co1-N3-C16	127.98(11)
C9-N3-C16	108.15(14)	O1-C1-O2	106.13(13)
O1-C1-N1	105.34(13)	O1-C1-C2	115.87(13)
O2-C1-N1	111.60(13)	O2-C1-C2	113.44(14)
N1-C1-C2	104.26(13)	C1-C2-C3	132.25(17)
C1-C2-C7	107.45(14)	C3-C2-C7	120.19(15)
C2-C3-C4	117.73(18)	C3-C4-C5	121.58(17)
C4-C5-C6	120.74(17)	C5-C6-C7	117.13(17)
C2-C7-C6	122.61(15)	C2-C7-C8	107.84(14)
C6-C7-C8	129.45(16)	N1-C8-N2	130.43(14)
N1-C8-C7	111.22(14)	N2-C8-C7	118.27(13)
N2-C9-N3	128.86(16)	N2-C9-C10	120.82(14)
N3-C9-C10	110.25(13)	C9-C10-C11	130.99(14)
C9-C10-C15	107.03(15)	C11-C10-C15	121.95(16)
C10-C11-C12	117.01(15)	C11-C12-C13	121.25(18)
C12-C13-C14	121.25(19)	C13-C14-C15	117.50(16)
C10-C15-C14	121.04(17)	C10-C15-C16	106.64(15)
C14-C15-C16	132.30(16)	N3-C16-N4	126.24(18)
N3-C16-C15	107.87(13)	N4-C16-C15	125.87(17)

symmetry code : -x + 0.5, y, -z + 1

Table 2-4. Bond lengths for [Zn(half-Pc)$_2$].

Zn1-N1	1.9915(14)	O1-C17	1.429(3)
Zn1-N3	1.9904(18)	O2-C18	1.433(3)
O1-C1	1.385(2)	N1-C8	1.324(2)
O2-C1	1.412(3)	N2-C9	1.320(2)
N1-C1	1.485(3)	N3-C16	1.416(3)
N2-C8	1.350(3)	C1-C2	1.524(3)
N3-C9	1.346(2)	C2-C7	1.388(3)
N4-C16	1.251(3)	C4-C5	1.382(4)
C2-C3	1.385(3)	C6-C7	1.383(3)
C3-C4	1.397(3)	C9-C10	1.475(3)
C5-C6	1.393(3)	C10-C15	1.387(3)
C7-C8	1.475(2)	C12-C13	1.395(3)
C10-C11	1.382(3)	C14-C15	1.385(3)
C11-C12	1.394(3)	C13-C14	1.387(4)
C15-C16	1.481(3)		

Table 2-5. Bond angles for [Zn(half-Pc)₂].

N1-Zn1-N1′	128.47(6)	N1-Zn1-N3	91.46(6)
N1-Zn1-N3′	117.54(7)	N1′-Zn1-N3	117.54(7)
N1'-Zn1-N3′	91.46(6)	N3-Zn1-N3′	111.72(7)
C1-O1-C17	115.66(16)	C1-O2-C18	115.21(18)
Zn1-N1-C8	127.94(12)	Zn1-N1-C8	122.54(13)
C1-N1-C8	109.51(14)	C8-N2-C9	121.94(16)
Zn1-N3-C9	123.00(13)	Zn1-N3-C16	128.54(14)
C9-N3-C16	108.46(17)	O1-C1-O2	106.00(17)
O1-C1-N1	105.59(15)	O1-C1-C2	116.04(16)
O2-C1-N1	111.31(15)	O2-C1-C2	113.60(16)
N1-C1-C2	104.08(16)	C1-C2-C3	132.5(2)
C1-C2-C7	107.70(16)	C3-C2-C7	119.67(18)
C2-C3-C4	117.8(2)	C3-C4-C5	121.9(2)
C4-C5-C6	120.5(2)	C5-C6-C7	117.1(2)
C2-C7-C6	122.97(17)	C2-C7-C8	107.50(16)
C6-C7-C8	129.44(19)	N1-C8-N2	130.60(16)
N1-C8-C7	111.18(17)	N2-C8-C7	118.15(16)
N2-C9-N3	129.69(18)	N2-C9-C10	120.27(16)
N3-C9-C10	109.97(15)	C9-C10-C11	131.14(16)
C9-C10-C15	107.09(17)	C11-C10-C15	121.76(19)
C10-C11-C12	117.31(18)	C11-C12-C13	120.8(2)
C12-C13-C14	121.4(2)	C13-C14-C15	117.44(19)
C10-C15-C14	121.2(2)	C10-C15-C16	106.51(18)
C14-C15-C16	132.26(18)	N3-C16-N4	125.4(2)
N3-C16-C15	107.93(16)	N4-C16-C15	126.7(2)

symmetry code : -x + 0.5, y, -z + 1

2-3-2 Static magnetic properties

The temperature dependence of $\chi_M T$ products on powder of **1** is plotted in Figure 2-4. The values remain almost constant between 300 to 100 K (2.37 cm³ K mol⁻¹ at 300 K). The value is larger than the spin-only value for high spin Co(II) (S=3/2) of 1.875 cm³ K mol⁻¹, and the isotropic g value is 2.25. This indicates the additional factor other than spin component. The $\chi_M T$ values decrease below 50 K and reach 1.61 cm³ K mol⁻¹ at 1.8 K. This is due to the anisotropic character of the Co ion in **1**. Magnetization vs. magnetic field (M-$\mu_0 H$) plot shows no hysteresis loops and no remnant magnetization at zero static field were observed even at 1.8 K (Figure 2-5).
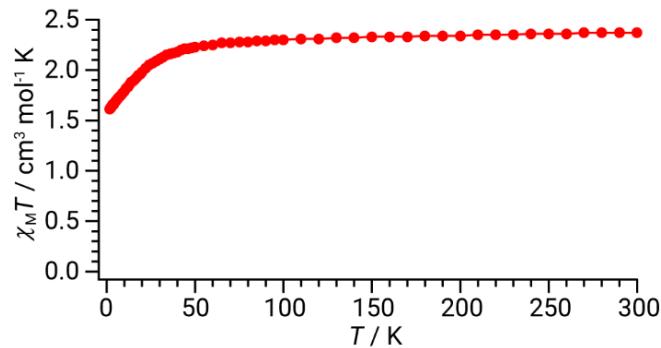

Figure 2-4. Temperature dependence of $\chi_M T$ products between 300 to 1.8 K of **1**.
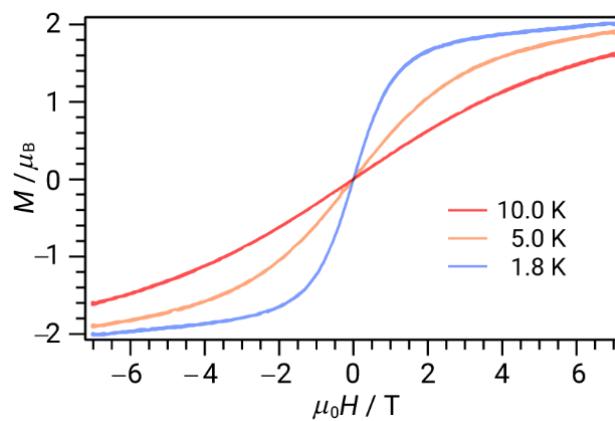
Figure 2-5. Magnetization (M) vs. magnetic field ($\mu_0 H$) plot of **1**.

The M vs HT^{-1} plot shows dispersions at each temperature, which means the presence of a large magnetic anisotropy on the cobalt site of **1** (Figure 2-6). In order to extract anisotropic parameters, the plot was fitted by the following anisotropic spin Hamiltonian:

$$\hat{H} = g\mu_B \mathbf{S} \cdot \mathbf{H} + D\left\{\hat{S}_z^2 + \frac{1}{3}S(S+1)\right\} + E\left(\hat{S}_x^2 - \hat{S}_y^2\right)$$

where g was assumed to be isotropic and collinear with the D tensor in order to avoid overparameterization. μ_B, D, E are Bohr magneton, the axial and rhombic ZFS parameters, respectively. $\mathbf{H}$ and $\mathbf{S}$ are vectors of magnetic field and spin angular momentum operators, and $\hat{S}_x$, $\hat{S}_y$ and $\hat{S}_z$ are spin angular momentum operators in notated directions. The best fit was obtained by the following parameters; $g = 2.30$, $D = -27.9$ cm^{-1}, $|E| = 0.002$ cm^{-1}. The negative D indicates that **1** has a large axial magnetic anisotropy, while nearly zero $|E|$ value indicates negligible rhombic anisotropy. As mentioned above, the anisotropic parameters are not sensitive to magnetic properties, therefore, these anisotropic parameters are uniquely determined through spectroscopic ESR measurements.
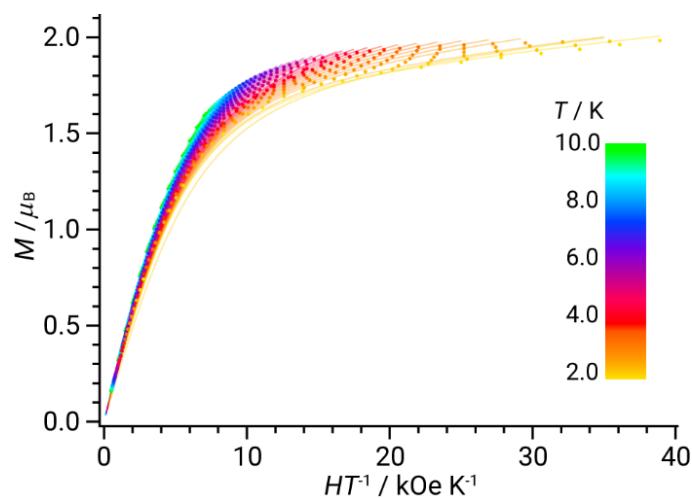
Figure 2-6. $M - \mu_0 HT^{-1}$ plot and fitting curves using the anisotropic parameters in the text.

2-3-3 Dynamic magnetic properties

In order to investigate the slow magnetic relaxations, temperature dependence of ac magnetic susceptibility measurements in ac frequency of 1000, 100, 10 and 1 Hz was observed for **1** and **dil.1** (Figure 2-7). In the absence of applied static magnetic field, the χ'' signals are significant in the ac frequencies higher than 10 Hz, and the obscure shoulders appear at ca. 5.6 and 4.8 K for 1000 and 100 Hz, respectively (Figure 2-7(a)). In the temperature range higher than 8 K, no χ'' signals were observed even at 1000 Hz. With decreasing the temperature at 1000 Hz, both the χ' and χ'' values start to rise gradually and take the highest values at 1.8 K.

When the static magnetic field of 1000 Oe was applied, distinct temperature dependencies were observed (Figure 2-7(b)). Maxima of χ'' were observed at 5.8, 5.0, 4.2 and 3.8 K in the ac frequency for 1000, 100, 10 and 1 Hz, respectively. At 1.8 K, both the χ' and χ'' values are almost zero at 1000 and 100 Hz, while those at 1 Hz are still non-negligible. These observations indicate that although the magnetic relaxations are effectively slowed down by the external magnetic field, other decay paths seem to be still significant.

In order to inspect the effects of the intermolecular interactions, a magnetically diluted solid solution, $[Co_{0.03}Zn_{0.97}(half-Pc)_2]$ (**dil.1**) was prepared. The temperature-dependent relaxation behaviors of **dil.1** differ drastically compared to that of undiluted **1** (Figure 2-7(c)). The clear peaks appeared even in the absence of static field. The peak temperatures approximately coincide with those observed in **1** in applied static field of 1000 Oe, and therefore, the magnetic relaxations in **1** in no applied static field can be ascribed mainly to the intermolecular interactions among the **1** molecules.
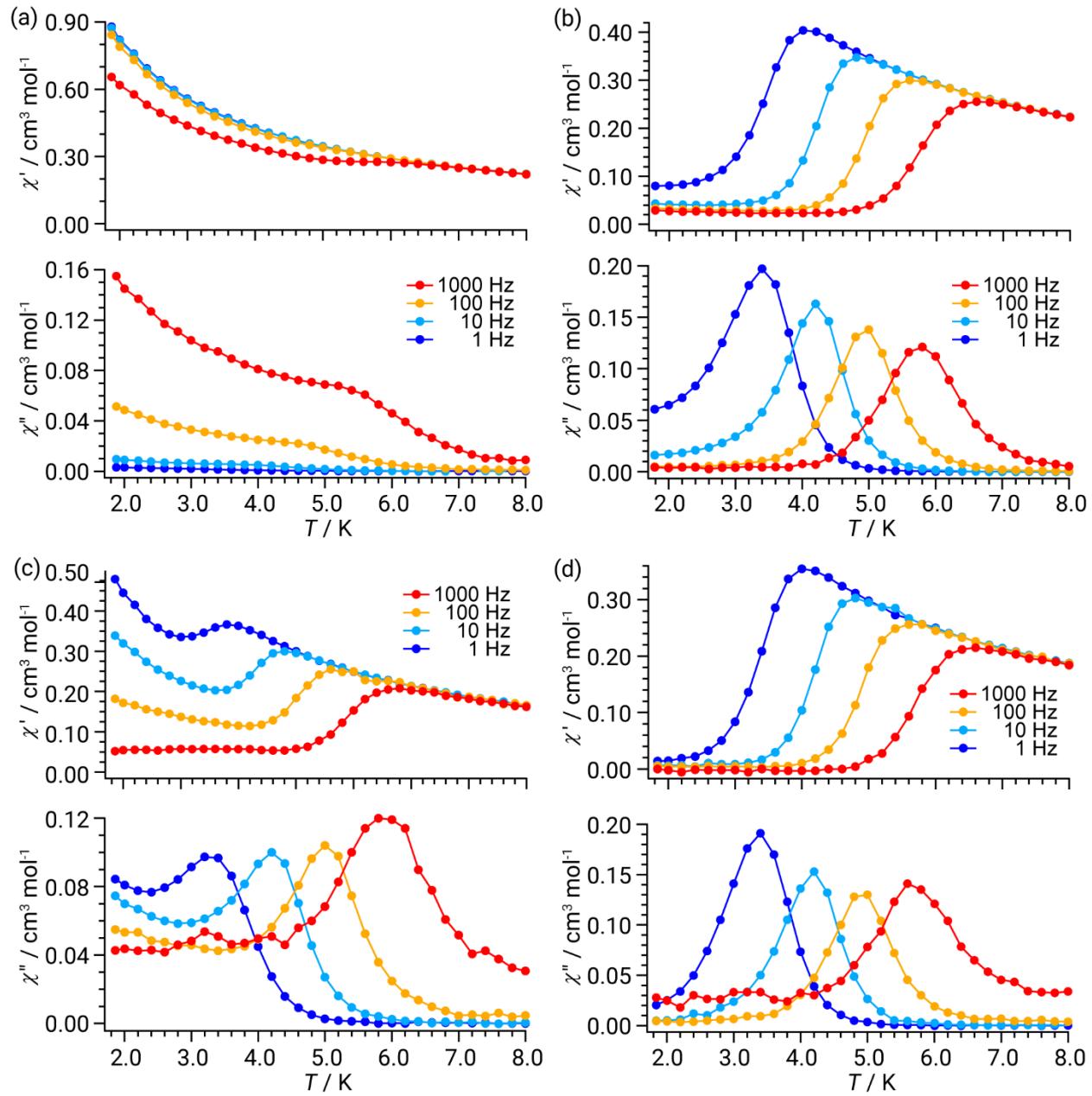
Figure 2-7. Temperature dependence of χ' and χ'' for **1** (a) in no applied static field and (b) in applied static field of 1000 Oe, and for **dil.1** in (c) in no applied static field and (d) in applied static field of 1000 Oe.

34

These facts suggest that the magnetic relaxations dominating in the low-temperature range are not suppressed by reducing the interactions among the Co(II) ions; i.e., the observed relaxations are of intramolecular origin. Application of the static field of 1000 Oe to **dil.1** gives no significant alterations of the peak temperature, while it leads to clear convergence of both the χ' and χ'' values at 1.8 K (Figure 2-7(d)). The observed static field dependencies at low temperatures strongly suggest that these magnetic relaxations arise from the QTMs.

In order to evaluate the relaxation times, the frequency dependence of the ac magnetic susceptibilities of **dil.1** in no applied static magnetic field and an applied static field of 1000 Oe were collected (Figure 2-8). At temperatures higher than 2 K, clear peak frequencies are recognized in no applied static field. The peaks shift to the high frequency side with increasing the temperature and transcend the experimental window (10000 Hz) at 7.5 K. In an applied static field of 1000 Oe, peaks of χ'' were observed between 7.0 – 3.0 K, (Figure 2-9). The experimental data were fitted by using the generalized Debye model (Figure 2-10, 2-11) The fitting parameters are listed in Table 2-6, 2-7, 2-8 and 2-9.
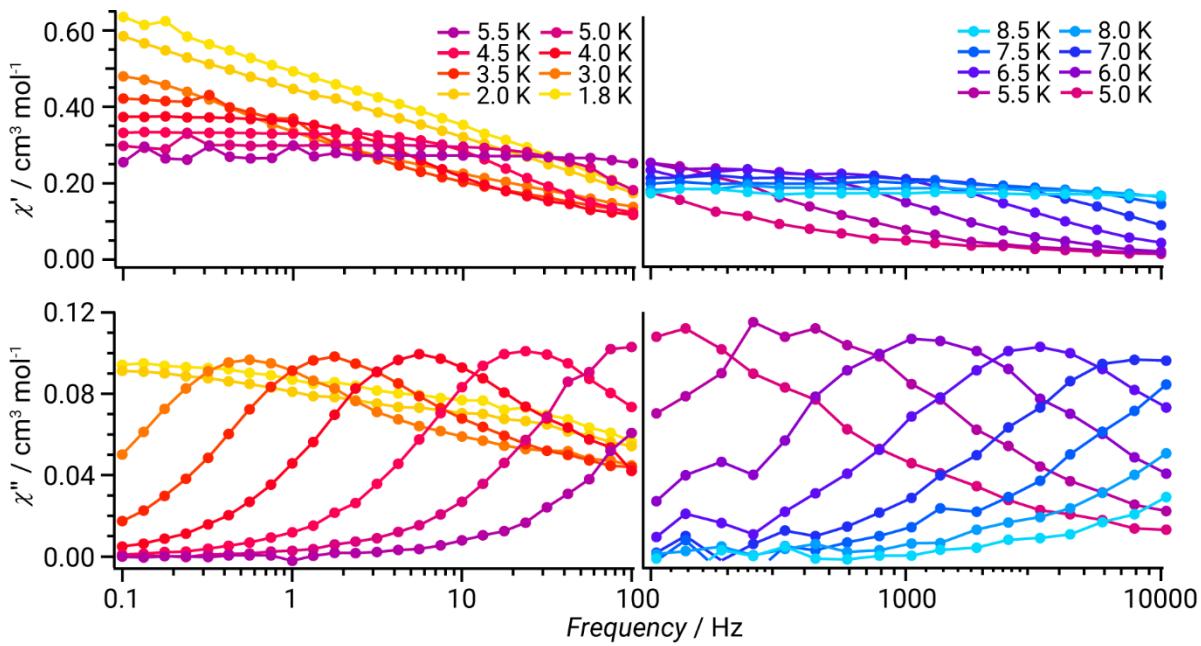
Figure 2-8. Frequency dependence of χ' and χ'' for **dil.1** in no applied static field.
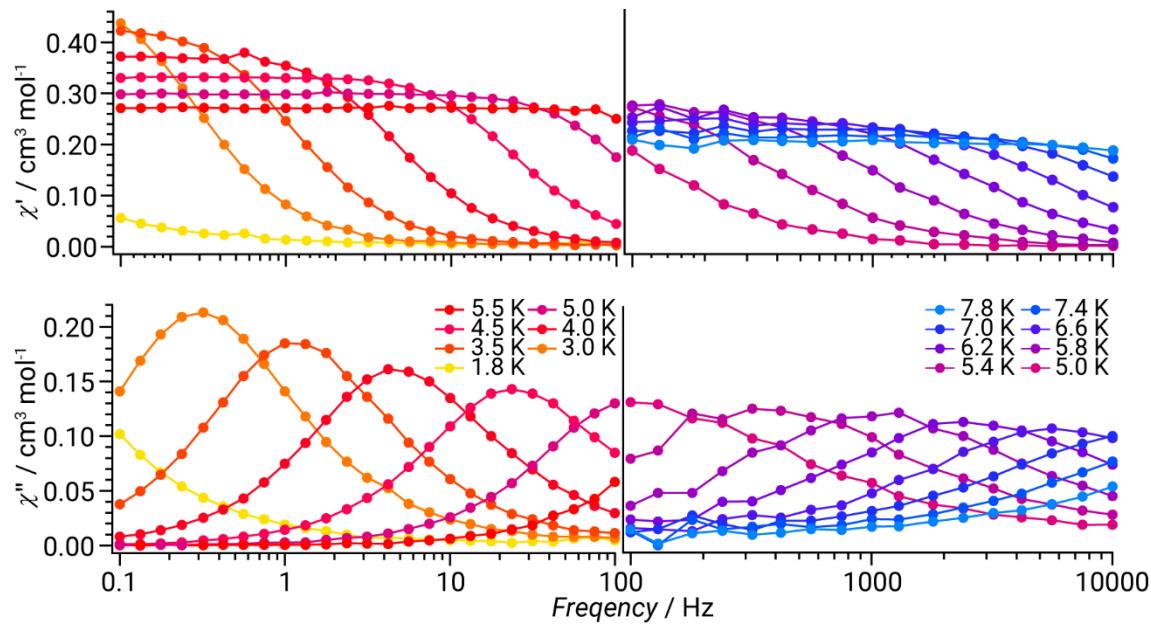
Figure 2-9. Frequency dependence of χ' and χ'' plots for **dil.1** in applied static field of 1000 Oe.

Generalized Debye model:

$$\chi'(\omega) = \chi_S + (\chi_T - \chi_S)\frac{1 + (\omega\tau)^{1-\alpha}\sin(\pi\alpha/2)}{1 + 2(\omega\tau)^{1-\alpha}\sin(\pi\alpha/2) + (\omega\tau)^{2-2\alpha}}$$

$$\chi''(\omega) = (\chi_T - \chi_S)\frac{(\omega\tau)^{1-\alpha}\cos(\pi\alpha/2)}{1 + 2(\omega\tau)^{1-\alpha}\sin(\pi\alpha/2) + (\omega\tau)^{2-2\alpha}}$$

χ_T : isothermal magnetic susceptibility, χ_S : adiabatic magnetic susceptibility

α : dispersion coefficient, τ : relaxation time
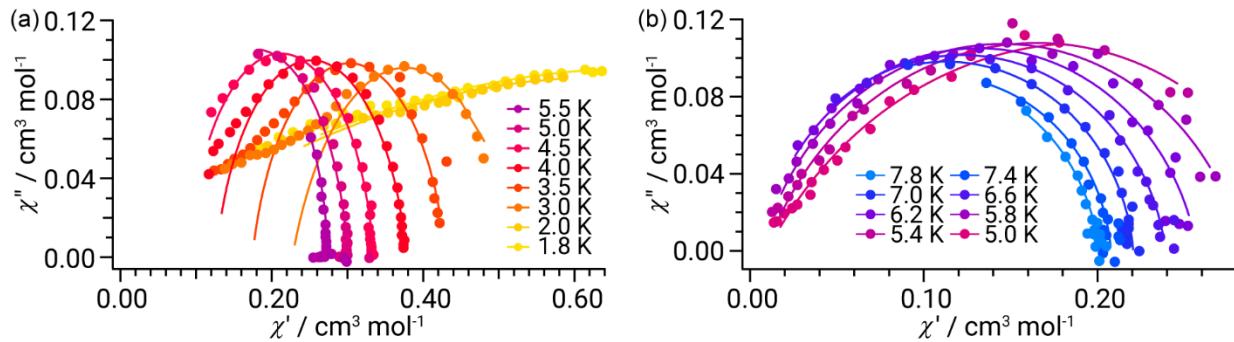
Figure 2-10. Cole-Cole plots for **dil.1** in no applied static field measured by (a) MPMS and (b) PPMS.
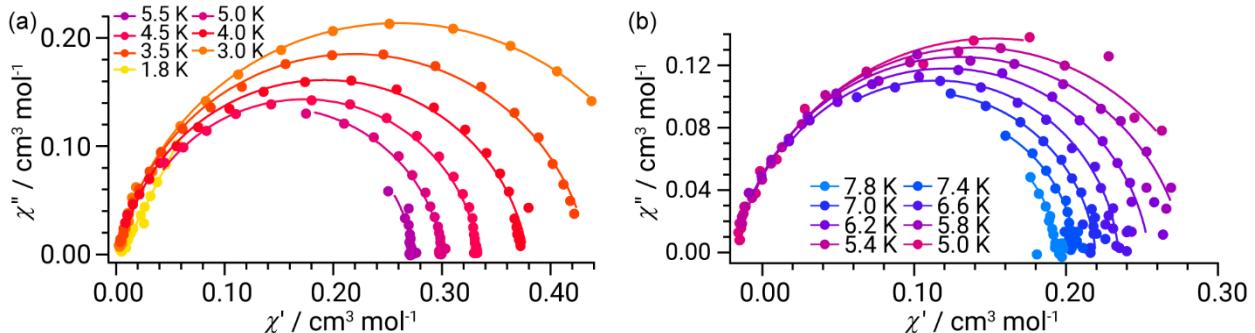
Figure 2-11. Cole-Cole plots for **dil.1** in an applied static field of 1000 Oe measured by (a) MPMS and (b) PPMS.

Table 2-6. Fitting parameters for **dil.1** in an absence of static field measured by PPMS.

T / K	χ_t / cm^3 mol^{-1}	χ_s / cm^3 mol^{-1}	α	τ / s
8.0	0.19	0.0080	0.059	5.09×10^{-6}
7.9	0.19	0.0071	0.057	5.68×10^{-6}
7.8	0.20	-0.0013	0.071	7.10×10^{-6}
7.7	0.20	-0.0025	0.070	7.05×10^{-6}
7.6	0.20	0.0050	0.053	8.56×10^{-6}
7.5	0.21	-0.012	0.073	8.75×10^{-6}
7.4	0.21	0.012	0.053	1.18×10^{-5}
7.3	0.21	0.015	0.047	1.41×10^{-5}
7.2	0.21	0.020	0.011	1.71×10^{-5}
7.1	0.22	0.0073	0.069	1.78×10^{-5}
7.0	0.22	0.0052	0.059	2.08×10^{-5}
6.9	0.23	0.0060	0.068	2.50×10^{-5}
6.8	0.23	0.0067	0.068	2.93×10^{-5}
6.7	0.23	-0.0021	0.099	3.28×10^{-5}
6.6	0.24	0.0051	0.090	4.09×10^{-5}
6.5	0.24	0.0037	0.085	4.75×10^{-5}
6.4	0.25	0.0061	0.083	5.82×10^{-5}
6.3	0.25	0.0052	0.099	7.00×10^{-5}
6.2	0.26	0.0057	0.11	8.64×10^{-5}
6.1	0.26	0.0047	0.13	1.04×10^{-4}
6.0	0.27	0.0013	0.16	1.32×10^{-4}
5.9	0.27	0.0079	0.14	1.59×10^{-4}
5.8	0.28	0.0070	0.16	2.06×10^{-4}

5.7	0.29	0.0083	0.17	2.58×10^{-4}
5.6	0.30	0.0072	0.20	3.42×10^{-4}
5.5	0.30	0.0081	0.19	4.13×10^{-4}
5.4	0.32	0.0093	0.23	5.69×10^{-4}
5.3	0.34	0.010	0.25	7.70×10^{-4}
5.2	0.35	0.011	0.26	1.01×10^{-3}
5.1	0.37	0.011	0.30	1.43×10^{-3}
5.0	0.38	0.010	0.32	1.91×10^{-3}

Table 2-7. Fitting parameters for **dil.1** in absence of static field measured by MPMS.

T / K	χ_t / cm^3 mol^{-1}	χ_s / cm^3 mol^{-1}	α	τ / s
5.5	0.27	0.036	0.059	4.40×10^{-4}
5.4	0.28	0.026	0.079	5.20×10^{-4}
5.3	0.28	0.028	0.095	6.63×10^{-4}
5.2	0.29	0.031	0.10	8.36×10^{-4}
5.1	0.29	0.039	0.11	1.08×10^{-3}
5.0	0.30	0.054	0.10	1.49×10^{-3}
4.9	0.31	0.060	0.091	2.06×10^{-3}
4.8	0.31	0.065	0.094	2.75×10^{-3}
4.7	0.32	0.076	0.087	3.78×10^{-3}
4.6	0.33	0.0081	0.097	4.96×10^{-3}
4.5	0.33	0.089	0.11	6.39×10^{-3}
4.4	0.34	0.099	0.15	9.04×10^{-3}
4.3	0.35	0.11	0.093	1.20×10^{-2}
4.2	0.36	0.11	0.13	1.49×10^{-2}
4.1	0.37	0.12	0.13	1.98×10^{-2}
4.0	0.38	0.13	0.15	2.52×10^{-2}
3.8	0.38	0.13	0.13	4.36×10^{-2}
3.5	0.43	0.17	0.17	8.48×10^{-2}
3.2	0.46	0.19	0.21	1.68×10^{-1}
3.0	0.53	0.23	0.27	2.81×10^{-1}
2.7	0.60	0.20	0.43	4.88×10^{-1}
2.4	0.80	0.17	0.64	1.41
2.2	0.82	0.21	0.63	1.39
2.0	1.3	0.00080	0.82	4.58
1.8	1.4	-0.027	0.83	5.20

Table 2-8. Parameters obtained from the fitting procedures for **dil.1** at H_{dc} = 1000 Oe in the temperature range of 8.0 - 5.0 K measured by the PPMS.

T / K	χ_t / cm^3 mol^{-1}	χ_s / cm^3 mol^{-1}	α	τ / s
8.0	0.19	0.048	0.00052	4.64×10^{-6}
7.8	0.19	0.042	0.00048	5.81×10^{-6}
7.6	0.20	−0.012	0.084	4.94×10^{-6}
7.4	0.21	0.014	0.044	8.26×10^{-6}
7.2	0.21	0.0034	0.052	1.03×10^{-5}
7.0	0.22	−0.0048	0.057	1.37×10^{-5}
6.8	0.23	−0.0094	0.065	1.86×10^{-5}
6.6	0.23	−0.0050	0.052	2.79×10^{-5}
6.4	0.24	−0.0088	0.066	4.05×10^{-5}
6.2	0.26	−0.013	0.081	5.97×10^{-5}
6.0	0.26	−0.017	0.095	9.13×10^{-5}
5.8	0.28	−0.018	0.11	1.49×10^{-4}
5.6	0.29	−0.019	0.12	2.48×10^{-4}
5.4	0.30	−0.017	0.11	4.11×10^{-4}
5.2	0.31	−0.017	0.13	7.27×10^{-4}
5.0	0.32	−0.0018	0.14	1.35×10^{-3}

Table 2-9. Parameters obtained from the fitting procedures for **dil.1** at H_{dc} = 1000 Oe in the temperature range of 5.5 - 1.8 K measured by the MPMS.

T / K	χ_t / cm³ mol⁻¹	χ_s / cm³ mol⁻¹	α	τ / s
5.5	0.27	-0.016	0.068	2.94×10^{-4}
5.0	0.30	-0.0095	0.086	1.18×10^{-3}
4.5	0.33	0.013	0.072	6.28×10^{-3}
4.0	0.38	0.0049	0.093	3.09×10^{-2}
3.5	0.44	0.0032	0.097	1.32×10^{-1}
3.0	0.52	0.0028	0.12	5.12×10^{-1}
1.8	26	0.0046	0.30	3.55×10^{3}

The natural logarithm of the reciprocal of the relaxation time τ, is plotted against the inverse of the temperature for **dil.1** in no applied static field and 1000 Oe (Figure 2-12(a,b)). The plots fit a straight line in the high temperature range. According to the regression in the temperature range between 8.0 and 5.2 K, the effective energy barrier (U_{eff}) of 54.0 cm^{-1} with the pre-exponential factor $\tau_0 = 3.17 \times 10^{-10}$ s was obtained. As anticipated from the temperature dependence of ac measurements (Figure 2-7), the U_{eff} value practically remains constant (53.9 cm^{-1}) by applying a static field of 1000 Oe (Figure 2-12(b)), suggesting that the temperature-dependent Orbach mechanism dominates in the high-temperature range.
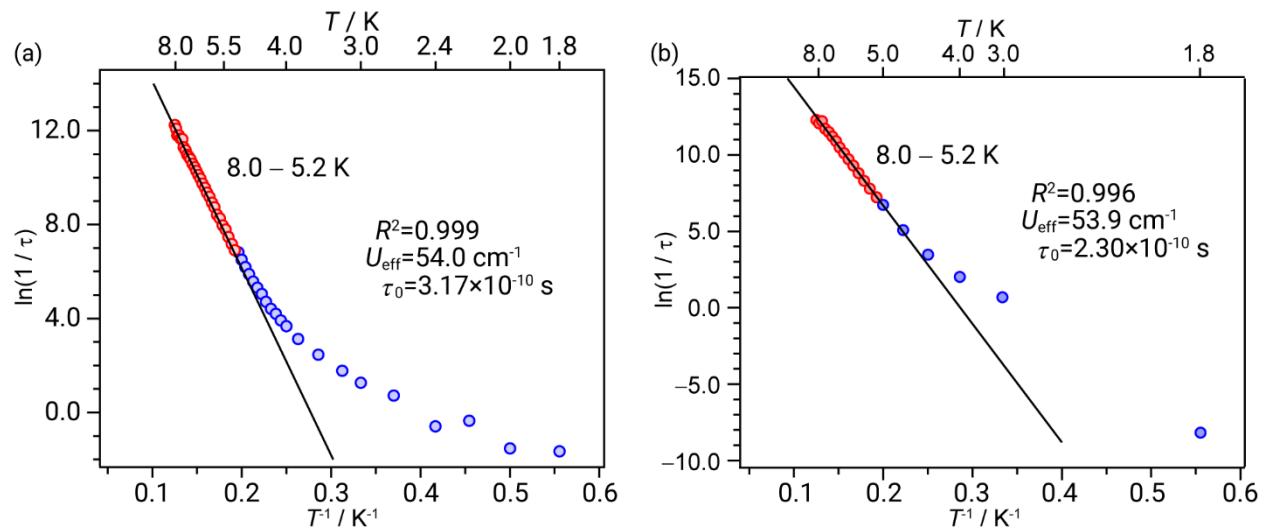
**Figure 2-12.** Natural logarithm of the magnetization relaxation time of **dil.1** against the inverse of the temperature at H_{dc} = (a) 0, and (b) 1000 Oe. The regression line obtained in the temperature range of 8.0 – 5.2 K is shown. The correlation factor (R^2) for the regression, effective energy barrier (U_{eff}), and preexponential factor (τ_0) are also given.

2-3-4 High-field, multi-frequency electron spin resonance

In order to evaluate the energy gap between the two doublets, high-field, multi-frequency ESR measurements were performed. Since we used a pulsed magnet, both the field ascending and descending processes were recorded and the signals appearing both processes were treated as the sample origin while appearing at only one of these were excluded as the noise.
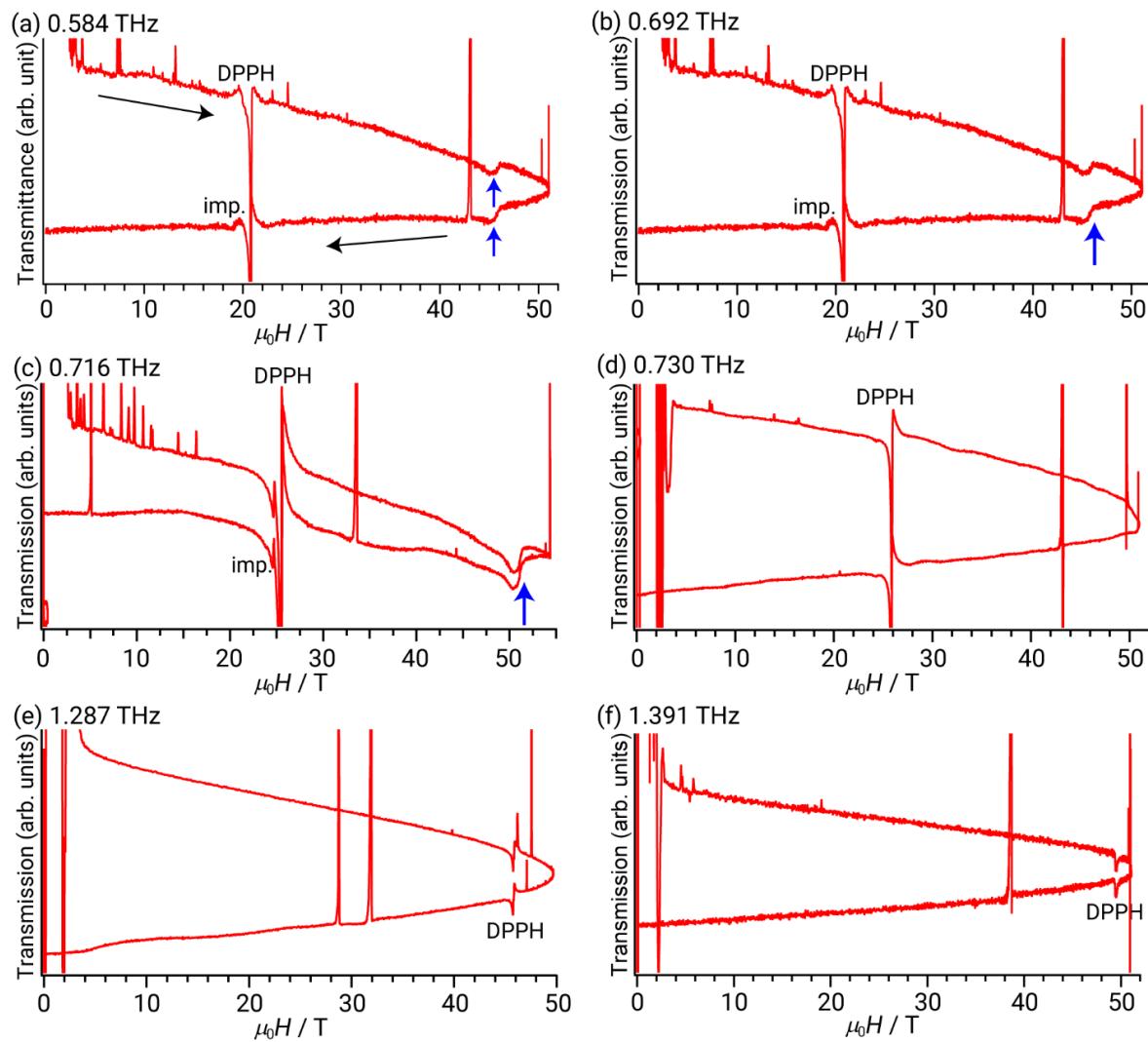

Figure 2-13. High-field, multi-frequency ESR spectra of **1** measured in the applied pulsed laser frequency of (a) 0.584, (b) 0.692, (c) 0.716, (d) 0.730, (e) 1.287, and (f) 1.391 THz at 4.2 K.
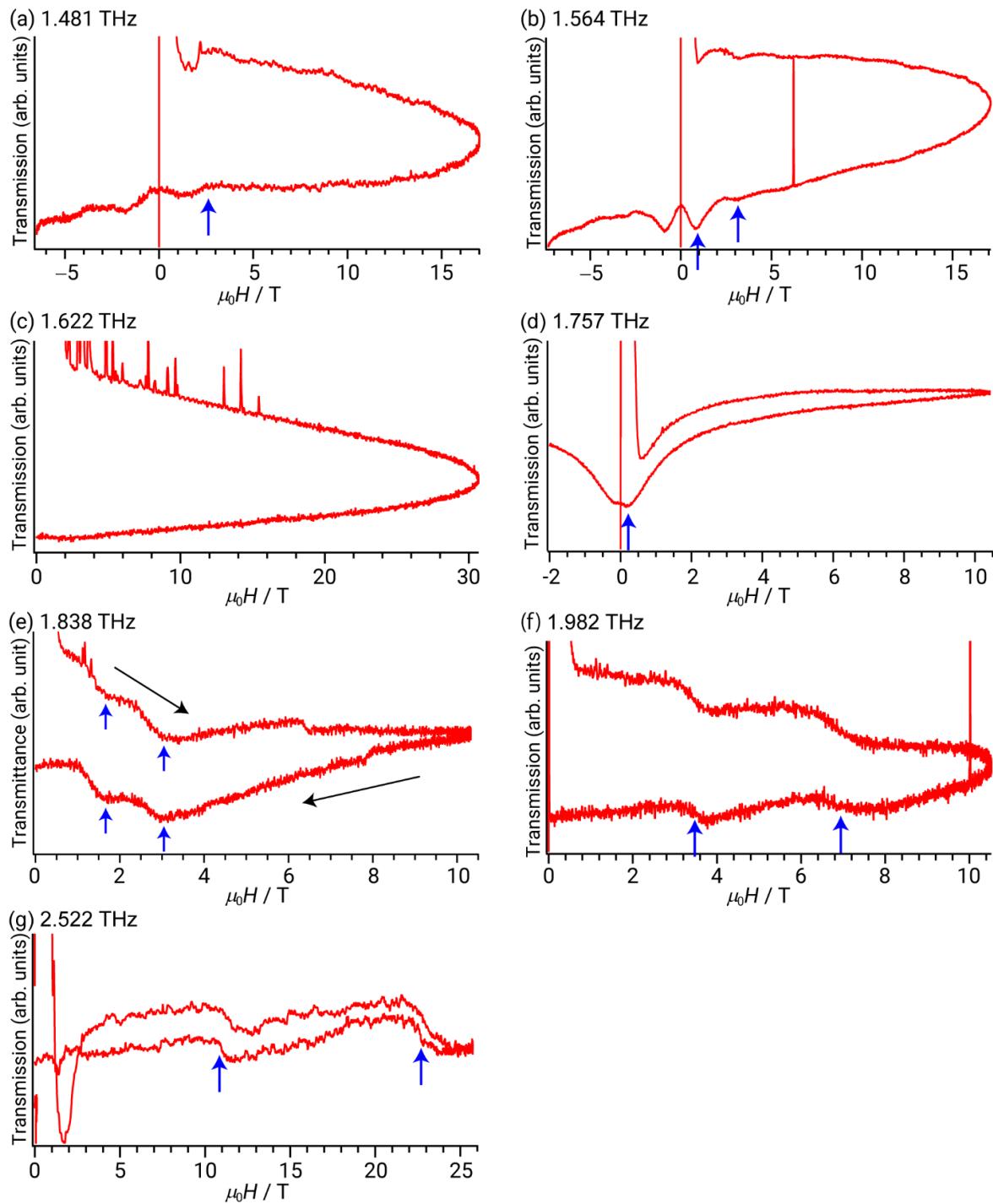
Figure 2-14. High-field, multi-frequency ESR spectra of **1** measured at (a) 1.481, (b) 1.564, (c) 1.622, (d) 1.757, (e) 1.838, (f) 1.982, and (g) 2.522 THz at 4.2 K.

45
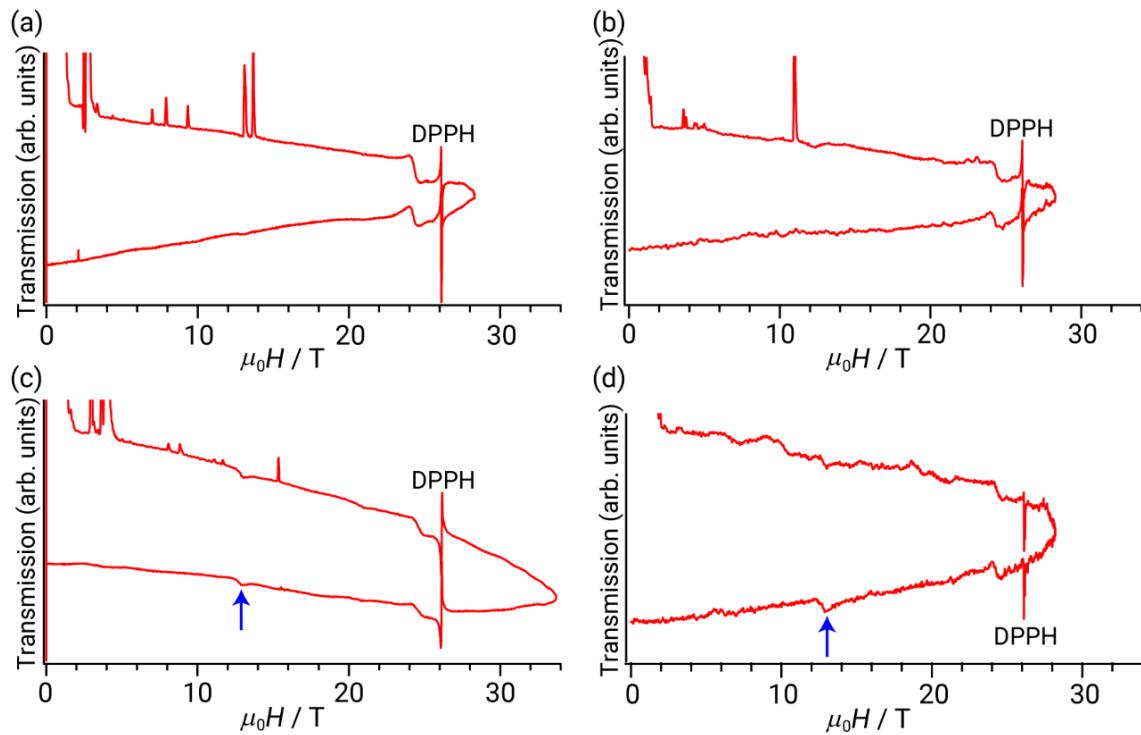
Figure 2-15. High-field, multi-frequency ESR spectra of **1** measured at 0.730 THz at (a) 1.4, (b) 4.2, (c) 77 K and (d) 100 K.

The spectra obtained at various frequencies are collected (Figure 2-13, 2-14), and the resonance fields are plotted in the frequency−magnetic field plane (Figure 2-16(a)). These experimental results were fitted by assuming $g_x = 2.1$, $g_y = 2.1$, $g_z = 2.6$, $D = -28.5$ cm^{-1}, and $E = 0.2$ cm^{-1}. Although no signal was detected corresponding to the square black symbols at 1.4 and 4.2 K (Figure 2-15 (a, b)), the appreciable signals were detected at ca. 13 T when the temperature was raised to 77 K (ca. 54 cm^{-1}) and 100 K (Figure 2-15 (c, d)). The signal can be assigned as the transitions between the upper two states, i.e., $|-1/2\rangle \rightarrow |+1/2\rangle$ (Figure 2-16(a,b) square), indicating the easy-axis type of electronic structures of **1**. To the best of my knowledge, this is the first example that unambiguously confirms the negative sign of the D value by observing the direct transition derived from the ground $\pm 3/2$ states to the excited $\pm 1/2$ states on the basis of the ESR

measurements for mononuclear cobalt complex that exhibit slow magnetic relaxation in no applied static magnetic field.
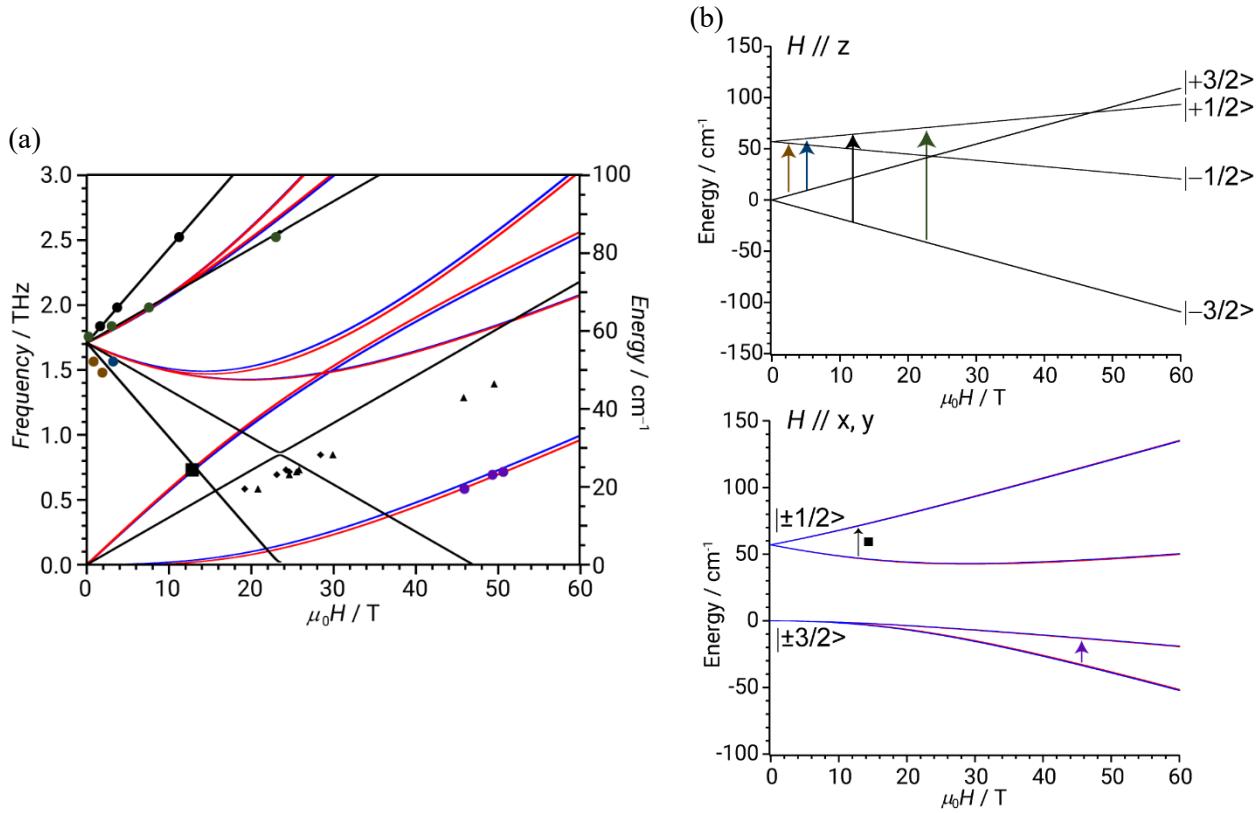
Figure 2-16. (a) Frequency-magnetic field plot of the experimental results. Signals arising from **1** at 4.2 K are plotted by the circles, while the signals appearing at high-temperatures (77 and 100 K) only are denoted by the squares. Signals of DPPH ($g \approx 2$) are plotted by the triangles and the signals next to DPPH is denoted by diamond which is expected to be paramagnetic impurities. The simulated field−frequency relationship is shown by the solid lines. Transitions associated with the magnetic fields parallel to the z, x, and y axes of the ZFS tensor are shown by the black, red and blue lines, respectively. (b) Zeeman diagrams for the Co(II) with anisotropic parameters in the text.

2-3-6 *Ab initio* calculations

Multi configuration *ab initio* calculations for **1** were performed by using the ORCA 4.0 program package. The molecular geometry was taken from the X-ray structure. The CAS(7,5) level SCF wave functions, i.e., seven electrons in the five active 3d-based orbitals, were calculated, which was followed by the N-electron valence state perturbation theory (NEVPT2) calculations in order to recover possible dynamic correlations. By including 10 quartets and 35 doublets for state interaction calculations, magnetic parameters of **1** have been predicted as follows: g_x = 2.107, g_y = 2.115, g_z = 2.566 (g_{iso} = 2.263), D = −38.2 cm^{-1}, $|E/D|$ < 0.01. Inspection of the individual contributions of the excited states to the D tensor has clarified that the large negative D value is arising from the first excited quartet (−55.7 cm^{-1}), while the second and third excited quartets impose the opposite effects on the D value (5.0 and 6.3 cm^{-1}, respectively), suggesting that the mixing of the higher excited states is non-negligible for the magnetic anisotropy of this type of mononuclear SMMs (Table 2-9). Although some excited states contribute to the E value to a certain degree, these compensate for each other, giving rise to the small total $|E|$. According to the results of the calculations, the ground SOC state arising from the quartet is the doublet which is mainly composed of the $|M_S\rangle = |\pm 3/2\rangle$ (Table 2-10); that is, the magnetic relaxations through the mixed wave functions are unlikely preferable in the ground states. On the contrary, the first excited SOC state at 76.4 cm^{-1} in energy is composed of the mixture of $|\pm 1/2\rangle$. Consequently, the magnetization is easily reversed at the thermally excited states through the mixing of the $|\pm 1/2\rangle$ wave functions, consistent with the experimental results. The calculated direction of the anisotropic axis is depicted in Figure 2-17. The easy-axis approximately bisects the molecule through the N1−Co−N3 direction, although the axis slightly inclines to the methoxy-substituted sites.

Table 2-10. Contribution of selected excited states to the *D*-tensor.

Multplet	Root	D / cm^{-1}	E / cm^{-1}	Multplet	Root	D / cm^{-1}	E / cm^{-1}
4	0	0	0	2	13	0.094	0.002
4	1	−52.378	−0.151	2	14	−0.154	0.163
4	2	5.024	−5.512	2	15	0.007	0.039
4	3	6.258	6.258	2	16	−0.077	−0.077
4	4	0.62	−0.895	2	17	−0.003	−0.003
4	5	0.001	0.001	2	18	−0.004	−0.004
4	6	0.064	−0.065	2	19	0.064	0.002
4	7	0.001	−0.002	2	20	−0.006	0.007
4	8	0	0	2	21	−0.854	-0.854
4	9	−0.003	0	2	22	−0.758	0.773
2	0	−0.341	1.063	2	23	−0.001	−0.001
2	1	−0.745	−0.745	2	24	−0.001	0.001
2	2	−0.042	−0.042	2	25	0.129	0.001
2	3	0.104	0.03	2	26	−0.002	−0.002
2	4	0	0	2	27	−0.003	-0.003
2	5	−0.016	−0.016	2	28	−0.002	−0.002
2	6	6.329	0.019	2	29	0.356	0.004
2	7	−0.824	0.83	2	30	−0.05	0.064
2	8	−1.887	−1.887	2	31	−0.064	−0.064
2	9	−1.191	1.207	2	32	−0.035	−0.035
2	10	0.989	0.116	2	33	−0.027	0.035
2	11	−0.191	−0.191	2	34	0	0
2	12	−0.008	−0.008				

Table 2-11. Wavefunctions for the ground and first excited states obtained at the QDPT with NEVPT2 level.

| state	$Energy$ / cm^{-1}	weight	root	spin	M_s
0	0.0000	0.079870	0	3/2	3/2
		0.866807	0	3/2	−3/2
		0.045902	1	3/2	−3/2
1	0.0000	0.866807	0	3/2	3/2
		0.045902	1	3/2	3/2
		0.079870	0	3/2	−3/2
2	76.4024	0.607675	0	3/2	1/2
		0.379487	0	3/2	−1/2
3	76.4024	0.379487	0	3/2	1/2
		0.607675	0	3/2	−1/2
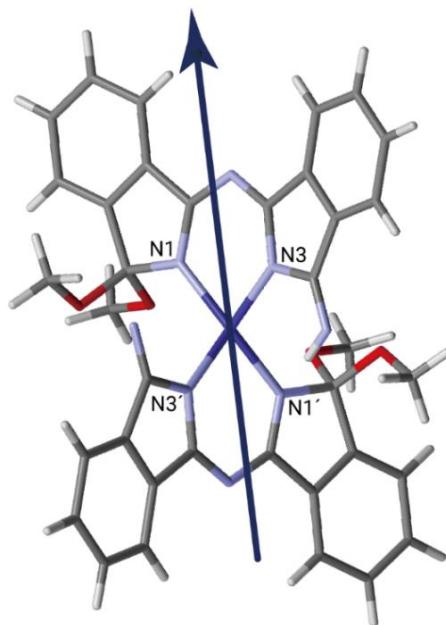
Figure 2-17. Ising axis obtained by CASSCF/RASSI calculation on ORCA.

2-4 Conclusion

We have demonstrated that a novel four coordinate mononuclear Co(II) complex **1** prepared from the reaction of 1,2-dicyanobenzene with lithium methoxide followed by the metal coordination, exhibits slow magnetic relaxations even in the absence of the external static magnetic field. Magnetic studies have clarified that the complex has a large axial magnetic anisotropy, and the magnetic relaxations are largely affected by the presence of the intramolecular and intermolecular factors in the low-temperature range, while the Orbach process is dominant in the high-temperature range. The effective relaxation energy barrier (U_{eff}) of 54.0 cm^{-1} and the axial anisotropic parameter (D) of -28.5 cm^{-1} were obtained from the ac magnetic susceptibility and high-field, multi-frequency ESR data, respectively. The zero-field splitting (ZFS) energy is evaluated to be 57.0 cm^{-1}, which is comparable to the estimated U_{eff} energy.

2-5 References

1. Craig, G. A.; Murrie, M. 3d single-ion magnets. *Chem. Soc. Rev.*, **2015**, *44*, 2135-2147.

2. Frost, J. M.; Harriman, K. L. M.; Murugesu, M. The rise of 3-d single-ion magnets in molecular magnetism: towards materials from molecules? *Chem. Soc.*, 2016, 7, 2470-2491.

3. Feng, M.; Tong. M. -L. Single Ion Magnets from 3d to 5f: Developments and Strategies. *Chem. Eur. J.*, **2018**, *24*, 7574-7594.

4. Zadrozny, M.; Long. J. R. Slow Magnetic Relaxation at Zero Field in the Tetrahedral Complex $[Co(SPh)_4]^{2-}$. *J. Am. Chem. Soc.*, **2011**, *133*, 20732-20734.

5. Novikov, V. V.; Pavlov, A. A.; Nelyubina, Y. V.**;** Boulon, M. -E.; Varzatskii, O. A.; Voloshin, Y. Z.; Winpenny, R. E. P. A Trigonal Prismatic Mononuclear Cobalt(II) Complex Showing Single-Molecule Magnet Behavior. *J. Am. Chem. Soc.*, **2015**, *137*, 9792-9795.

6. Pavlov, A. A.; Savkina, S. A.; Belov, A. S.; Nelyubina, Y. V.; Efimov, N. N.; Voloshin, Y. Z.; Novikov, V. V. Trigonal Prismatic Tris-pyridineoximate Transition Metal Complexes: A Cobalt(II) Compound with High Magnetic Anisotropy. *Inorg. Chem.*, **2017**, *56*, 6943-6951.

7. Zhu, Y-Y.; Cui, C.; Zhang, Y-Q.; Jia, J-H.; Guo, X.; Gao, F.; Qian, K.; Jiang, S-D.; Wang, B-W.; Wang, Z-M.; Gao. S. Zero-field slow magnetic relaxation from single Co(II) ion: a transition metal single-molecule magnet with high anisotropy barrier. *Chem. Sci.*, **2013**, *4*, 1802-1806.

8. Zhu, Y.-Y.; Zhang, Y.-Q.; Yin, T.-T.; Gao, C.; Wang, B.-W.; Gao. S. A Family of $Co^{II}Co^{III}_3$ Single-Ion Magnets with Zero-Field Slow Magnetic Relaxation: Fine Tuning of Energy Barrier by Remote Substituent and Counter Cation. *Inorg. Chem.*, **2015**, *54*, 5475-5486.

9. Rigamonti, L.; Bridonneau, N.; Pontei, G.; Tesi, L.; Sorace, L.; Pinkowicz, D.; Jover, J.; Ruiz, E.; Sessoli, R.; Cornia. A.; A Pseudo-Octahedral Cobalt(II) Complex with

Bispyrazolylpyridine Ligands Acting as a Zero-Field Single-Molecule Magnet with Easy Axis Anisotropy. *Chem. Eur. J.*, **2018**, *24*, 8857-8868.

10. Zadrozny, J. M.; Telser, J.; Long. J. R.; Slow magnetic relaxation in the tetrahedral cobalt(II) complexes $[Co(EPh)_4]^{2-}$ (E=O, S, Se). *Polyhedron*. **2013**, *64*, 209-217.

11. Fataftah, M. S.; Zadrozny, J. M.; Rogers, D. M.; Freedman. D. E.; A Mononuclear Transition Metal Single-Molecule Magnet in a Nuclear Spin-Free Ligand Environment. *Inorg. Chem.*, **2014**, *53*, 10716-10721.

12. Carl, E.; Demeshko, S.; Meyer, F.; Stalke, D. Triimidosulfonates as Acute Bite-Angle Chelates: Slow Relaxation of the Magnetization in Zero Field and Hysteresis Loop of a Co^{II} Complex. *Chem. Eur. J.*, **2015**, *21*, 10109-10115.

13. Rechkemmer, Y.; Breitgoff, F. D.; M. van der Meer, Atanasov. M.; Hakl, M.; Orlita, M.; Neugebauer, P.; Neese, F.; Sarkar, B.; J. van Slageren. A four-coordinate cobalt(II) single-ion magnet with coercivity and a very high energy barrier. *Nat. Commun.*, **2016**, *7*, 10467-10484.

14. Sottini, S.; Poneti, G.; Ciattini, S.; Levesanos, N.; Ferentinos, E.; Krzystek, J.; Sorace, L.; Kyritsis, P. Magnetic Anisotropy of Tetrahedral Co^{II} Single-Ion Magnets: Solid-State Effects. *Inorg. Chem.*, **2016**, *55*, 9537-9548.

15. Vaidya, S.; Tewary, S.; Singh, S. K.; Langley, S. K.; Murray, K. S.; Lan, Y.; Wernsdorfer, W.; Rajaraman, G.; Shanmugam. M. What Controls the Sign and Magnitude of Magnetic Anisotropy in Tetrahedral Cobalt(II) Single-Ion Magnets?. *Inorg. Chem.*, **2016**, *55*, 9564-9578.

16. Tu, D.; Shao, D.; Yan, H.; Lu. C. A carborane-incorporated mononuclear Co(II) complex showing zero-field slow magnetic relaxation. *Chem Commun.*, **2016**, *52*, 14326-14329.

17. Mitsuhashi, R.; Hosoya, S.; Suzuki, T.; Sunatsuki, Y.; Sakiyama, H.; Mikuriya, M. Hydrogen-bonding interactions and magnetic relaxation dynamics in tetracoordinated cobalt(II) single-ion magnets. *Dalton Trans.*, **2019**, *48*, 395–399.

18. Zadrozny, J. M.; Xiao, D. J.; Atanasov, M.; Long, G. J.; Grandjean, F.; Neese, F.; Long. J. R.; Magnetic blocking in a linear iron(I) complex. *Nat. Chem.*, **2013**, *5*, 577-581.

19. Werncke, C. G.; Bunting, P. C.; Duhayon, C.; Long, J. R.; Bontemps, S.; Sabo-Etienne, S. Two-Coordinate Iron(I) Complex [Fe{N(SiMe$_3$)$_2$}$_2$]$^-$: Synthesis, Properties, and Redox Activity. *Angew. Chem., Int. Ed.* **2015**, *54*, 245−248.

20. Yao, X.-N.; Du, J.-Z.; Zhang, Y.-Q.; Leng, X.-B.; Yang, M.-W.; Jiang, S.-D.; Wang, Z.-X.; Ouyang, Z.-W.; Deng, L.; Wang, B.-W.; Gao. S. Two-Coordinate Co(II) Imido Complexes as Outstanding Single-Molecule Magnets. *J. Am. Chem. Soc.*, **2017**, *139*, 373-380.

21. Bunting, P. C.; Atanasov, M.; Damgaard-Møller, E.; Perfetti, M.; Crassee, I.; Orlita, M.; Overgaard, J.; van Slageren, J.; Neese, F.; Long, J. R. A linear cobalt(II) complex with maximal orbital angular momentum from a non-Aufbau ground state. *Science* **2018**, *362*, eaat7319.

22. Gatteschi, D.; Sessoli, R. Quantum Tunneling of Magnetization and Related Phenomena in Molecular Materials. *Angew. Chem. Int. Ed.*, **2003**, *42*, 268-297.

23. Sessoli, R.; Tsai, H.-L.; Schake, A. R.; Wang, S.; Vincent, J. B.; Folting, K.; Gatteschi, D.; Christou, G.; Hendrickson, D. N. High-Spin Molecules: [Mn$_{12}$O$_{12}$0(O$_2$CR)$_{16}$(H$_2$O)$_4$]. *J. Am. Chem. Soc.* **1993**, *115*, 1804-1816.

24. Waldmann, O.; Ako, A. M.; Güdel, H. U.; Powell, A. K. Assessment of the Anisotropy in the Molecule Mn19 with a High-Spin Ground State S = 83/2 by 35 GHz Electron Paramagnetic Resonance. *Inorg. Chem.* **2008,** *47*, 3486-3488.

25. Krzystek, J.; Zvyagin, S. A.; Ozarowski, A.; Fiedler, A. T.; Brunold, T. C.; Telser, J. Definitive Spectroscopic Determination of Zero-Field Splitting in High-Spin Cobalt(II). *J. Am. Chem. Soc.* **2004**, *126*, 2148−2155.

26. Idešicová, M.; Titiš, J.; Krzystek, J.; Boča, R. Zero-Field Splitting in Pseudotetrahedral Co(II) Complexes: a Magnetic, High- Frequency and -Field EPR, and Computational Study. *Inorg. Chem.* **2013**, *52*, 9409−9417.

27. Schweinfurth, D.; Krzystek, J.; Atanasov, M.; Klein, J.; Hohloch, S.; Telser, J.; Demeshko, S.; Meyer, F.; Neese, F.; Sarkar, B. Tuning Magnetic Anisotropy Through Ligand Substitution in Five-Coordinate Co(II) Complexes. *Inorg. Chem.* **2017**, *56*, 5253−5265.

28. Fukuda, T; Kikukawa, Y; Turuya, R; Fuyuhiro, A; Ishikawa, N; Kobayashi, N. Effect of Chain Length on Thermal Conversion of Alkoxy-Substitude Copper Phthalocyanine Precursors. *Inorg. Chem.* **2011**, *50*, 11832-11837.

29. Kikukawa, Y; Fukuda, T; Fuyuhiro, A; Ishikawa, N; Kobayashi, N. Facile one-pot preparation of thermally and photochemically convertible soluble precursor of copper phthalocyanine and naphthalocyanine. *Chem. Commun.* **2011**, *47*, 8518-8520.

30. Fukuda, T.; Shigeyoshi, N.; Fuyuhiro, A.; Ishikawa, N. First example of a hexadentate bicyclic phthalocyanine analogue containing a divalent metal center. *Dalton Trans.* **2013**, *42*, 16486–16489.

31. Sheldrick, G. M. *A short history of SHELX. Acta Crystallogr., Sect. A: Found. Crystallogr.* **2008**, *64*, 112−122.

32. Bain, G. A.; Berry, J. F. Diamagnetic Corrections and Pascal's Constants. *J. Chem. Educ.* **2008**, *85*, 532−536.

33. Neese, F. ORCA - *An ab Initio, Density Functional and Semiempirical Program Package*, version 4.0; **2017**.

34. Neese, F. Software Update: The ORCA Program System, version 4.0. *WIREs Comput. Mol. Sci.* **2018**, *8*, e1327.

35. Neese, F. ORCA Program System. *WIREs Comput. Mol. Sci.* **2012**, *2*, 73−78.

36. Vaidya, S.; Singh, S. K.; Shukla, P.; Ansari, K.; Rajaraman, G.; Shanmugam, M. Role of Halide Ions in the Nature of the Magnetic Anisotropy in Tetrahedral Co^{II} Complexes. *Chem. Eur. J.* **2017**, *23*, 9546−9559.

Chapter 3

The effect of intermolecular interactions on slow

magnetic relaxations of a mononuclear tetrahedral four-

coordinate cobalt(II) complex with bidentate ligands

comprised of pyrrolopyrrole and benzothiazole moieties

3-1 Introduction

3-1-1 The effect of intermolecular interactions on dynamic magnetic relaxations

  The intermolecular dipolar interactions are one of the main factors for promoting quantum tunneling of magnetizations (QTM), and in general, they disturb the observation of slow magnetic relaxations.[1] However, the effect of intermolecular interactions on dynamic magnetic properties has been interested in a point of view of controlling QTM. In manganese tetranuclear clusters, formation of hydrogen-bond dimer decreases the QTM rate in the absence of static field through exchange bias.[2,3] Recently, Mikuriya and coworkers reported three mononuclear tetrahedral four-coordinate Co(II) complexes having different intermolecular hydrogen-bond networks. Interestingly, the two complexes with smaller intermolecular Co-Co distance show slow magnetic relaxation even in no applied static field.[4]

  In addition, slow magnetic relaxations based on intermolecular interactions have also been reported. Murugesu and coworkers demonstrated the intermolecular origin slow magnetic relaxations at low temperature by ac measurements on several concentrations of magnetically dilution samples of a mononuclear Co(II) complex.[5] Boca and coworkers reported Co(II), Ni(II), Cu(II) mononuclear six-coordinate transition metal complexes forming hydrogen-bonding dimers.[6-8] All three complexes exhibit slow magnetic relaxation in an applied static field, and multiple relaxation behaviors are indicated. Interestingly, the comparison with magnetically diluted sample showed slow relaxations of intermolecular origin were much slower than intramolecular ones in the Co(II) complex.[6]

3-1-2 Pyrrolopyrrole-based bidentate ligands

Shimizu and coworkers reported the dehydration (Schiff-base) reactions of the diketo-pyrrolopyrrole and hetero aromatic amines moieties afforded organic molecules that have intense absorption in visible and NIR region.[9] The boron complexes composed of the aza-bridged π-conjugate molecules are expected for light harvesting and fluorescent materials.[10] The bidentate ligand molecules also form stable complexes containing first-row transition metal ions (Figure 3-1). While the absorption and fluorescent properties have been investigated, the magnetic properties of the transition metal complexes are not investigated. As mentioned previous chapter, tetrahedral four-coordinate Co(II) complexes are expected to exhibit slow magnetic relaxations owing to the large magnetic anisotropy arising from the mixing of nearly degenerated excited states.[1] In addition, the pyrrolopyrrole-based bidentate ligands can be easily tuned by introducing functional groups to the pyrrolopyrrole and aromatic amines.[11,12] The intermolecular hydrogen-bonding interactions of complex are also expected to introducing hetero atoms to the ligand. The dynamic magnetic properties of complexes with strong intermolecular interactions are interested.
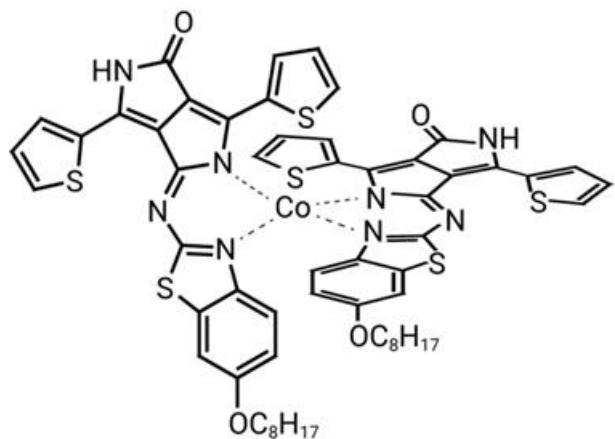

Figure 3-1. Molecular structure of [Co(L)₂] (**2**).

3-2 Experimental section

Syntheses of [Co(L)$_2$] (**2**) and [Zn(L)$_2$] were performed at the Furuta group in Kyusyu University.

3-2-1 Preparation of [Co$_{0.055}$Zn$_{0.945}$(L)$_2$], **dil.2**

A mixture of **2** and [Zn(L)$_2$] in a molar ratio of 5.5 : 94.5 was dissolved in chloroform and passed through a bio-beads column. The eluent was collected, concentrated in vacuo and dried under reduced pressure at 50 ℃ for 1 day.

3-2-2 Measurements

Static magnetic properties were collected using a Quantum Design MPMS-XL7AC SQUID magnetometer. The sample was prepared by wrapping 6.80 mg (5.77×10^{-6} mol) of **2** in an aluminum foil of 18.72 mg. Diamagnetic components were estimated using the Pascal constants,[13] and the contribution from the aluminum foil was corrected on the basis of the blank measurement. Ac measurements were performed on a Quantum Design MPMS-XL7AC (0.1-1340 Hz) with employing oscillating magnetic field of 3.9 Oe. The undiluted sample was prepared by fixing 30.1 mg of **2** in a gelatin capsule using eicosane. The diluted sample was prepared by fixing 156.27 mg of **dil.2** in a sample using eicosane.

Ab initio quantum calculations were conducted on the ORCA 4.0 program package.[14-16] The resolution of identity (RI) approximation technique was employed with the def2-TZVPP basis set and def2/JK auxiliary basis set implemented in ORCA. The complete active space self-consistent field (CASSCF) calculations were performed on specified seven active electrons in five Co-based 3d orbitals. For state interaction calculations, 10 quartets and 35 doublets were included. Dynamic correlations were recovered by N-electron valence state perturbation theory.

3-3 Results and Discussion

3-3-1 Molecular structure

The complex **2** was synthesized and structurally characterized at the Furuta group in Kyusyu University. Single crystal X-ray analysis revealed that this complex was composed of a cobalt ion and two bidentate ligands synthesized from Schiff base reaction of pyrrolopyrrole and benzothiazole moieties (Figure 3-2). **2** has the *I/2a* space group, in which the C_2 axes were on the Co atoms. No counter ions were found, implying that complex **2** was neutral in total. The bond lengths between the central Co and the N2 and N4 atoms are almost identical: Co1-N2 = 1.9832 Å and Co-N4 = 1.9835 Å, respectively. The bond angles between the Co and N atoms are in the range of 95.24° (for N2-Co-N4) to 125.83° (for N2-Co-N2′). The former is much smaller than that anticipated from the ideal T_d symmetry, which indicates the Co site of **2** is distorted to give the elongated T_d ligand field along almost perpendicular to the C_2 axis. The dihedral angle between the two ligands measured without thiophen rings and octoxy chains (88.49°) is slightly smaller than that for the ideal T_d geometry (90°). The lattice constants are unusually large compared with those of typical mononuclear Co(II) complexes due to the presence of the long octyl chains of the complexes.[17] Nevertheless, the shortest intermolecular Co-Co distance of 10.188 Å is in the range of typical mononuclear systems. In the crystals, intermolecular hydrogen-bond interactions were found for the S3⋯H15′-C15′ pair with the distances of 2.864 Å (Figure 3-3(a), and highly planar between N1-H…O1′ and O1…H′-N1′ double hydrogen bonds can be recognized in the second shortest intermolecular Co-Co pairs (Figure 3-3(b)). According to the almost perpendicular coordination geometry and the intermolecular hydrogen-bond network, the molecules are aligned

in the 1-dimensional zigzag chain fashion, while these chains are stabilized by the mutual S-H

interactions, giving the 3-dimensional hydrogen-bond network in total.
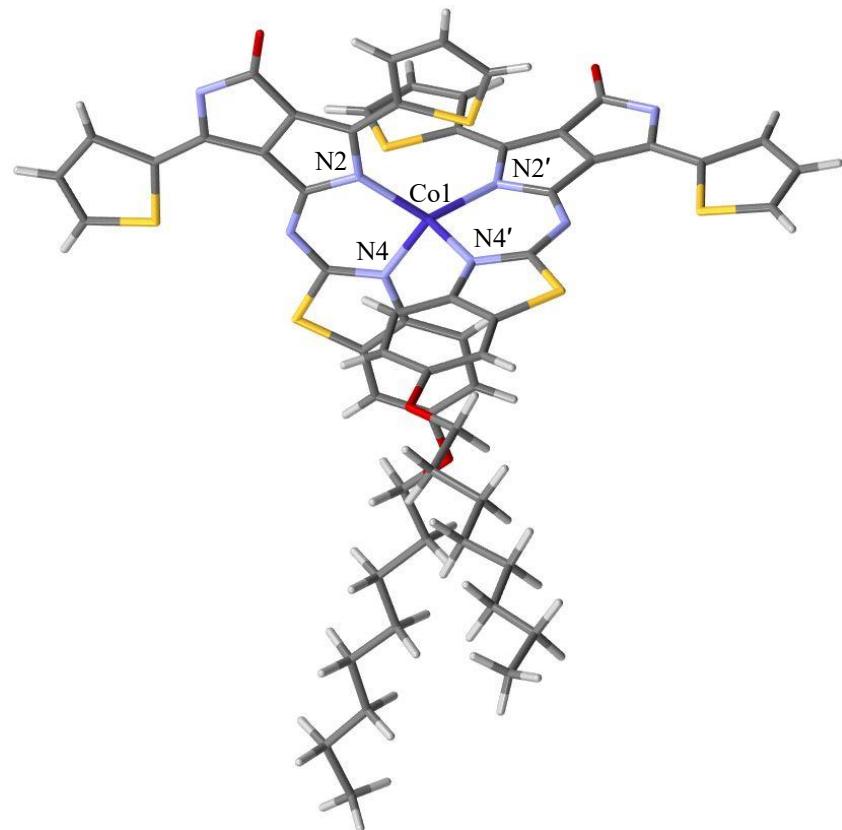
**Figure 3-2.** Caped stick diagram of [Co(L)$_2$] (**2**).
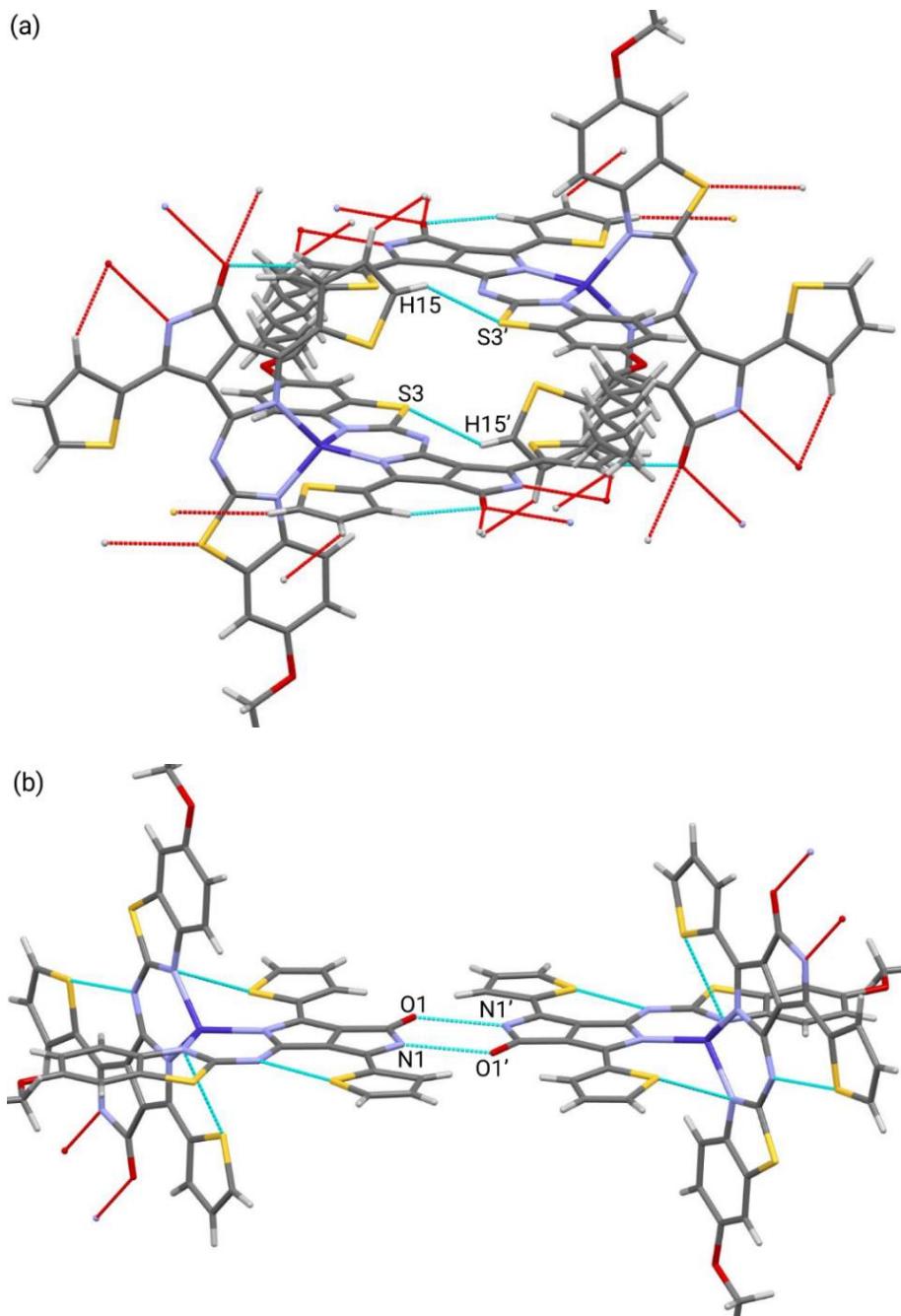
Figure 3-3. Intramolecular hydrogen bond interactions between (a) S3···H15′-C15 and (b) N1···O1' in the crystal lattice of **2** molecules.

3-3-2 Static magnetic properties

The temperature dependence of $\chi_M T$ products obtained in an applied field of 1000 Oe is shown in Figure 3-4. The $\chi_M T$ values at 300 K of 2.21 cm^3 K mol^{-1} gradually decrease with lowering the temperature down to 50 K. Below 50 K, the value drops to 1.33 cm^3 K mol^{-1} at 1.8 K. The former is attributed to the temperature independent paramagnetism (TIP) arising from the mixing of the low-lying excited states, and the latter can be ascribed to the magnetic anisotropy of the Co ions.
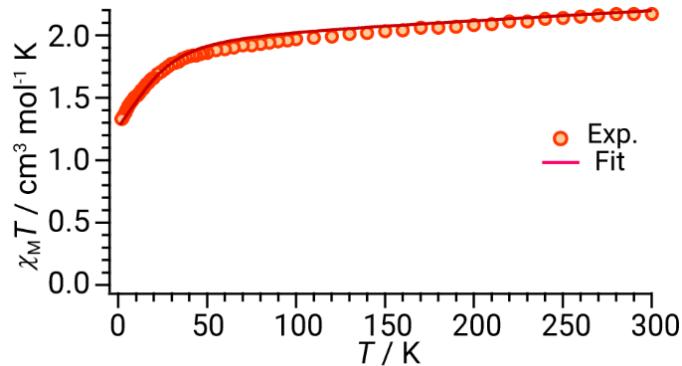

Figure 3-4. Temperature dependence of $\chi_M T$ products between 300 to 1.8 K of **2**. Fitting curve with following parameters (discussed below): $g_z = 2.12$, $g_{x,y} = 2.0$, $D = -27.0$ cm^{-1}, TIP = 8×10^{-4} cm^3 mol^{-1}.

The static magnetic field dependence of magnetization measurements shows no remnant magnetization at zero static field and no hysteresis loops are recognized (Figure 3-5). The dispersion of the M vs. HT^{-1} plots indicates a significant magnetic anisotropy of the Co ions. In order to estimate the anisotropic parameters of **2**, The magnetization data were analysed by the following anisotropic spin Hamiltonian.

$$\hat{H} = g_{\mathrm{iso}}\mu_{\mathrm{B}}\boldsymbol{S}\cdot\boldsymbol{H} + D\left\{\hat{S}_z^2 + \frac{1}{3}S(S+1)\right\} + E\left(\hat{S}_x^2 - \hat{S}_y^2\right)$$

The best fit was obtained by using the following parameters: $g_{\mathrm{iso}} = 2.104$, $D = -27.1$ cm^{-1} and $|E| = 5.17\times10^{-5}$ cm^{-1} (Figure 3-6). Obtained large and negative D value indicates the large easy-axis type of magnetic anisotropy of **2**. The rhombic magnetic anisotropy E is negligible, however, the magnitude of E is not sensitive to magnetization measurements.[18] In order to confirm the magnitude of D, the $\chi_{\mathrm{M}}T$ -T plot was also fitted using anisotropic g, axial parameter D and TIP component. The best fit parameters are as follows: $g_z = 2.12$, $g_{x,y} = 2.0$, $D = -27.0$ cm^{-1}, TIP $= 8\times10^{-4}$ cm^3 mol^{-1}. The obtained TIP value is slightly larger than that of typical 3d mononuclear complexes.[19] The obtained g and D are comparable to those determined by magnetization fitting and theoretical calculations discussed below.
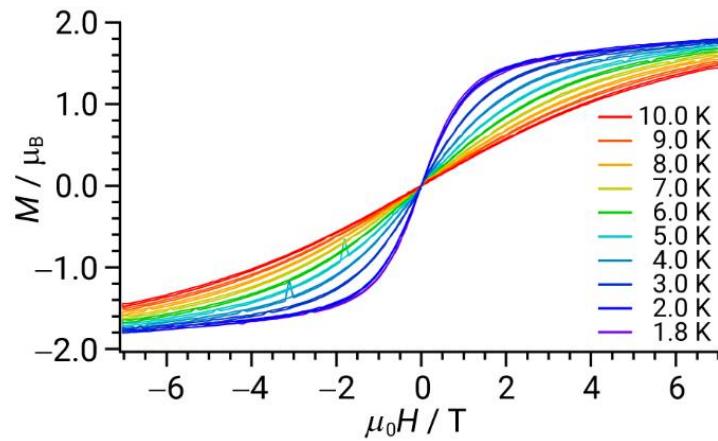
**Figure 3-5.** The Magnetization (M) – magnetic field ($\mu_0 H$) plot of **2**.
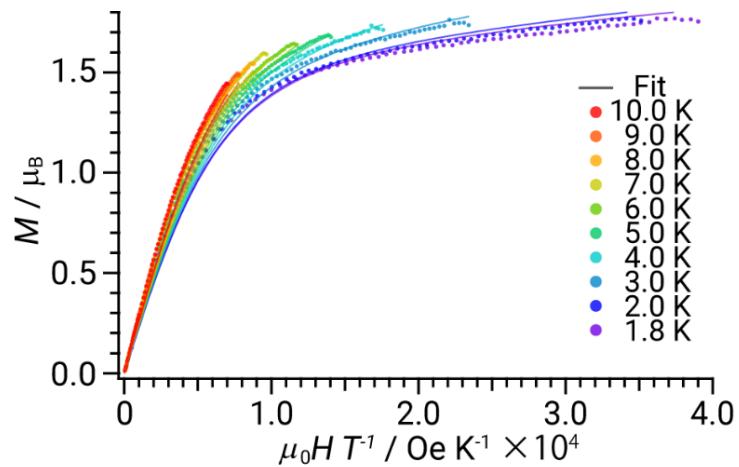
Figure 3-6. The $M - \mu_0 HT^{-1}$ plot of **2**. Fitting curves were plotted with the following parameters:

$g_{iso} = 2.104$, $D = -27.1$ cm^{-1} and $|E| = 5.17 \times 10^{-5}$ cm^{-1}

3-3-3 Dynamic magnetic properties

In order to investigate magnetic relaxations and the effect of intermolecular interactions, ac magnetic susceptibility measurements were performed on both pristine **2** and magnetically diluted **2** [$Co_{0.055}Zn_{0.945}L_2$] (**dil.2**). In the absence of static magnetic field, only small uplift of χ'' signals at ac frequency above 100 Hz was observed even at 1.8 K for **2** (Figure 3-7(a)), which is due probably to the fast quantum tunnelling of magnetization. In the case of **dil.2**, although the χ'' peaks are still unclear, the signals are larger compared with those of undiluted **2**. They can be attributed to decrease of QTM through intermolecular interactions by magnetic dilutions (Figure 3-7(b)). In addition, two peaks in χ'' and the corresponding dual semi-cycles in the Cole-Cole plot below 4.5 K (Figure 3-7(b)) indicate the existence of multiple relaxation processes with different relaxation times at these temperatures.
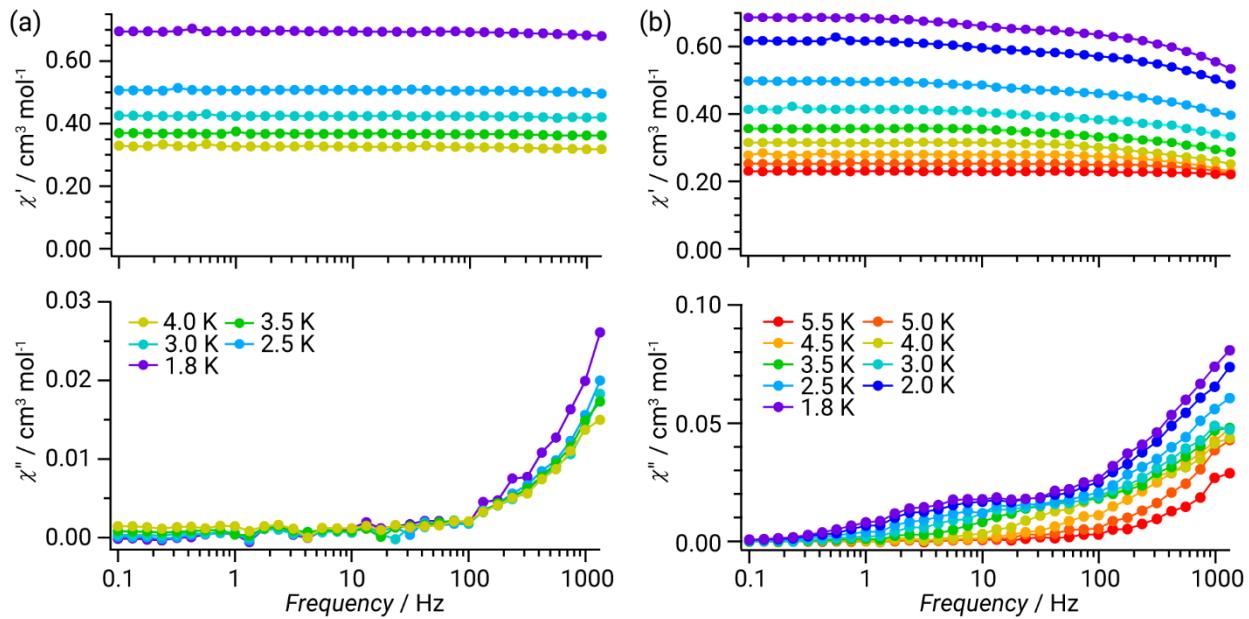
Figure 3-7. Frequency dependence of χ' and χ'' of (a) **2** and (b) **dil.2** in the absence of static magnetic field.
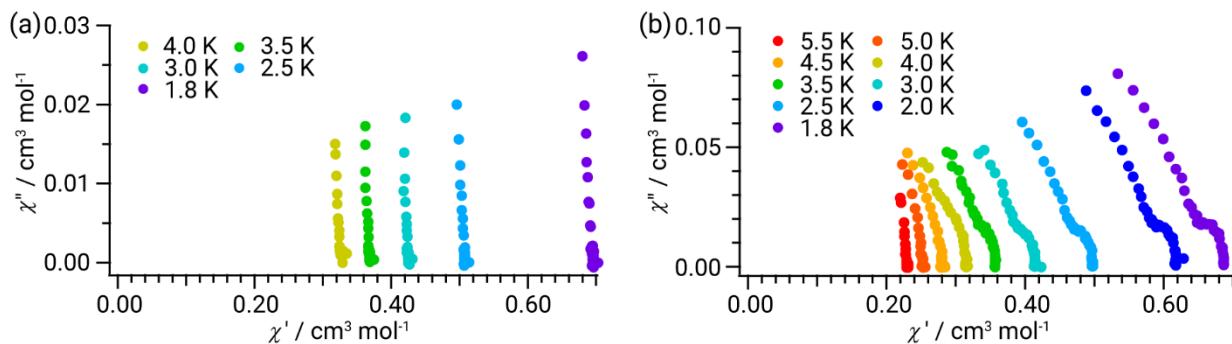
**Figure 3-8.** Cole-Cole plots of (a) **2** and (b) **dil.2** in the absence of static magnetic field.
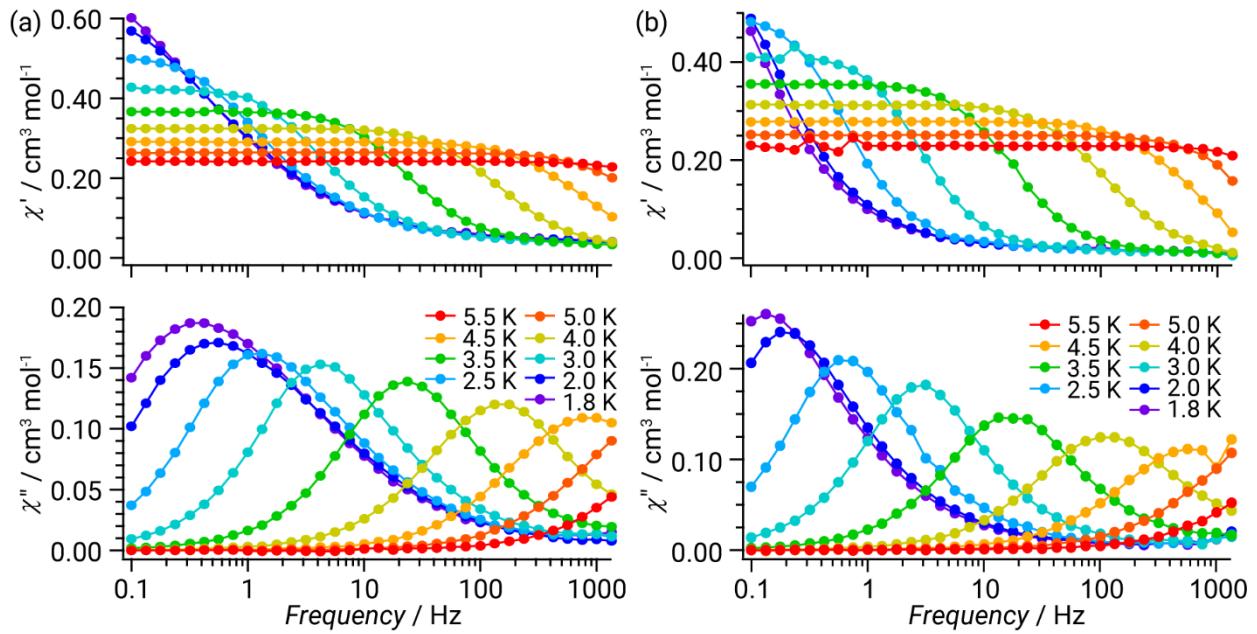
Figure 3-9. Frequency dependence χ' and χ'' of (a) **2** and (2) **dil.2** in an applied static field of 1000 Oe.


Figure 3-10. Cole-Cole plots for (a) **2** and (b) **dil.2**. in an applied static field of 1000 Oe.

Applying a static field of 1000 Oe, the slow relaxations were largely enhanced, and frequency-dependent χ'' peak maxima were recognized below 5.0 K for both **2** and **dil.2** (Figure 3-9(a, b)), which can be attributed to the slow down tunnelling relaxation paths by applying a static field. Between 5.5 and 3.0 K, the peaks were almost equivalent for **2** and **dil.2**. However, significant difference was observed the temperature below 3.0 K. At these temperatures, the χ'' peaks are apparently sharper and the peak maxima are situated in lower frequencies for **dil.2**, which indicates that the intermolecular interactions have significant effect on magnetic relaxations below 3.0 K even in static magnetic field of 1000 Oe.

The Cole-Cole plots showed single semi-circle at each temperature (Figure 3-10(a,b)). The Debye model with single relaxation time was employed to determine the relaxation times for each condition. Fitting parameters were listed on Table 3-1 and 3-2. In **dil.2**. the relaxation times τ are larger and the distribution coefficients α become smaller than that of undiluted **2** for all measured temperatures. However, the significant differences are recognized below 3.0 K. It is noted that dispersion coefficients α for undiluted **2** at low temperatures are quite large, e.g. 0.40 at 1.8 K (for $\alpha = 0$, single relaxation). The dispersion coefficient α for dil.2 at 1.8 K (0.25) is significantly smaller than that of undiluted **2**, and relaxation time τ become larger from 0.376 s (for **2**) to 1.28 s (for **dil.2**).

Table 3-1. Fitting parameters of **2** in an applied static magnetic field of 1000 Oe.

T / K	χ_t / cm^3 mol^{-1}	χ_s / cm^3 mol^{-1}	α	τ / s
5.5	0.24	0.0050	0.076	2.14×10^{-5}
5.0	0.26	0.030	0.093	6.72×10^{-5}
4.5	0.29	0.010	0.15	2.06×10^{-4}
4.0	0.33	0.024	0.14	1.06×10^{-3}
3.5	0.37	0.035	0.11	6.38×10^{-3}
3.0	0.43	0.042	0.16	3.18×10^{-2}
2.5	0.54	0.044	0.27	1.04×10^{-1}
2.0	0.71	0.038	0.40	2.69×10^{-1}
1.8	0.79	0.040	0.41	3.76×10^{-1}

Table 3-2. Fitting parameters of [Co$_{0.055}$Zn$_{0.945}$L$_2$] in an applied static magnetic field of 1000 Oe.

T / K	χ_t / cm^3 mol^{-1}	χ_s / cm^3 mol^{-1}	a	τ / s
5.5	0.23	0.029	0.062	3.28×10^{-5}
5.0	0.25	0.020	0.056	8.98×10^{-5}
4.5	0.28	0.023	0.10	2.99×10^{-4}
4.0	0.32	0.0014	0.14	1.35×10^{-3}
3.5	0.36	0.010	0.096	8.78×10^{-3}
3.0	0.42	0.015	0.066	5.30×10^{-2}
2.5	0.51	0.017	0.11	2.31×10^{-1}
2.0	0.70	0.017	0.22	8.26×10^{-1}
1.8	0.80	0.017	0.25	1.28

The natural logarithm of relaxation time τ versus inverse of temperature $1/T$ plots (Arrhenius plots) exhibited high linearity at high temperature region between 5.5 to 3.5 K ($R^2 = 0.999$, 5 points) for both **2** and **dil.2**. which indicate Arrhenius behaviors or Orbach relaxations at these temperatures. From the slopes and intercepts of the straight lines, the effective energy barriers U_{eff} of 38.0 cm^{-1} and 37.4 cm^{-1}, preexponential factors τ_0 of 1.31×10^{-9} s and 1.84×10^{-9} s were extracted for **2** and **dil.2**, respectively. Almost identical U_{eff}'s implied that the reducing intermolecular interactions has only small effect on high temperature relaxation processes under applied static magnetic field of 1000 Oe in this complex. Furthermore, obtained U_{eff}'s were smaller than the zero-field splitting obtained by magnetization measurements ($|2D| \fallingdotseq 54.2$ cm^{-1}). However, these situations are frequently observed in other mononuclear systems.[17]
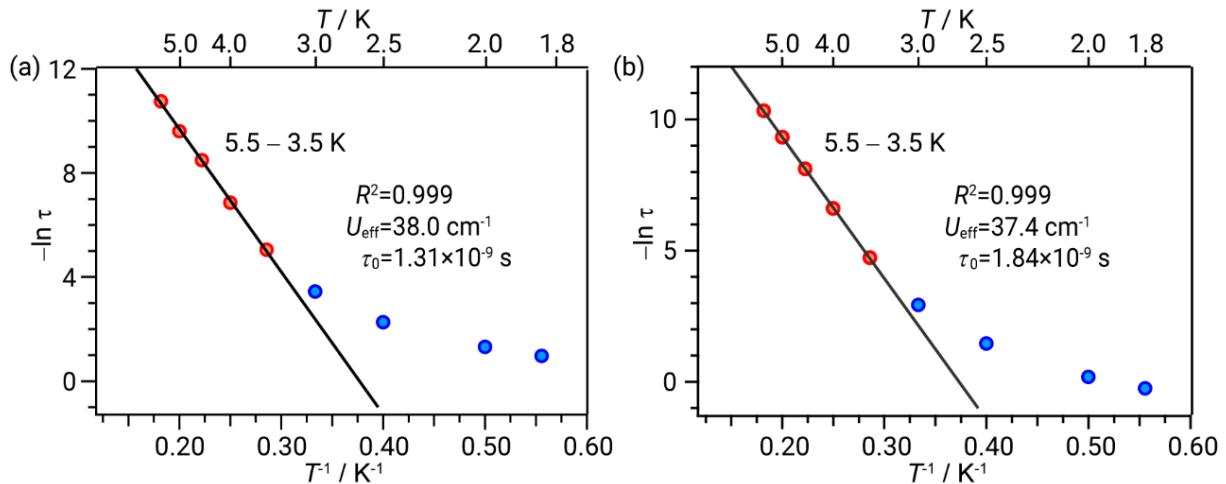
**Fig. 3-11.** Natural logarithm of the magnetization relaxation time of (a) **2** and (b) **dil.2** against the inverse of the temperature at $H_{dc} = 1000$ Oe. The regression line obtained in the temperature range of 5.5 – 3.5 K is shown. The correlation factor (R^2) for the regression, effective energy barrier (U_{eff}), and preexponential factor (τ_0) are also given.

In order to get deeper information of the effect of intermolecular interactions on magnetic relaxations at low temperatures, ac susceptibility measurements at 2.0 K in variable static magnetic field were investigated on both **2** and **dil.2**. The small uplift at high ac frequency observed in the absence of static magnetic field become larger and the peak is shifted to lower frequency up to 1000 Oe for **2** (Figure 3-12(a)). In the case of **dil.2**, the small peak situated in ca. 20 Hz increased and shifted to lower frequency with increasing dc field up to 1000 Oe. This is the same tendency with **2**, however, the peaks were much sharper in **2**. Further field increase shifted the peak to higher frequency (Figure 3-14), which means that relaxations were decreased with excessive external magnetic field. This is typical behavior of direct relaxation process.[20] On the other hand, the shoulder recognized at high frequency was decreased with increasing dc field (Figure 3-12(b)). The prepared Cole-Cole plots were reproduced by employing the Debye model (Figure 3-13, 3-15). For **2**, two relaxation components are needed to obtain a good fit especially in a dc field of 300 and 500 Oe, which indicate that two relaxation components are largely overlapped in these conditions (Table 3-3). For **dil.2**, clearly two separated semi-circles are observed in the dc field up to 1000 Oe (Figure 3-13 (b)). These plots were fitted by two relaxation components (Table 3-4). Above dc field of 1000 Oe, employing only one relaxation time afforded good fit of experimental Cole-Cole plots (Figure 3-15).

These analyses indicated that the peak observed at low frequency in **dil.2** shows typical static field dependence of quantum tunneling and direct processes, which means the ac signals is intramolecular origin. While other peaks observed as the shoulders at high frequency in **dil.2** and overlapped to intramolecular origin signals in **2** are expected the intermolecular component, as they are monotonically decreased with increasing dc field. The above consideration indicates the intramolecular relaxation components are large affected by intermolecular components. The

73

broader and peak implies that it may cause a shortcut of the spin-lattice relaxations by dominant tunnelling relaxation processes even in applied dc field and the reason of unclear structures of χ'' signals in zero dc field for both **2** and **dil.2**. This may explain the obtained smaller U_{eff}'s than zero-field splittings, however, the overestimation of axial ZFS parameter D cannot be excluded.
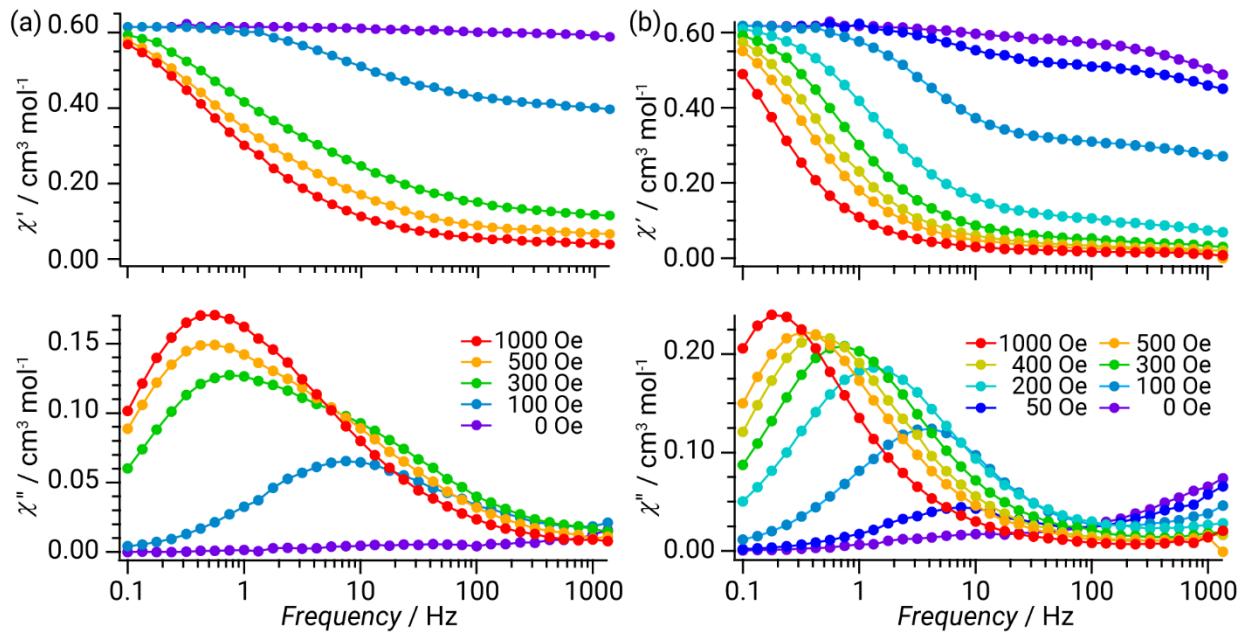
Figure 3-12. Frequency dependence of χ' and χ'' plots of (a) **2** and (b) **dil.2** at 2.0 K in indicated static magnetic field.
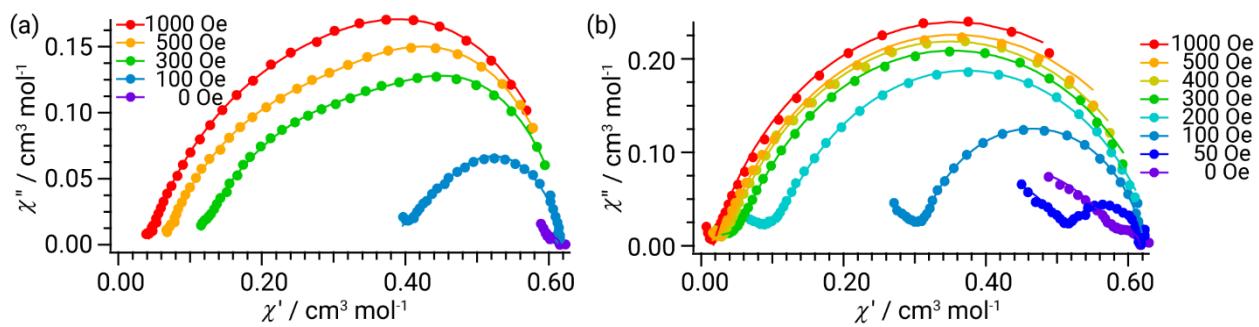
**Figure 3-13.** Cole-Cole plots of (a) **2** and (b) **dil.2** at 2.0 K in a static field between 0 - 1000 Oe.
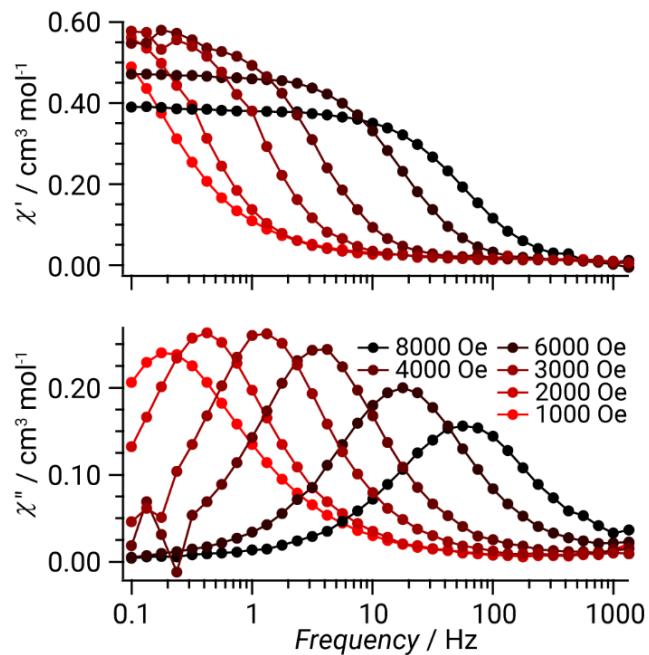
**Figure 3-14.** Frequency dependence of χ' and χ'' plots of **dil.2** at 2.0 K in a static magnetic field between 1000 - 8000 Oe.
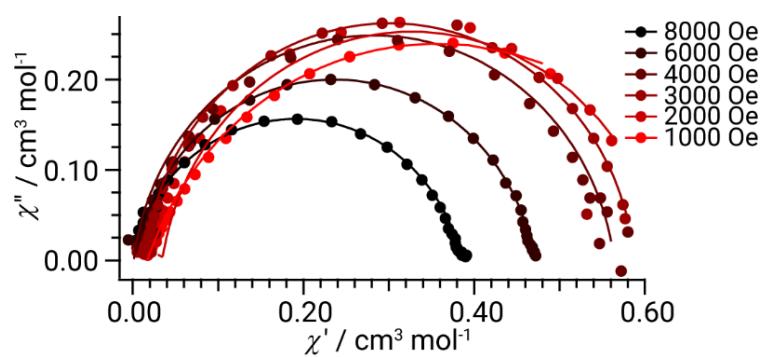

Figure 3-15. Cole-Cole plot of **dil.2** at 2.0 K in a static magnetic field between 1000 - 8000 Oe.

Table 3-3. Fitting parameters of **2** at 2.0 K

H / Oe	χ_t / cm^3 mol^{-1}	χ_s / cm^3 mol^{-1}	α_1	τ_1 / s	Weight of τ_1	α_2	τ_2 / s
0	0.62	0.55	0.29	7.07×10^{-3}	0.25	0.15	4.07×10^{-5}
100	0.62	0.38	0.21	2.30×10^{-2}	0.67	0.48	9.75×10^{-4}
300	0.64	0.11	0.05	3.55×10^{-1}	0.26	0.44	3.86×10^{-2}
500	0.63	0.061	0.10	4.81×10^{-1}	0.37	0.40	5.11×10^{-2}
1000	0.64	0.039	0.13	5.24×10^{-1}	0.38	0.36	9.02×10^{-2}

Table 3-4. Fitting parameters of **dil.2** at 2.0 K.

H / Oe	χ_t / cm^3 mol^{-1}	χ_s / cm^3 mol^{-1}	α_1	τ_1 / s	Weight of τ_1	α_2	τ_2 / s
0	0.62	0.28	0.13	2.29×10^{-2}	0.084	0.37	3.99×10^{-5}
50	0.62	0.22	0.12	2.48×10^{-2}	0.24	0.37	2.63×10^{-5}
100	0.62	0.078	0.14	4.32×10^{-2}	0.57	0.37	1.80×10^{-5}
200	0.64	0.0096	0.22	1.17×10^{-1}	0.84	0.47	7.16×10^{-5}
300	0.65	-0.010	0.22	2.15×10^{-1}	0.89	0.64	7.84×10^{-5}
400	0.66	-0.015	0.22	3.31×10^{-1}	0.91	0.69	6.97×10^{-5}
500	0.69	-0.011	0.22	4.72×10^{-1}	0.91	0.80	9.53×10^{-4}
1000	0.70	0.017	0.22	8.26×10^{-1}	0.96	0.40	3.20×10^{-5}
2000	0.62	0.017	0.093	3.79×10^{-1}	-	-	-
3000	0.59	0.014	0.057	1.22×10^{-1}	-	-	-
4000	0.56	0.0011	0.079	4.58×10^{-2}	-	-	-
6000	0.47	0.0025	0.10	9.16×10^{-3}	-	-	-
8000	0.39	-0.0031	0.14	2.80×10^{-3}	-	-	-

In order to rationalize the relaxation behaviour of **2** molecule, the temperature- and static field-dependence of relaxation times of **dil.2** were simultaneously fitted by following equation, which considered spin-lattice relaxation processes (direct, Raman and Orbach) and quantum tunnelling process. [21,22]

$$\tau^{-1} = AH^5 \coth(g\mu_B H/2k_B T) + CT^n + \tau_0^{-1} \exp(U_{\text{eff}}/k_B T) + d\frac{1 + eH^2}{1 + fH^2}$$

The A is coefficient of direct process, and C and n are those of Raman process, d, e and f are coefficient of QTM. In the QTM term, the coefficients d, e and f represent the relaxation rate in zero dc field, the effect of interacting spins and the ability of the external dc field to suppress the mechanism, respectively. In this fitting, g value determined by magnetization fitting was used (g = 2.104), and the Orbach coefficients U_{eff} and τ_0 were fixed to the values obtained by the Arrhenius plot. The QTM and direct coefficients were uniquely determined from the static field dependence of τ at 2.0 K, and determining the Raman coefficients, the best fit was obtained by following parameters: $A = 3.0 \times 10^2$ s^{-1} T^{-5}, $C = 1.0 \times 10^{-2}$ s^{-1} K^{-n}, $n = 6.2$, $d = 55$ s^{-1}, $e = 0$, $f = 1.6 \times 10^4$ T^{-2} (Figure 3-15). It is noted that the intermolecular interactions on magnetic relaxations were not necessary to improve the fitting (i.e. $e = 0$). The obtained n (6.2) is smaller than that of Kramers systems of 9, however, this value is allowed in the presence of low-lying excited states.[23] Furthermore, rational fits considering the U_{eff} equal to ZFS ($|2D| \approx 54.2$ cm^{-1}) could not obtained.[24]
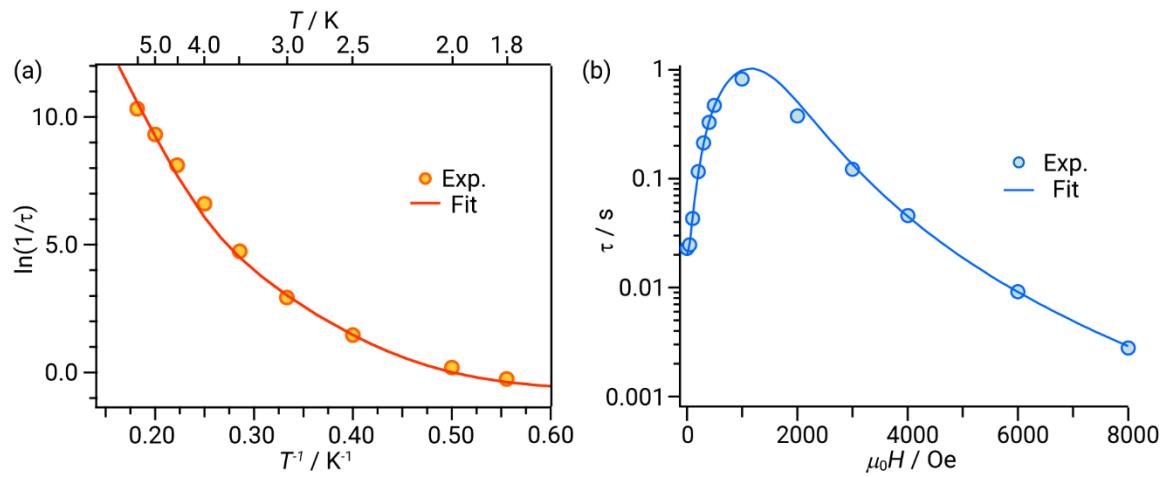
**Figure 3-16.** Relaxation time fitting of **dil.2** with eq.2 in applied static field of 1000 Oe and (inset) at 2.0 K in variable static field with fixed U_{eff} and τ_0 are from Arrhenius plot ($A = 3.0 \times 10^2$ s^{-1} T^{-5}, $C = 1.0 \times 10^{-2}$ s^{-1} K^{-n}, $n = 6.2$, $U_{eff} = 37.4$ cm^{-1}, $\tau_0 = 1.84 \times 10^{-9}$ s, $d = 55$ s^{-1}, $f = 1.6 \times 10^4$ T^{-2}).

3-3-4 *Ab initio* calculations

In order to get insight of electronic structure of **2**, *ab initio* calculations were performed on ORCA 4.0.1.2 package.[25-27] The input structure was taken from the X-ray structure with substituting from octyl chains to methyl group to reduce the calculation cost. The CAS(7,5) SCF were performed and the 10 spin quartets and 35 doublets were included in the CAS space, then dynamic corrections were recovered by the NEVPT2 program. The largest contribution to the axial anisotropic parameter D was derived from first excited quartet (Table 3-5). The resultant anisotropic and g-parameters were as follows: $D = -30.7$ cm^{-1} and $|E/D| = 0.012$, $g_x = 2.117$, $g_y = 2.136$, $g_z = 2.493$, ($g_{iso} = 2.249$). Obtained large negative D value supported the large Ising anisotropy of **2**, which was indicated by static magnetic measurements. The direction of anisotropic axis is indicated in Figure 3-17. The easy axis (D_{ZZ}) was indicated along the direction of bisect bite angle between Co and bidentate ligands. Similar results were also reported in other tetrahedral Co(II) systems comprised of two bidentate ligands with small bite angles.[1,18] The magnitude of $|D|$ was comparable with the magnetization and magnetic susceptibility results. The relatively small E value of 0.036 cm^{-1} indicated small rhombic anisotropy, or small energetically difference between x- and y- directions of **2**. The ALFET program was performed to obtain one-electron wavefunctions of five 3d orbitals (Table 3-6). The 3d-based orbitals laid at the lowest and the second lowest were fully occupied and have large contribution of d$_{z2}$ orbital (-0.935), and d$_{xy}$ orbital (0.994), respectively. The latter one lay at 711.2 cm^{-1} higher than the lowest one. The remained three orbitals were half-filled. The third lowest one manly consisted of d$_{x2-y2}$ lying at 3098 cm^{-1}. The fourth and fifth ones were situated at 7256 cm^{-1} and 7947 cm^{-1} from ground one, respectively, and they had mixed contributions of d$_{yz}$ and d$_{zx}$ orbitals. The large contribution for

axial contribution would be derived from the relatively small energy gap between d_{xy} and d_{x2-y2} orbitals.[28,29]

Table 3-5. Contribution of anisotropic parameters on ground spin quartet.

| Multiplet	Root	D / cm^{-1}	E / cm^{-1}	Multiplet	Root	D / cm^{-1}	E / cm^{-1}
4	0	0	0	2	13	0.083	0
4	1	−45.358	0.015	2	14	−0.194	0.192
4	2	5.758	0.457	2	15	−0.033	−0.021
4	3	5.908	−1.434	2	16	0.008	−0.015
4	4	0.807	0.125	2	17	−0.014	−0.017
4	5	0.158	−0.062	2	18	−0.012	−0.028
4	6	0.049	−0.005	2	19	0.011	0.013
4	7	0.002	0	2	20	−0.04	0.039
4	8	0.001	−0.001	2	21	−0.595	−0.609
4	9	−0.001	−0.001	2	22	−0.106	−0.112
2	0	−0.3	−0.252	2	23	−0.685	0.685
2	1	−0.469	0.096	2	24	−0.003	0.003
2	2	−0.033	0.036	2	25	0.158	0.001
2	3	0.045	−0.033	2	26	0.012	−0.001
2	4	0	0.012	2	27	−0.004	0.002
2	5	0.076	0.01	2	28	−0.002	0
2	6	6.086	−0.02	2	29	0.299	-0.003
2	7	−1.477	−0.742	2	30	−0.052	−0.057
2	8	−2.029	0.15	2	31	−0.086	0.076
2	9	−0.843	0.133	2	32	−0.019	0.013
2	10	1.028	0.005	2	33	−0.014	−0.011
2	11	−0.097	−0.047	2	34	0	0
2	12	0.005	0.002				
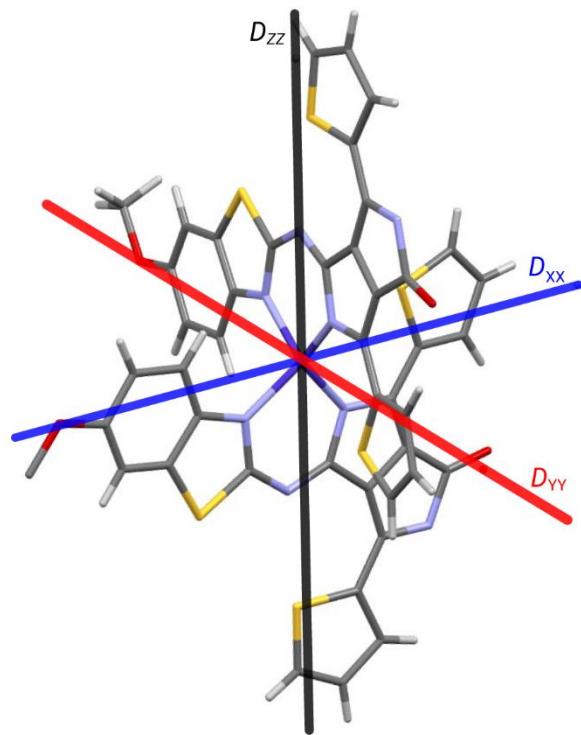
Figure 3-17. Direction of anisotropic axes for **2** obtained from *ab initio* calculations.

Table 3-6. One electron eigenfunctions derived on the AILET program.

Orbital	*Energy* / cm^{-1}	d_{xy}	d_{yz}	d_{z2}	d_{xz}	d_{x2-y2}
1	0	0.086	-0.241	-0.935	0.172	0.178
2	711.2	0.994	-0.0349	0.092	-0.004	-0.041
3	2925.8	0.035	0.234	0.138	0.069	0.959
4	6822.3	-0.025	-0.661	0.074	-0.718	0.203
5	7250.4	-0.046	-0.67	0.306	0.671	0.073

3-4 Conclusion

The mononuclear tetrahedral four-coordinate Co(II) complex having bidentate ligands composed of pyrrolopyrrole and benzothiazole moieties exhibited significant slow magnetic relaxation in an applied static magnetic field, in which significant quantum tunneling process induced by significant intermolecular interactions through 3-dimentional hydrogen bond was disturbed the observation of ac signals in no applied dc field. In static field of 1000 Oe, frequency dependence of χ'' peaks was observed on both **2** and **dil.2**. Employing fitting with generalized Debye model afforded larger relaxation time τ and smaller dispersion coefficients α for **dil.2** at all measured temperatures. However, prepared Arrhenius plots afforded almost identical effective energy barriers U_{eff}'s, which implies that the relaxation path via intermolecular interactions have small effects at high temperature region in an applied static field of 1000 Oe. However, ac peaks and extracted relaxation times are significantly different at low temperatures. The comparison between **2** and **dil.2** in variable static magnetic field indicated that broad χ'' peak in **2** is attributed to intermolecular interactions. The magnetic dilution successfully separated the intermolecular and intramolecular relaxation components. The extracted temperature- and static field-dependence of relaxation times τ of **dil.2** was successfully reproduced by considering spin-lattice relaxation and tunneling processes.

3-5 References

1. Ishizaki, T.; Fukuda, T.; Akaki, M.; Fuyuhiro, A.; Hagiwara, M.; Ishikawa. N. Synthesis of a Neutral Mononuclear Four-Coordinate Co(II) Complex Having Two Halved Phthalocyanine Ligands That Shows Slow Magnetic Relaxations under Zero Static Magnetic Field. *Inorg. Chem.* **2019,** *58*, 5211-5220**.**

2. Wernsdorfer, W.; Aliaga-Alcalde, N.; Hendrickson, D. N.; Christou, G. Exchange-biased quantum tunnelling in a supramolecular dimer of single-molecule magnets. *Nature* **2002**, *416*, 406-409.

3. Hill, S.; Edwards, R. S.; Aliaga-Alcalde, N.; Christou, G. *Science* **2003**, *302*, 1015-1018.

4. Mitsuhashi, R.; Hosoya, S.; Suzuki, T.; Sunatsuki, Y.; Sakiyama, H.; Mikuriya, M. Hydrogen-bonding interactions and magnetic relaxation dynamics in tetracoordinated cobalt(II) single-ion magnets. *Dalton Trans.* **2019**, *48*, 395-399.

5. Habib, F.; Korobkov, I.; Murugesu, M. Exposing the intermolecular nature of the second relaxation pathway in a mononuclear cobalt(II) single-molecule magnet with positive anisotropy. *Dalton Trans.* **2015**, *44*, 6368-6373.

6. Boća, R.; Rajnák, C.; Moncol, J.; Titiš, J.; Valigura, D.; Breaking the Magic Border of One Second for Slow Magnetic Relaxation of Cobalt-Based Single Ion Magnets. *Inorg. Chem.* **2018**, *57*, 14314-14321.

7. Miklovič, J.; Valigura, D.; Boča, R.; Titiš, J. A mononuclear Ni(II) complex: a field induced single-molecule magnet showing two slow relaxation processes. *Dalton Trans.* **2015**, *44*, 12484−12487.

8. R. Boča, C. Rajnák, J. Titiš, D. Valigura, Field Supported Slow Magnetic Relaxation in a Mononuclear Cu(II) Complex. *Inorg. Chem.* **2017**, *56*, 1478−1482.

9. Shimizu, S.; Iino, T.; Araki, Y.; Kobayashi, N. Pyrrolopyrrole aza-BODIPY analogues: a facile synthesis and intense fluorescence. *Chem. Commun.* **2013**, *49*, 1621-1623.

10. Loudet A.; Burgess, K. BODIPY Dyes and Their Derivatives: Syntheses and Spectroscopic Properties. *Chem. Rev.* **2007**, *107*, 4891-4932.

11. Shimizu, S.; Iino, T.; Saeki, A.; Seki, S.; Kobayashi, N. Rational Molecular Design towards Vis/NIR Absorption and Fluorescence by using Pyrrolopyrrole aza-BODIPY and its Highly Conjugated Structures for Organic Photovoltaics. *Chem. Eur. J.* **2015**, *21*, 2893-2904.

12. Kage, Y.; Karasaki, H.; Mori, S.; Furuta, H.; Shimizu, S. Pyrrolopyrrole Aza-BODIPY Analogues as Near-Infrared Chromophores and Fluorophores: Red-Shift Effects of Substituents on the Absorption and Emission. *ChemPlusChem* **2019**, *84*, 1648-1652.

13. Bain, G. A.; Berry, J. F. Diamagnetic Corrections and Pascal's Constants. *J. Chem. Educ.* **2008**, *85*, 532−536.

14. Neese, F. ORCA - *An ab Initio, Density Functional and Semiempirical Program Package*, version 4.0; **2017**.

15. Neese, F. Software Update: The ORCA Program System, version 4.0. *WIREs Comput. Mol. Sci.* **2018**, *8*, e1327.

16. Neese, F. ORCA Program System. *WIREs Comput. Mol. Sci.* **2012**, *2*, 73−78.

17. Frost, J. M.; Harriman, K. L. M.; Murugesu, M. The rise of 3-d single-ion magnets in molecular magnetism: towards materials from molecules? *Chem. Soc.* 2016, 7, 2470-2491.

18. Ziegenbalg, S.; Hornig, D.; Görls, H.; Plass, W. Cobalt(II)-Based Single-Ion Magnets with Distorted Pseudotetrahedral [N_2O_2] Coordination: Experimental and Theoretical Investigations. *Inorg. Chem.* **2016**, *55*, 4047−4058.

19. S. Tripathi, S. Vaidya, K. U. Ansari, N. Ahmed, E. Rivière, L. Spillecke, C. Koo, R. Klingeler, T. Mallah, G. Rajaraman, M. Shanmugam. Influence of a Counteranion on the Zero-Field Splitting of Tetrahedral Cobalt(II) Thiourea Complexes. *Inorg. Chem.* **2019**, 58, 9085−9100.

20. Fukuda, T.; Shigeyoshi, N.; Yamamura, T.; Ishikawa. N. Magnetic Relaxations Arising from Spin−Phonon Interactions in the Nonthermally Activated Temperature Range for a Double-Decker Terbium Phthalocyanine Single Molecule Magnet. *Inorg. Chem.* **2014**, *53*, 9080-9086.

21. Fort, A.; Rettori, A.; Villain, J.; Gatteschi, D.; Sessoli. R.; Mixed Quantum-Thermal Relaxation in Mn12 Acetate Molecules. *Phys. Rev. Lett.* 1998, 80, 612-615.

22. Vleck, J. H. V. Paramagnetic Relaxation Times for Titanium and Chrome Alum. *Phys. Rev.* **1940**, *57*, 426-447.

23. Shrivastava, K. N. Theory of Spin–Lattice Relaxation. *phys. stat. sol.* **1983**, *117*, 437-458.

24. Rechkemmer, Y.; Breitgoff, F. D.; Meer, M. V. D.; Atanasov. M.; Hakl, M.; Orlita, M.; Neugebauer, P.; Neese, F.; Sarkar, B.; Slageren, J. V. A four-coordinate cobalt(II) single-ion magnet with coercivity and a very high energy barrier. *Nat. Commun.* **2016**, *7*, 10467-10484.

25. Neese, F. ORCA - *An ab Initio, Density Functional and Semiempirical Program Package*, version 4.0; 2017.

26. Neese, F. Software Update: The ORCA Program System, version 4.0. *WIREs Comput. Mol. Sci.* **2018**, *8*, e1327.

27. Neese, F. ORCA Program System. *WIREs Comput. Mol. Sci.* **2012**, *2*, 73−78.

28. Zadrozny, J. M.; Long. J. R. Slow Magnetic Relaxation at Zero Field in the Tetrahedral Complex $[Co(SPh)_4]^{2-}$. *J. Am. Chem. Soc.* **2011**, *133*, 20732-20734.

29. Vaidya, S.; Upadhyay, A.; Singh, S. K.; Gupta, T.; Tewary, S.; Langley, S. K.; Walsh, J. P. S.; Murray, K. S.; Rajaraman, G.; Shanmugam. M.; A synthetic strategy for switching the single ion anisotropy in tetrahedral Co(II) complexes. *Chem. Commun.* **2015**, *51*, 3739-3742.

Chapter 4

Synthesis and observations of slow magnetic relaxation

phenomena of a tetrahedral four-coordinate mononuclear

copper(II) complex consisting of bis-phenyl-bisisoindole-

aza-methene ligands

4-1 Introduction

4-1-1 Slow magnetic relaxations of mononuclear transition metal complexes with easy-plane magnetic anisotropy

Although the easy-axis type of magnetic anisotropies are essential for the observation of slow magnetic relaxations in transition metal clusters and lanthanide systems,[1-2] the phenomena based on the easy-plane type of magnetic anisotropies have been reported only for several mononuclear transition metal complexes.[3] The first report is the square-pyramidal five-coordinate mononuclear Co(II) complex which shows slow magnetic relaxations only in an applied static magnetic field of 2000 Oe, in which the positive axial magnetic parameter D of $+12.7$ cm^{-1} was determined by high-field, multi-frequency ESR measurements.[4] In the paper, The high temperature relaxation process is assigned by Orbach relaxation process the mixing of the ground sublevels $M_S = \pm 1/2$ and the first excited sublevels $M_S = \mp 3/2$ through rhombic anisotropy E, owing to the almost equal experimental effective energy barrier U_{eff} and zero-field splitting (ZFS).[1] On the one hand, it is difficult to rationalize the relaxation mechanisms when the ZFS is much larger than U_{eff}.[5,6] In addition, the direct and QTM relaxation processes for half-integral spin systems are theoretically forbidden by degeneracy of two same magnitude of quantum states in no static field. However, Gómez-Coca *et al.* demonstrated that these processes were partially permitted through the entanglements of electron and nuclear spins in an applied static magnetic field, and they successfully explained the relaxation mechanisms of [Co(acac)$_2$(H$_2$O)$_2$] with large positive D are dominated by the Raman and direct processes.[7]

4-1-2 Slow magnetic relaxations with an $S = 1/2$ effective spin

The reference 7 afforded the rational explanation about the slow relaxations on the $S_{eff} = 1/2$ systems. In mononuclear transition metal complexes with $S = 1/2$, slow magnetic relaxations were reported for V(IV),[8-12] low-spin Mn(IV),[13] low-spin Co(II),[14] Ni(I),[15-16] low-spin Ni(III),[17] Co(II)[18-19] and Ru(III)[20] complexes. However, the origin of the slow relaxations is still unclear. In the low-spin d^7 Ni(III) cyclam complexes with two axial nitrate ligands exhibits slow magnetic relaxations in an applied static magnetic field, while the complex with two axial isothiocyanato (NCS) ligands does not show slow relaxations even in an applied static magnetic field.[17] In the d^9 Ni(I) complexes, three coordinate geometry afforded slow relaxations in an applied static magnetic field, while tetrahedral geometry does not show slow magnetic relaxations, which implied that the dynamic magnetic properties on $S = 1/2$ systems are sensitive to the ligand-metal bonds and the coordination geometries around the metal centers.[16] In d^9 Cu(II) complexes, slow magnetic relaxations were firstly reported by Boca *et. al.*, in which multiple relaxations may be due to the intermolecular interactions at low temperature disturb the rationalizations of the relaxation mechanisms.[18]
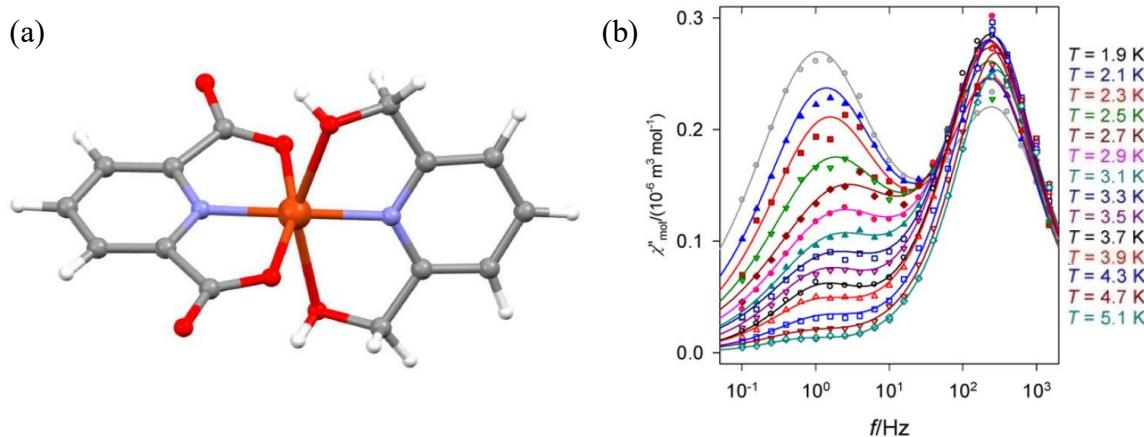

Figure 4-1. (a) Structure of [Cu(pydca)(dmpy)]·0.5H$_2$O and (b) frequency dependence of out-of-phase susceptibilities of [Cu(pydca)(dmpy)]·0.5H$_2$O in applied static field of 5000 Oe.

4-1-3 The bisphenyl-bisisoindole-aza-methene ligand

The bisphenyl-bisisoindole-aza-methene (half-Pc$_{Ph}$) has a structure of aza-bridged bisisoindoles with two terminal phenyl rings. The metal-free form of the ligand has large absorptions in the visible and NIR region. The boron complexes are well known as the aza-boron dipyrrolomethene (aza-BODIPY), and expected for bio imagings, fluorescent materials.[21] In first row transition metal ions, the homoleptic Co(II), Ni(II), Cu(II), Zn(II) and Hg(II) mononuclear complexes composed of the ligands are reported, together with the optical and electrochemical propersites.[22] In the report, the Co and Zn complexes are structurally determined by the X-ray analyses. Interestingly, the dihedral angles between the central metal ion and two bisisoindoles are much smaller than ideal tetrahedron (90 °) of 68.0(6) and 66.7(9) ° for the Co and Zn complexes, respectively, owing to the intramolecular interactions between the terminal phenyl rings and bisisoindole units. The dynamic magnetic properties of distorted tetrahedral four-coordination geometry around the central ions are interested.
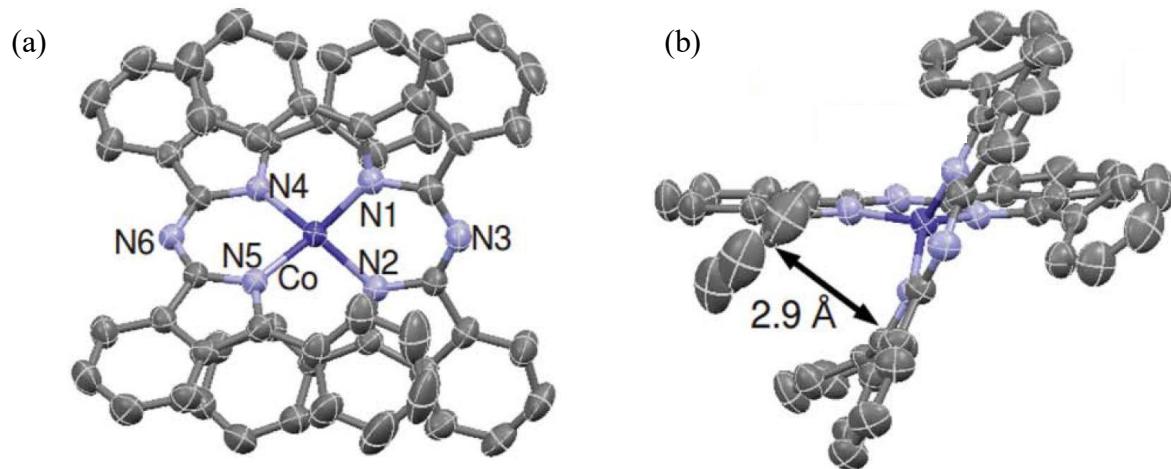

Figure 4-2. (a) Top view and (b) side view of the Co(II) complex composed of bisphenyl-bisisoindole-aza-methene ligands.

4-2 Experimental Section

4-2-1 Syntheses of bisphenyl-bisisoindole-aza-methene ligand

Syntheses of bisphenyl-bisisoindole-aza-methene (half-Pc$_{Ph}$) ligand and the copper(II) complex were performed according to the previous reports with some modifications.[21,22] A dry diethyl ether solution of phenyl Grignard was dropped to a dry toluene solution (30 ml) of 1,2-dicyanobenzene (450 mg, 3.51 mmol) at 0 °C and the mixture was stirred for 2 h. Water (10 ml) and aqueous saturated ammonium chloride (10 ml) were added to the reactant solution followed by the evaporation of the solvent at 120 °C for 1 h. The blue solid was dissolved in dichloromethane and washed with water. The extracted organic solvent was dried by adding anhydrous sodium sulfate and the residue was purified by silica column chromatography with CH$_2$Cl$_2$ as eluent to afforded a blue solid (yield 18.2 %).

4-2-2 Synthesis of [Cu(half-Pc$_{Ph}$)], **3**

The copper(II) complex **3** was synthesized through refluxing the bisphenyl-bisisoindole-aza-methene (half-Pc$_{Ph}$) ligand (200 mg, 0.50 mmol), Cu(CH$_3$COO)$_2$ monohydride (131 mg, 0.654 mmol, 1.3 eq) and *N,N*-diisopropylethylamine (DIPEA, 2 eq) in dry tetrahydrofuran (THF) (10 ml) for 6 h. The blue precipitate was filtrated and washed with methanol (yield 47.4 %). MS (ESI): *m*/z: 856.23702 [CuC$_{56}$N$_6$H$_{36}$] +H $^+$. Anal. Calcd (%) for CuC$_{56}$N$_6$H$_{36}$: C 78.53, H 4.24, N 9.81. Found: C 78.01, H 4.38, N 9.62.

4-2-3 Preparation of $[Cu_{0.037}Zn_{0.963}(half\text{-}Pc_{Ph})_2]$ (**dil.3**)

A mixture of **3** and $[Zn(half\text{-}Pc_{Ph})_2]$ in the molar ratio of 3.7 : 96.3 was dissolved in CH_2Cl_2 and passed through a celite column. The eluent was collected, concentrated in vacuo and dried under reduced pressure at 50 ℃ for 1 day.

4-3 Measurements

Elemental analysis was performed by a YANACO CHN Corder MT-6 analyzer. Mass spectra were obtained using a Thermo Fisher Scientific Orbitrap XL (ESI-LIT-orbitrap) spectrometer. Single crystal X-ray diffractions were collected with a Rigaku R-AXIS VII diffractometer using filtered Mo Kα (λ = 0.71075 Å) radiation. The refinement with full-matrix least-squares techniques was carried out with SHELXL-2014/7.[23]

Static magnetic properties were collected using a Quantum Design MPMS-XL7AC SQUID magnetometer. The sample was prepared by wrapping 12.43 mg (1.45×10^{-5} mol) of **3** in an aluminum foil of 43.46 mg and fixed by eicosane of 13.68 mg. Diamagnetic components were estimated using the Pascal constants,[24] and the contribution from the aluminum foil was corrected on the basis of the blank measurement. Ac measurements were performed on a Quantum Design MPMS-XL7AC (0.1-1340 Hz) with employing oscillating magnetic field of 3.9 Oe. The undiluted sample was prepared by fixing 15.45 mg of **3** in a gelatin capsule using eicosane of 13.14 mg. The diluted sample was prepared by fixing **dil.3** (126.83 mg) in a plastic straw using eicosane.

Continuous-wave X-band (9.211 GHz) electron spin resonance (ESR) spectra of 3.7% magnetically diluted **3** [$Cu_{0.037}Zn_{0.963}$(half-Pc$_{Ph}$)$_2$] (**dil.3**) were measured on JEOL RESONANCE JES X320 with at 123 K. Simulations of ESR spectra were performed using Anisotropic simulation implemented in an AniSimu/FA Version 2.4.0 software.

4-4 Results and Discussion

4-4-1 Synthesis and characterizations

Synthesis of the bisphenyl-bisisoindole-aza-methene (half-Pc$_{Ph}$) ligand was performed by the reaction of 1,2-dicyanobenzene and a Grignard reagent of phenyl magnesium bromide. Heating the reaction mixture in dry toluene afforded blue precipitate, and the target compound was isolated and purified by silica gel column chromatography. The copper(II) complex **3** was synthesized by refluxing copper(II) acetate and the half-Pc$_{Ph}$ ligand in dry tetrahydrofuran (THF) in the presence of diisopropylethylamine (DIEPA) as a base.
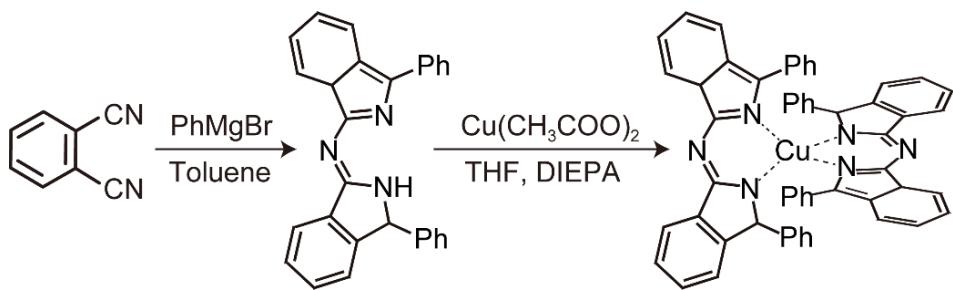
Scheme 1. Synthesis of bisphenyl-bisisoindole-aza-methene (half-Pc$_{Ph}$) ligand and the copper complex **3**.

Single crystals of **3** were obtained by slow diffusion of methanol in dichloromethane solution of **3**. Single crystal X-ray diffraction revealed that **3** was crystalized in the triclinic $P\bar{1}$ (Table 4-3). The central copper ion is coordinated by four nitrogen atoms of the two bisisoindole ligands (Figure 4-3(a)). Because of the intermolecular interactions between the isoindoles and terminal phenyl rings, the copper ion of **3** has the distorted tetrahedral coordination geometry with the dihedral angle between the two ligands of 65.85° (Figure 4-1(b)). This value is smaller than that of the Co and Zn congerners (for 68.0(6) and 66.7(9) °, respectively). This would be attributed to

96

the preferential planer confirmations of Cu(II) ions. The Cu-N bond lengths are in the range of 1.955(2) to 1.968(2) Å (Table 4-2). The N-Cu-N bond angles are in the range of 94.48(9) (for N1-Cu-N2) to 133.29(11) (for N1-Cu-N5). The shortest intermolecular Cu-Cu distance is 8.165 Å (Figure 4-4).
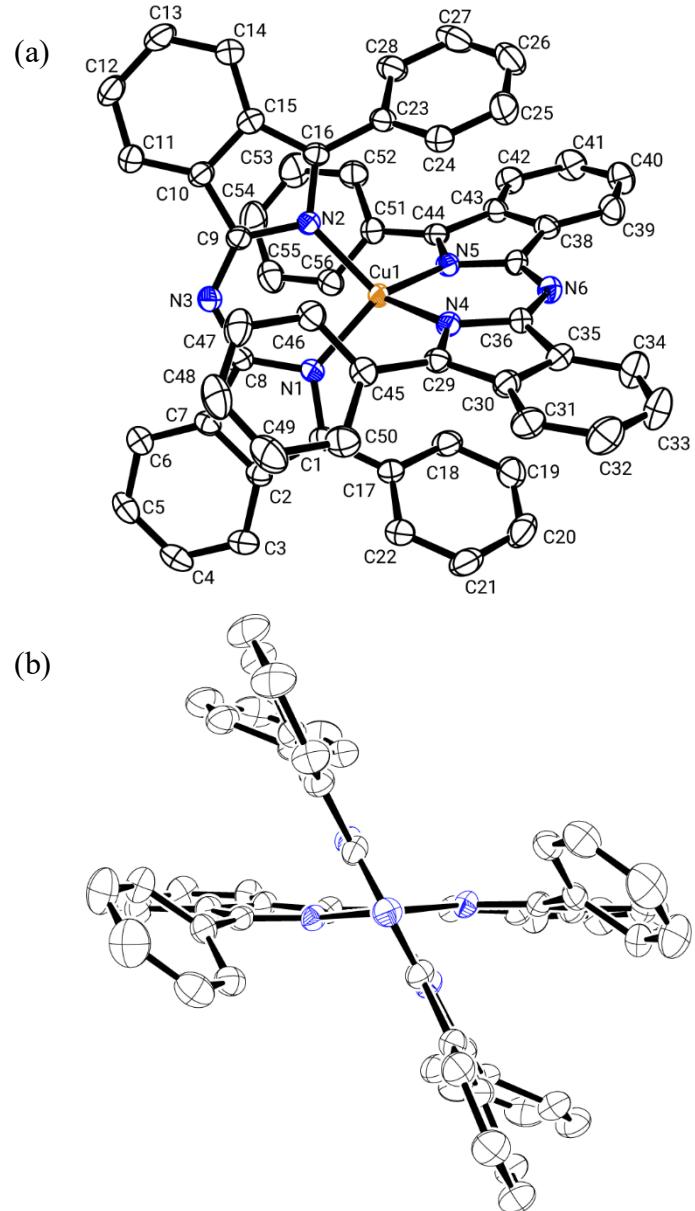

Figure 4-3. Ortep diagrams of (a) top and (b) side view of **3** (50% probability ellipsoids). Hydrogen atoms are omitted for clarity.
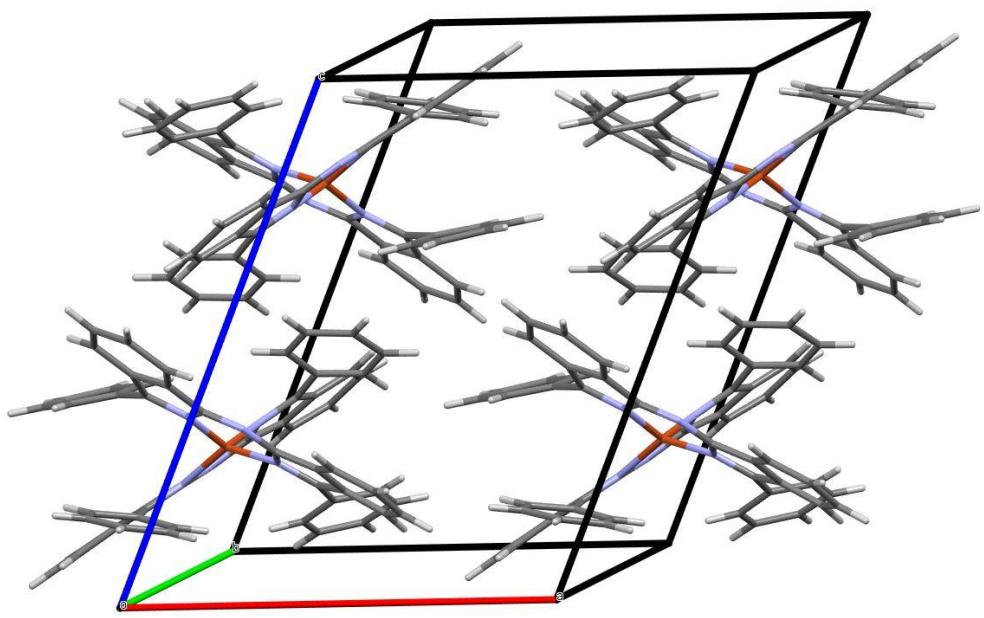
Figure 4-4. Crystal packing of **3**.

Table 4-1. Selected crystal structural parameters for [Cu(half-Pc$_{Ph}$)$_2$] (**3**).

	[Cu(half-Pc$_{Ph}$)$_2$], **3**
Empirical Formula	C$_{57}$H$_{38}$Cl$_2$CuN$_6$
Formula Weight	941.42
Crystal System	*triclinic*
a / Å	12.5358(3)
b / Å	13.0926(3)
c / Å	16.4085(3)
a / °	67.782(5)
β / °	67.509(5)
γ / °	68.941(5)
V / Å^3	2229.77(13)
Space Group	$P\bar{1}$ (No.2)
Z value	2
D_{calc}/ g cm^{-3}	1.402
Temperature / °C	-73.0
No. of Observations	10113
R_1	0.0559
wR_2	0.1537

Table 4-2. Bond lengths for **3**.

Cu1-N1	1.961(3)	Cu1-N2	1.968(2)
Cu1-N4	1.955(2)	Cu1-N5	1.958(3)
N1-C1	1.348(4)	N1-C8	1.403(3)
N2-C9	1.399(4)	N2-C16	1.347(4)
N3-C8	1.323(3)	N3-C9	1.322(4)
N4-C29	1.355(5)	N4-C36	1.393(4)
N5-C37	1.392(3)	N5-C44	1.349(5)
N6-C36	1.325(5)	N6-C37	1.333(5)
C1-C2	1.439(4)	C1-C17	1.470(4)
C2-C3	1.409(4)	C2-C7	1.411(4)
C3-C4	1.380(5)	C4-C5	1.406(4)
C5-C6	1.379(5)	C6-C7	1.400(4)
C7-C8	1.443(4)	C9-C10	1.442(4)
C10-C11	1.395(4)	C10-C15	1.416(5)
C11-C12	1.378(4)	C12-C13	1.407(5)
C13-C14	1.377(4)	C14-C15	1.401(4)
C15-C16	1.431(4)	C16-C23	1.470(4)
C17-C18	1.399(6)	C17-C22	1.403(5)
C18-C19	1.386(4)	C19-C20	1.381(7)
C20-C21	1.379(7)	C21-C22	1.381(4)
C23-C24	1.392(4)	C23-C28	1.402(6)
C24-C25	1.386(5)	C25-C26	1.373(8)
C26-C27	1.385(5)	C27-C28	1.386(6)
C29-C30	1.437(4)	C29-C45	1.466(5)
C30-C31	1.402(6)	C30-C35	1.415(6)

C31-C32	1.372(4)	C32-C33	1.395(7)
C33-C34	1.380(7)	C34-C35	1.394(4)
C35-C36	1.444(5)	C37-C38	1.447(6)
C38-C39	1.400(5)	C38-C43	1.420(4)
C39-C40	1.381(7)	C40-C41	1.395(5)
C41-C42	1.374(5)	C42-C43	1.399(6)
C43-C44	1.439(5)	C44-C51	1.461(4)
C45-C46	1.395(4)	C45-C50	1.402(6)
C46-C47	1.384(5)	C47-C48	1.373(7)
C48-C49	1.382(5)	C49-C50	1.382(6)
C51-C52	1.401(5)	C51-C56	1.392(5)
C52-C53	1.379(5)	C53-C54	1.387(6)
C54-C55	1.383(6)	C55-C56	1.383(4)

Table 4-3. Bond angles for **3**.

N1-Cu1-N2	94.48(9)	N1-Cu1-N4	104.74(11)
N1-Cu1-N5	133.29(11)	N2-Cu1-N4	133.28(10)
N2-Cu1-N5	104.30(12)	N4-Cu1-N5	92.81(12)
Cu1-N1-C1	129.77(19)	Cu1-N1-C8	121.84(18)
C1-N1-C8	108.3(2)	Cu1-N2-C9	121.98(18)
Cu1-N2-C16	129.76(19)	C9-N2-C16	108.2(2)
C8-N3-C9	126.2(2)	Cu1-N4-C29	127.3(2)
Cu1-N4-C36	124.0(3)	C29-N4-C36	108.2(2)
Cu1-N5-C37	123.4(3)	Cu1-N5-C44	126.76(19)
C37-N5-C44	109.1(3)	C36-N6-C37	125.8(3)

N1-C1-C2	110.3(2)	N1-C1-C17	123.6(3)
C2-C1-C17	126.1(3)	C1-C2-C3	132.4(3)
C1-C2-C7	106.5(3)	C3-C2-C7	121.0(3)
C2-C3-C4	117.4(3)	C3-C4-C5	121.2(3)
C4-C5-C6	122.0(3)	C5-C6-C7	117.5(3)
C2-C7-C6	120.8(3)	C2-C7-C8	106.5(2)
C6-C7-C8	132.6(3)	N1-C8-N3	127.8(3)
N1-C8-C7	108.4(2)	N3-C8-C7	123.8(2)
N2-C9-N3	127.6(2)	N2-C9-C10	108.4(2)
N3-C9-C10	124.0(3)	C9-C10-C11	133.0(3)
C9-C10-C15	106.4(2)	C11-C10-C15	120.6(3)
C10-C11-C12	118.4(3)	C11-C12-C13	121.4(3)
C12-C13-C14	120.8(3)	C13-C14-C15	118.7(3)
C10-C15-C14	120.1(3)	C10-C15-C16	106.3(2)
C14-C15-C16	133.5(3)	N2-C16-C15	110.6(3)
N2-C16-C23	123.5(2)	C15-C16-C23	125.8(3)
C1-C17-C18	122.0(3)	C1-C17-C22	119.6(4)
C18-C17-C22	118.4(3)	C17-C18-C19	120.0(4)
C18-C19-C20	120.7(4)	C19-20-21	119.9(3)
C20-C21-C22	120.0(4)	C17-C22-C21	120.9(4)
C16-C23-C24	122.6(4)	C16-C23-C28	119.2(3)
C24-C23-C28	118.1(3)	C23-C24-C25	121.0(4)
C24-C25-C28	119.9(3)	C25-C26-C27	120.5(4)
C26-C27-C28	119.7(5)	C23-C28-C27	120.7(3)
N4-C29-C30	110.5(3)	N4-C29-C45	122.1(2)
C30-C29-C45	127.5(4)	C29-C30-C31	133.0(4)

C29-C30-C35	106.1(3)	C31-C30-C35	120.8(3)
C30-C31-C32	118.0(4)	C31-C32-C33	121.5(4)
C32-C33-C34	121.2(3)	C33-C34-C35	118.7(4)
C30-C35-C34	119.8(4)	C30-C35-C36	106.7(3)
C34-C35-C36	133.6(4)	N4-C36-N6	126.4(3)
N4-C36-C35	108.6(3)	N6-C36-C35	125.1(3)
N5-C37-N6	126.7(4)	N5-C37-C38	108.2(3)
N6-C37-C38	125.1(3)	C37-C38-C39	133.2(3)
C37-C38-C43	106.4(3)	C39-C38-C43	120.4(4)
C38-C39-C40	117.8(3)	C39-C40-C41	121.7(4)
C40-C41-C42	121.4(5)	C41-C42-C43	118.2(3)
C38-C43-C42	120.5(3)	C38-C43-C44	106.3(3)
C42-C43-C44	133.2(3)	N5-C44-C43	110.0(2)
N5-C44-C51	122.8(3)	C43-C44-C51	127.2(4)
C29-C45-C46	121.3(3)	C29-C45-C50	120.1(3)
C46-C45-C50	118.6(3)	C45-C46-C47	120.9(4)
C46-C47-C48	119.7(3)	C47-C48-C49	120.4(4)
C48-C49-C50	120.4(5)	C45-C50-C49	119.9(3)
C44-C51-C52	120.0(3)	C44-C51-C56	121.2(3)
C52-C51-C56	118.8(3)	C51-C52-C53	120.3(4)
C52-C53-C54	120.3(4)	C53-C54-C55	119.9(3)
C54-C55-C56	120.2(4)	C51-C56-C55	120.5(3)

4-4-2 Static magnetic properties

Magnetic susceptibility measurements were performed on a powder form of **3**. The $\chi_M T$ vs. T

plot was depicted in Figure 4-5. The $\chi_M T$ value is almost plateau between 15 - 200 K (0.378 cm^3

mol^{-1} at 200 K), which is consistent with $S = 1/2$ spin-only value. Magnetization (M) vs. static field

($\mu_0 H$) plot shows no hysteresis loops even at 1.8 K (Figure 4-6 (a)). The plotted M vs. $\mu_0 H T^{-1}$

curves are superimposed (Figure 4-6 (b)), which indicates that **3** has no significant magnetic

anisotropy. It is consistent with no existence of zero-field splittings in $S = 1/2$ systems.
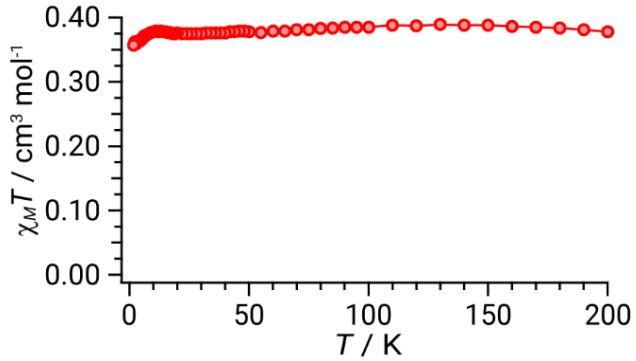
**Figure 4-5.** $\chi_M T$ vs. T plot of **3** measured in an applied static field of 1000 Oe.
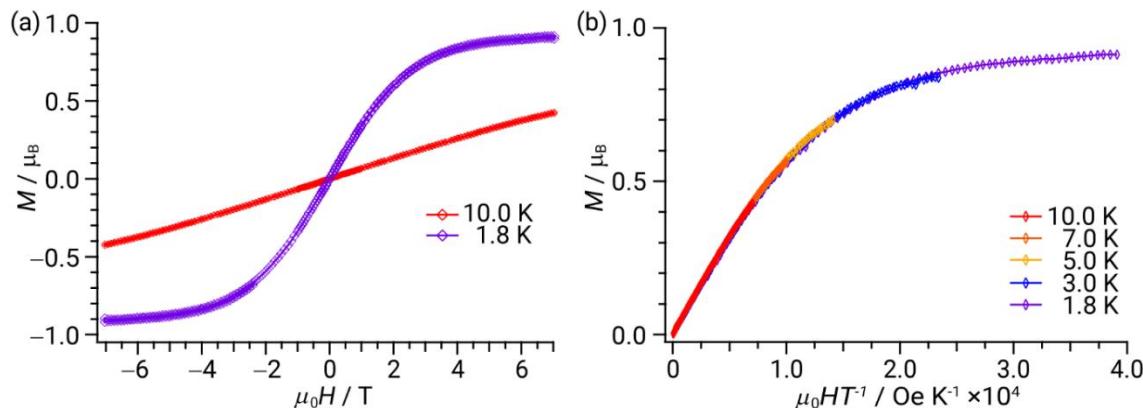
Figure 4-6. (a) Magnetization (M) vs. magnetic field ($\mu_0 H$) and (b) Magnetization (M) vs. $\mu_0 H / T$

plot of **3**.

4-4-3. X-band electron spin resonance (ESR) measurements

In order to confirm the electronic structure of **3**, the X-band electron spin resonance (ESR) spectra (9.211 GHz) were measured on 3.7 % magnetically diluted **3** [$Cu_{0.037}Zn_{0.963}$(half-Pc$_{Ph}$)$_2$] (**dil.3**) at (123 K, Figure 4-7). The splitting into four peaks at low magnetic field is successfully simulated by considering the interaction between the electron and nuclear spins (hyperfine interaction) of the Cu(II) ($S = 1/2$, $I = 3/2$). This indicates the spin is largely located on the central Cu(II) ions. The entire spectrum was successfully reproduced by the following parameters: $g_{//} = 2.26$, $g_{\perp} = 2.07$, $A_{//}$(Cu) = 11.0 mT (154 MHz), $A_{\perp}$(Cu) = 1.5 mT (21 MHz). The average g value $g_{av} = (g_{//} + 2g_{\perp})$ / 3 = 2.13 or $g_{av} = \sqrt{(g_{//}^2 + 2g_{\perp}^2)/3} = 2.14$ is slightly larger than that of magnetic susceptibility measurements at 120 K ($g_{iso} = 2.03$).
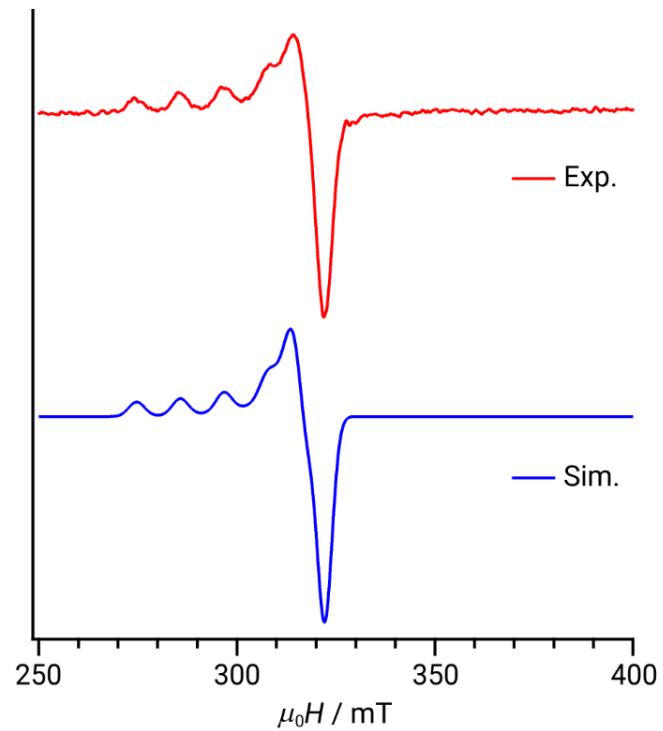
Figure 4-7. (red) X-band ESR spectrum of **dil.3** at 123 K and (blue) simulation curve with the following parameters: $g_{//} = 2.26$, $g_{\perp} = 2.07$, $A_{//} = 11.0$ mT (154 MHz), $A_{\perp} = 1.5$ mT (21 MHz)

4-4-4. Dynamic magnetic properties

In order to investigate the dynamic magnetic relaxations, alternative current (ac) magnetic susceptibility measurements of **3** were performed at 1.8 K. In the absence of applied static field, no χ'' signals were observed (Figure 4-8). Applying a static field of 2000 Oe, a peak maximum of χ'' is observed in ac frequency ca. 200 Hz. The peak slightly shifts to lower frequency when the applied static magnetic field is increased to 5000 Oe, and the peak become apparently broad in a static field of 10000 Oe. The Cole-Cole plots showed single semi-circles for each condition (Figure 4-9), therefore, the generalized Debye model with single relaxation time was employed to these peaks in order to extract relaxation times. Fitting parameters were listed in Table 4-4. The obtained dispersion coefficients α are increased with increasing the magnitude of applied static field, which indicates that the dispersion of relaxation times become complicated with increasing static field.

Variable-temperature ac measurements in a static magnetic field of 2000 Oe and 5000 Oe were performed. The peak was shifted to higher frequency with increasing temperatures (Figure 4-10(a, b)). Above 3.0 K, only the shoulder of χ'' were observed. Prepared Cole-Cole plots were fitted by employing the generalized Debye model, in order to investigate the relaxation times (Figure 4-11, Table 4-5 and 4-6). It should be noted that the dispersion coefficients α are relatively large even at 7.5 K (ca. 0.4), which indicate that large dispersion of relaxation time even at high temperatures in undiluted **3**.
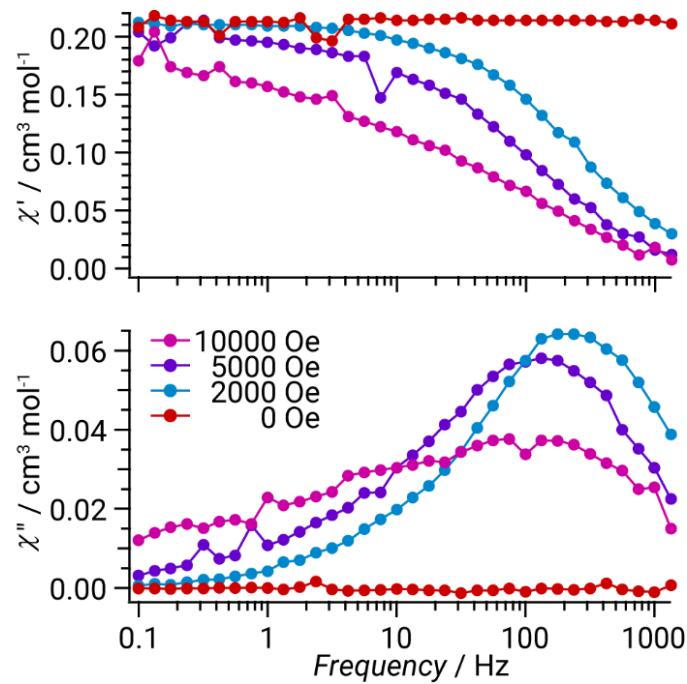
Figure 4-8. Frequency dependence of χ' and χ'' measured in indicated static magnetic field at 1.8 K of **3**.
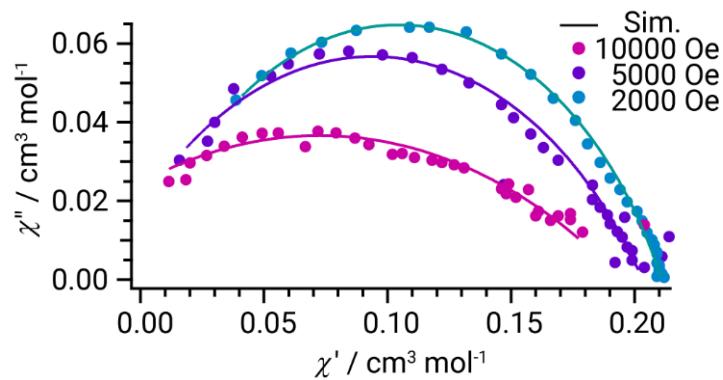

Figure 4-9. Cole-Cole plot at 1.8 K of **3**.

Table 4-4. Fitting parameters in a static magnetic field at 1.8 K of **3**.

| H / Oe	χ_t / cm^3 mol^{-1}	χ_s / cm^3 mol^{-1}	α	τ / s
2000	0.21	−0.0021	0.30	6.88×10^{-4}
5000	0.20	−0.015	0.39	1.49×10^{-3}
10000	0.20	−0.05	0.63	2.40×10^{-3}
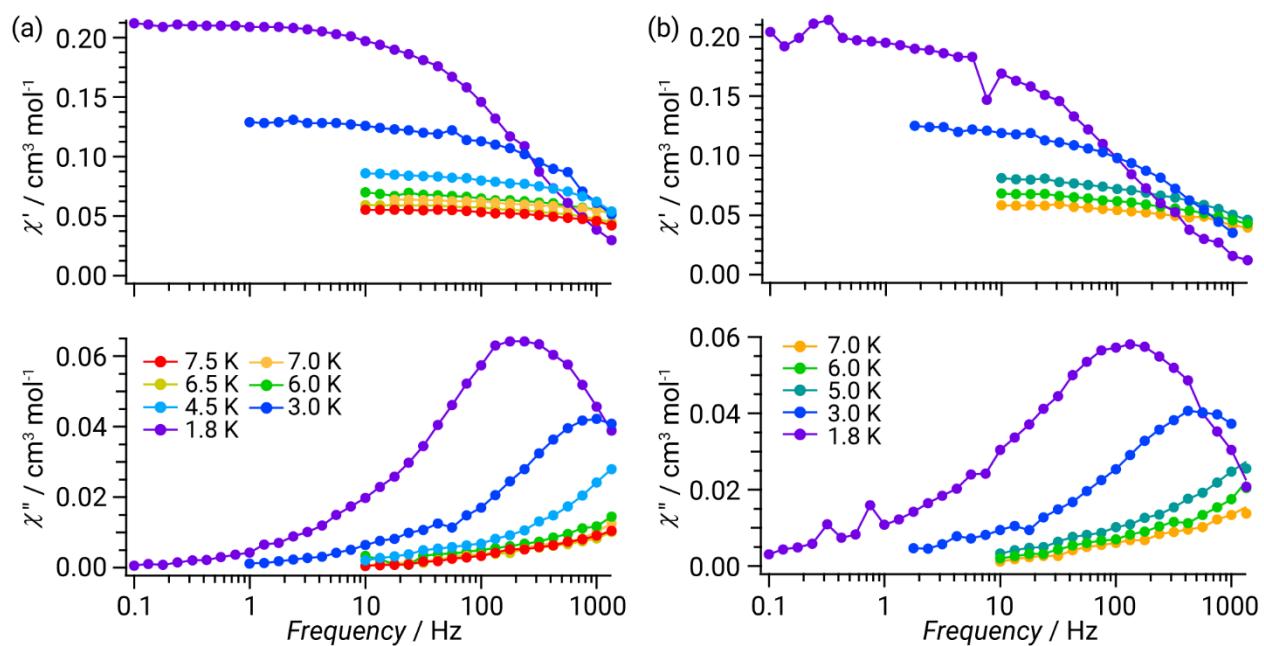
Figure 4-10. Frequency dependence of χ' and χ'' plot in a static magnetic field of (a) 2000 Oe and (b) 5000 Oe of **3**.
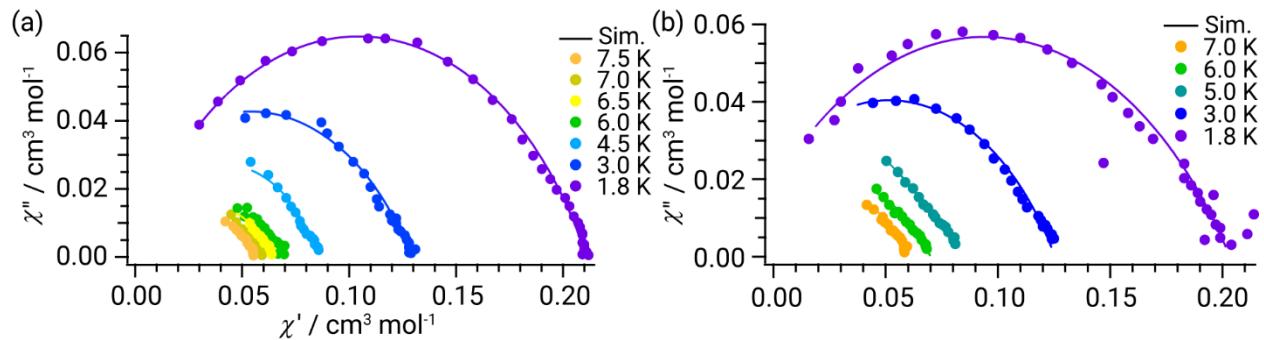
Figure 4-11. Cole-Cole plots in an applied static magnetic field of (a) 2000 and (b) 5000 Oe of **3**.

Table 4-5. Fitting parameters in a static magnetic field of 2000 Oe of **3**.

T / K	χ_t / cm^3 mol^{-1}	χ_s / cm^3 mol^{-1}	α	τ / s
7.5	0.056	0.015	0.36	4.59×10^{-5}
7.0	0.060	0.080	0.40	3.45×10^{-5}
6.5	0.064	0.0067	0.40	3.39×10^{-5}
6.0	0.070	0.016	0.39	4.86×10^{-5}
4.5	0.086	−0.017	0.34	4.30×10^{-5}
3.0	0.13	−0.022	0.34	1.17×10^{-4}
1.8	0.21	−0.0021	0.30	6.88×10^{-4}

Table 4-6. Fitting parameters in a static magnetic field of 5000 Oe of **3**.

T / K	χ_t / cm³ mol⁻¹	χ_s / cm³ mol⁻¹	α	τ / s
7.0	0.06	0.001	0.39	5.5×10^{-5}
6.0	0.07	0.015	0.45	4.0×10^{-5}
5.0	0.82	−0.01	0.37	7.0×10^{-5}
3.0	0.13	−0.022	0.36	2.25×10^{-4}
1.8	0.20	−0.015	0.39	1.49×10^{-3}

In order to reduce the intermolecular interactions and get deeper insight of relaxation mechanism of **3**, 3.7 % magnetically diluted **3** [$Cu_{0.037}Zn_{0.963}$(half-Pc_{Ph})$_2$] (**dil.3**) was prepared and investigated. In a static field of 2000 Oe, a peak maximum in χ'' was observed ca. 10 Hz at 1.8 K (Figure 4-12), which is largely shifted to lower frequency compared with undiluted **3** (ca. 200 Hz for **3**), which indicated the magnetic relaxation on **3** molecules are largely influenced by intermolecular interactions. On increasing temperatures, the χ'' maxima gradually shift to higher frequency, and the peaks were reached 200 Hz at 14.0 K. Fitting parameters were listed on Table 4-7. The dispersion coefficient α at 1.8 K (0.22) become smaller and relaxation time τ (8.08×10^{-2} s) is two order larger than that of undiluted **3** ($\alpha = 0.30$ and $\tau = 6.88 \times 10^{-4}$ s, respectively). The relaxation time τ increased and dispersion coefficient α decreased monotonically with increasing temperature, which is typical tendency found in other systems.
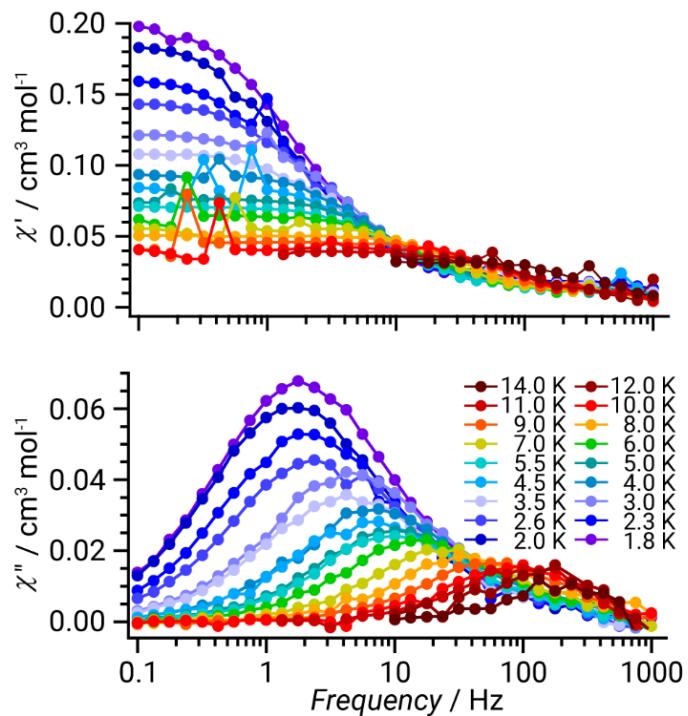
Figure 4-12. Frequency dependence of χ' and χ'' plot for **dil.3** measured in an applied static magnetic field of 2000 Oe.
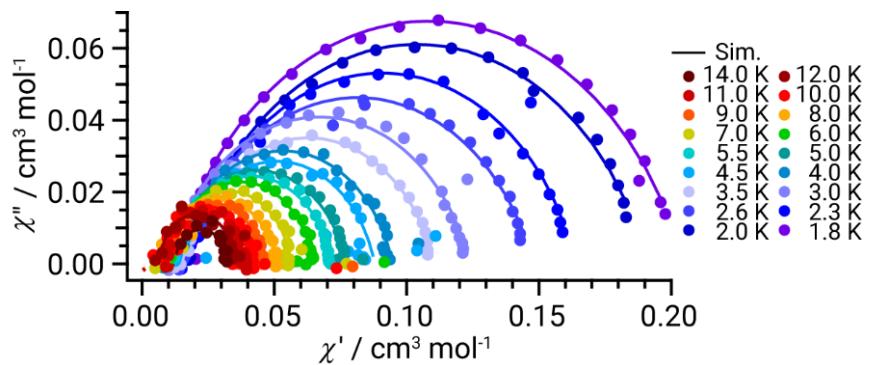

Figure 4-13. Cole-Cole plot of χ' and χ'' plot for **dil.3** measured in an applied static magnetic field of 2000 Oe.

Table 4-7. Fitting parameters of $[Cu_{0.037}Zn_{0.963}(half\text{-}Pc_{Ph})_2]$ (**dil.3**) in static field of 2000 Oe.

T / K	χ_t / cm^3 mol^{-1}	χ_s / cm^3 mol^{-1}	α	τ / s
14.0	0.032	0.013	0.0065	7.17×10^{-4}
12.0	0.035	0.0068	0.016	1.29×10^{-3}
11.0	0.038	0.0085	0.012	1.69×10^{-3}
10.0	0.041	0.0085	0.0092	1.88×10^{-3}
9.0	0.045	0.0082	0.058	2.79×10^{-3}
8.0	0.051	0.0084	0.11	4.10×10^{-3}
7.0	0.056	0.0090	0.099	6.35×10^{-3}
6.0	0.065	0.0097	0.12	9.80×10^{-3}
5.5	0.071	0.012	0.13	1.52×10^{-2}
5.0	0.077	0.0096	0.16	1.36×10^{-2}
4.5	0.086	0.014	0.16	2.21×10^{-2}
4.0	0.095	0.012	0.17	2.06×10^{-2}
3.5	0.11	0.014	0.20	3.42×10^{-2}
3.0	0.12	0.010	0.21	3.09×10^{-2}
2.6	0.15	0.015	0.22	5.56×10^{-2}
2.3	0.16	0.016	0.22	6.96×10^{-2}
2.0	0.19	0.017	0.22	9.07×10^{-2}
1.8	0.20	0.012	0.22	8.08×10^{-2}

In order to get information about the static field dependence of relaxation behavior of **dil.3**, ac measurements at 1.8 K were performed in various static magnetic field conditions (Figure 4-14). As shown above, χ'' signals were not observed in no applied static magnetic field. On increasing a static field, χ'' signals were slightly increased with increasing ac frequency, and a small peak of χ'' was observed at ac frequency of ca. 10 Hz under an applying static field of 100 Oe. Increasing static field above 100 Oe, the peaks gradually increase and shift to the lower frequency. In a static field of 5000 Oe, the peak maximum was reached to ca. 1 Hz. Further increasing static field gradually shifted the peaks to the higher frequencies and the peaks reached ca. 20 Hz in a static field of 20000 Oe. The Cole-Cole plots showed clear semi-circles in an applied static field above 50 Oe, and these plots were fitted by generalize Debye model with one relaxation components (Figure 4-15, Table 4-5). Obtained relaxation time τ was increased with static magnetic field of up to 5000 Oe, then it decreased with further increasing static field. The former is attributed to the decrease of QTM process and the latter is dominant direct process as observed in **2**. However, the static field dependence of relaxation times was small compared with **2**. Similar behaviors are reported in $S = 1/2$ V(IV) mononuclear systems.[7-11]
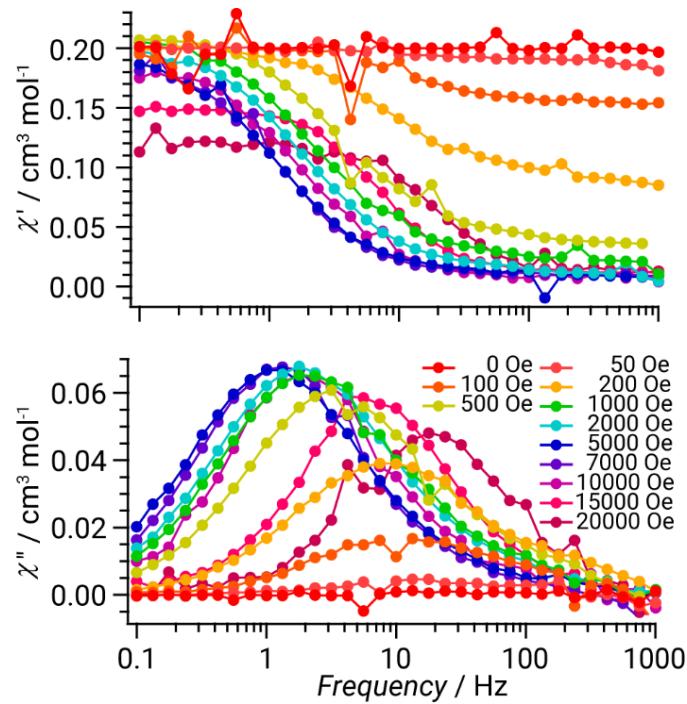
Figure 4-14. Frequency dependence of χ' and χ'' plot for **dil.3** at 1.8 K in an absence of static magnetic field and applied static field between 50 – 20000 Oe.
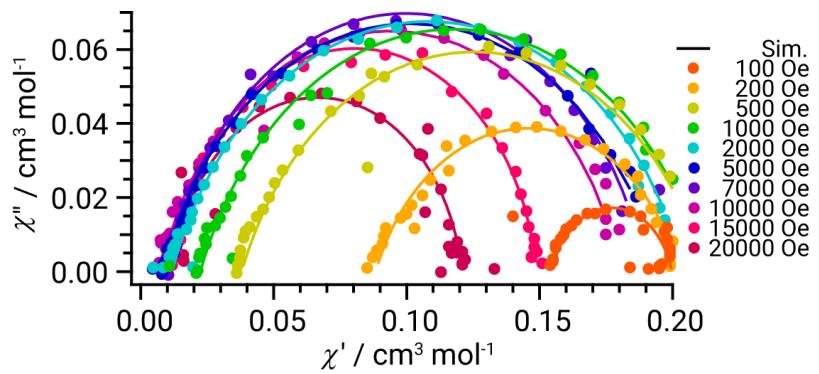

Figure 4-15. Cole-Cole plot and the simulation curves of **dil.3** measured in various static magnetic field between 100 – 20000 Oe at 1.8 K.

Table 4-8. Fitting parameters of $[Cu_{0.037}Zn_{0.963}(half\text{-}Pc_{Ph})_2]$ at 1.8 K.

H / Oe	χ_t / cm^3 mol^{-1}	χ_s / cm^3 mol^{-1}	α	τ / s
100	0.20	0.15	0.17	1.23×10^{-2}
200	0.20	0.088	0.24	1.77×10^{-2}
500	0.21	0.038	0.24	4.49×10^{-2}
1000	0.21	0.022	0.23	6.99×10^{-2}
2000	0.20	0.012	0.22	8.08×10^{-2}
3000	0.20	0.010	0.22	1.15×10^{-1}
5000	0.19	0.0084	0.21	1.34×10^{-1}
7000	0.19	0.010	0.16	1.24×10^{-1}
10000	0.18	0.0077	0.18	8.25×10^{-2}
15000	0.15	0.012	0.086	2.24×10^{-2}
20000	0.12	0.014	0.076	8.74×10^{-3}

Extracted temperature- and static magnetic field-dependence of relaxation times τ were simultaneously fitted by expected relaxation mechanisms, in order to rationalize the relaxation mechanisms. As mentioned above, Orbach process is not expected owing to the lack of accessible excited state to flip the magnetization. Therefore, relaxation mechanism of **3** was fitted by following equation considering spin-lattice direct and Raman processes and tunneling process (Figure 4-16).[25,26]

$$\tau^{-1} = AH^5 \coth(g\mu_{\mathrm{B}}H/2k_{\mathrm{B}}T) + CT^n + d\frac{1+eH^2}{1+fH^2}$$

The best fit was obtained by following parameters: $A = 2.5$ s^{-1} T^{-5}, $C = 0.50$ s^{-1} K^{-n}, $n = 3.0$, $d = 85$ s^{-1}, $e = 50$ T^{-2}, $f = 1.5 \times 10^3$ T^{-2}. It is noted that the finite intermolecular contribution on magnetic relaxations e is essential to obtain good fit in the field dependence of relaxation time, which is in contrast to [Co(L)$_2$] (**2**) case discussed in Chapter 2 of this thesis. The obtained Raman coefficient n of 3.0 is much smaller than theoretical value of 9. However, this value is observed in other $S = 1/2$ systems and allowed in existence of acoustic and optical phonons.[27]
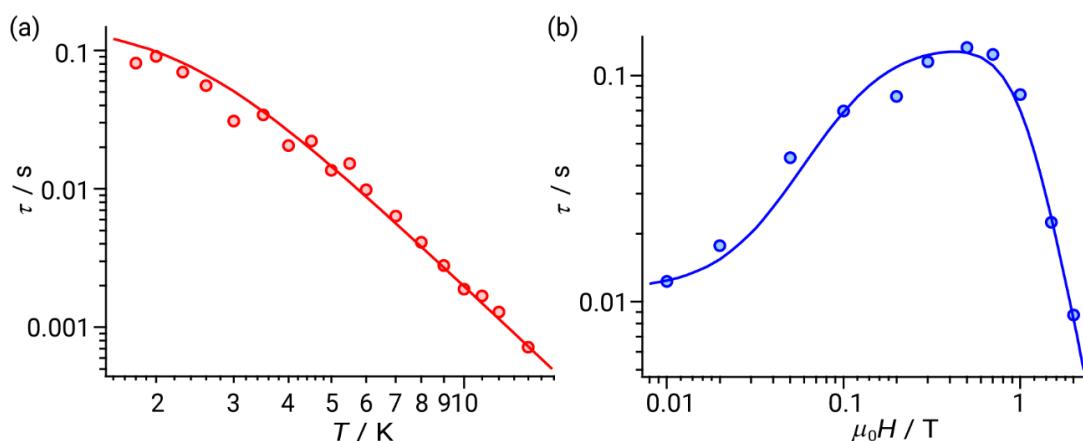

Figure 4-16. (a) Temperature- and (b) static field-dependence relaxation time plots of **dil.3** and fitting curves. Fitting parameters are given in the text.

4-5 Conclusions

Slow magnetic relaxation of a distorted tetrahedral four-coordinate mononuclear copper(II) complex [Cu(II)(half-Pc$_{Ph}$)$_2$] (**3**) composed of two bis-pheyl-bisisoindole-aza-methene bidentate ligands (half-Pc$_{Ph}$) has been reported. The X-ray analysis revealed the highly distorted tetrahedral four-coordination geometry of **3**. Static magnetic susceptibility measurements showed almost identical $\chi_M T$ value with spin-only $S = 1/2$ value in the entire temperature range, and no dispersion in magnetization vs. $\mu_0 H T^{-1}$ plot indicated no significant magnetic anisotropy on **3**. X-band electron spin resonance (ESR) measurements on 3.7 % magnetically diluted **3** [Cu$_{0.037}$Zn$_{0.963}$(half-Pc$_{Ph}$)$_2$] (**dil.3**) at 123 K indicated that the unpaired electron is mainly located in the central Cu(II) ions. Ac susceptibility measurements of **3** exhibited slow magnetic relaxation in applied static magnetic field. On diluting with diamagnetic isomorphous, slow magnetic relaxations of **dil.3** were largely enhanced and the χ'' peak maxima were observed even at 14.0 K in an applied static magnetic field of 2000 Oe. At 1.8 K, the χ'' peak gradually shifted to lower frequency applying a static field up to 5000 Oe. Above 5000 Oe, the maxima shifted to higher frequency and observed even in a static field of 20000 Oe. The extracted temperature and static field dependencies of relaxation times were successfully reproduced by assuming the direct, Raman and QTM processes. The Raman coefficient $n = 3.0$ indicated the relaxation process is molecular origin and the finite e parameter of QTM term implied that the retention of relaxation times at 1.8 K between 1000 – 10000 Oe derives from the intermolecular interactions among the Cu(II) spin centers.

4-6 References

1. Gatteschi, D.; Sessoli, R. Quantum Tunneling of Magnetization and Related Phenomena in Molecular Materials. *Angew. Chem. Int. Ed.* **2003**, *42*, 268-297.

2. Feltham, H. L. C.; Brooker, S. Review of purely 4f and mixed-metal nd-4f single-molecule magnets containing only one lanthanide ion. *Coord. Chem. Rev.* **2014**, *276*, 1−33.

3. Frost, J. M.; Harriman, K. L. M.; Murugesu, M. The rise of 3-d single-ion magnets in molecular magnetism: towards materials from molecules?. *Chem. Sci.* **2016**, *7*, 2470–2491.

4. Zadrozny, J. M.; Liu, J.; Piro, N. A.; Chang, C. J.; Hill, S.; Long, J. R. Slow magnetic relaxation in a pseudotetrahedral cobalt(II) complex with easy-plane anisotropy. *Chem. Commun.* **2012**, *48*, 3897-3900.

5. Vallejo, J.; Castro, I.; Ruiz-García, R.; Cano, J.; Julve, M.; Lloret, F.; Munno, G. D.; Wernsdorfer, W.; Pardo, E. Field-Induced Slow Magnetic Relaxation in a Six-Coordinate Mononuclear Cobalt(II) Complex with a Positive Anisotropy. *J. Am. Chem. Soc.* **2012**, *134*, 15704−15707.

6. Colacio, E.; Ruiz, J.; Ruiz, E.; Cremades, E.; Krzystek, J.; Carretta, S.; Cano, J.; Guidi, T.; Wernsdorfer, W.; Brechin, E. K. Slow Magnetic Relaxation in a $Co^{II}–Y^{III}$ Single-Ion Magnet with Positive Axial Zero-Field Splitting. *Angew. Chem. Int. Ed.* **2013**, *52*, 9130 –9134.

7. Gómez-Coca, S.; Urtizberea, A.; Cremades, E.; Alonso, P. J.; Camón, A.; Ruiz, E.; Luis, F. Origin of slow magnetic relaxation in Kramers ions with non-uniaxial anisotropy. *Nat. Commun.* **2014**, *5*, 4300.

8. L. Tesi, E. Lucaccini, I. Cimatti, M. Perfetti, M. Mannini, M. Atzori, E. Morra, M. Chiesa, A. Caneschi, L. Sorace, R. Sessoli. Quantum coherence in a processable vanadyl complex: new tools for the search of molecular spin qubits. *Chem. Sci.* **2016**, *7*, 2074–2083.

9. M. Atzori, L. Tesi, E. Morra, M. Chiesa, L. Sorace, R. Sessoli. Room-Temperature Quantum Coherence and Rabi Oscillations in Vanadyl Phthalocyanine: Toward Multifunctional Molecular Spin Qubits. *J. Am. Chem. Soc.* **2016**, *138*, 2154−2157.

10. L. Tesi, A. Lunghi, M. Atzori, E. Lucaccini, L. Sorace, F. Tottia, R. Sessoli. Giant spin–phonon bottleneck effects in evaporable vanadyl-based molecules with long spin coherence. *Dalton Trans.* **2016**, *45*, 16635–16643.

11. M. Atzori, L. Tesi, S. Benci, A. Lunghi, R. Righini, A. Taschin, R. Torre, L. Sorace, R. Sessoli. Spin Dynamics and Low Energy Vibrations: Insights from Vanadyl-Based Potential Molecular Qubits. *J. Am. Chem. Soc.* **2017**, *139*, 4338−4341.

12. M. S. Fataftah, M. D. Krzyaniak, B. Vlaisavljevich, M. R. Wasielewski, J. M. Zadrozny, D. E. Freedman. Metal–ligand covalency enables room temperature molecular qubit candidates. *Chem. Sci.* **2019,** *10*, 6707–6714.

13. M. Ding, G. E. Cutsail III, D. Aravena, M. Amoza, M. Rouzières, P. Dechambenoit, Y. Losovyj, M. Pink, E. Ruiz, R. Clérac, J. M. Smith. A low spin manganese(IV) nitride single molecule magnet. *Chem. Sci.* **2016**, *7*, 6132–6140.

14. H.-H. Cui, J. Wang. X.-T. Chen, Z.-L. Xue. Slow magnetic relaxation in five-coordinate spin-crossover cobalt(II) complexes. *Chem. Commun.* **2017**, *53*, 9304-9307.

15. R. C. Poulten, M. J. Page, A. G. Algarra, J. J. L. Roy, I López,   E. Carter, A. Llobet, S. A. Macgregor, M. F. Mahon, D. M. Murphy, M. Murugesu, M. K. Whittlesey. Synthesis, Electronic Structure, and Magnetism of [Ni(6-Mes)$_2$]$^+$: A Two-Coordinate Nickel(I) Complex Stabilized by Bulky N‑Heterocyclic Carbenes. *J. Am. Chem. Soc.* **2013**, *135*, 13640−13643.

16. W. Lin, T. Bodenstein, V. Mereacre, K. Fink, A. Eichhöfer. Field-Induced Slow Magnetic Relaxation in the Ni(I) Complexes [NiCl(PPh$_3$)$_2$]·C$_4$H$_8$O and [Ni(N(SiMe$_3$)$_2$)(PPh$_3$)$_2$]. *Inorg. Chem.* **2016**, *55*, 2091−2100.

17. I. Bhowmick, A. J. Roehl, J. R. Neilson, A. K. Rappé. M. P. Shores. Slow magnetic relaxation in octahedral low-spin Ni(III) complexes. *Chem. Sci.* **2018**, *9*, 6564–6571.

18. R. Boča, C. Rajnák, J. Titiš, D. Valigura, Field Supported Slow Magnetic Relaxation in a Mononuclear Cu(II) Complex. *Inorg. Chem.* **2017**, *56*, 1478−1482.

19. Fataftah, M. S.; Krzyaniak M. D.; Vlaisavljevich, B.; Wasielewski, M. R.; Zadrozny J. M.; Freedman, D. E. Metal–ligand covalency enables room temperature molecular qubit candidates. *Chem. Sci.* **2019**, *10*, 6707–6714.

20. S.-Q. Wu, Y. Miyazaki, M. Nakano, S.-Q. Su, Z.-S. Yao, H.-Z. Kou, O. Sato. Slow Magnetic Relaxation in a Mononuclear Ruthenium(III) Complex. *Chem. Eur. J.* **2017**, *23*, 10028 – 10033.

21. E. Maligaspe, T. J. Pundsack, L. M. Albert, Y. V. Zatsikha, P. V. Solntsev, D. A. Blank, V. N. Nemykin. Synthesis and Charge-Transfer Dynamics in a Ferrocene-Containing Organoboryl aza-BODIPY Donor−Acceptor Triad with Boron as the Hub. *Inorg. Chem.* **2015**, *54*, 4167−4174.

22. Gresser, R.; Hoyer, A.; Hummert, M.; Hartmann, H.; Leo, K.; Riede, M. Homoleptic Co(II), Ni(II), Cu(II), Zn(II) and Hg(II) complexes of bis-(phenyl)-diisoindol-aza-methene. *Dalton Trans.* **2011**, *40*, 3476–3483.

23. Bain, G. A.; Berry, J. F. Diamagnetic Corrections and Pascal's Constants. *J. Chem. Educ.* **2008**, *85*, 532−536.

24. Sheldrick, G. M. *A short history of SHELX. Acta Crystallogr., Sect. A: Found. Crystallogr.* **2008**, *64*, 112−122.

25. Fort, A.; Rettori, A.; Villain, J.; Gatteschi, D.; Sessoli. R.; Mixed Quantum-Thermal Relaxation in Mn12 Acetate Molecules. *Phys. Rev. Lett.* 1998, 80, 612-615.

26. Vleck, J. H. V. Paramagnetic Relaxation Times for Titanium and Chrome Alum. *Phys. Rev.* **1940**, *57*, 426-447.

27. Shriyastava, K. N. Theory of Spin-Lattice Relaxation. *Phys. Status Solidi B* **1983**, *117*, 437–458.

Chapter 5

Summary

5-1 Summary

This thesis is dedicated to the observation of recently reported mononuclear first-row transition metal based slow magnetic relaxation phenomena. In this dissertation, two $S = 3/2$ Co(II) complexes and one $S = 1/2$ Cu(II) complex composed of rigid bidentate ligands with tetrahedral four-coordinate ligand field were investigated. In order to discuss the molecular based magnetic relaxations, measurements on magnetically dilution measurements were performed.

In chapter 2, the synthesis and magnetic properties of a tetrahedral four-coordinate mononuclear Co(II) complex comprised of bisisoindole-aza-methene ligands [Co(half-Pc)$_2$] (**1**) were reported. The complex exhibited the slow magnetic relaxation even in no applied static magnetic field. The easy-axis type of magnetic anisotropy and the large zero-field splitting between the ground $M_S = \pm 3/2$ and the first excited $M_S = \pm 1/2$ states is unambiguously determined by the high-field, multi-frequency electron spin resonance (ESR) measurements and Orbach magnetic relaxation at high temperature was successfully determined.

In chapter 3, the effect of intermolecular interactions on dynamic magnetic relaxations of a tetrahedral four-coordinate mononuclear Co(II) complex comprised of bidentate ligands synthesized through the dehydration reactions of pyrrolopyrrole and benzothiazole moieties [Co(L)$_2$] (**2**) was reported. The comparison between undiluted **2** and magnetically diluted **2** indicated that the large dispersion indicated on undiluted **2** were mainly intermolecular origin. In addition, extracted relaxation times which investigated entire temperature and static field were fitted by the Orbach, Raman, direct and quantum tunneling processes.

In chapter 4, slow magnetic relaxation on an $S = 1/2$ distorted tetrahedral coordinate Cu(II) mononuclear complex with bis-pheyl-bisisoindole-aza-methene ligands [Cu(half-Pc$_{Ph}$)$_2$] (**3**) was

reported. The complex exhibited slow magnetic relaxations only in a static magnetic field, and the dilution measurements showed that the slow relaxations were largely enhanced by reducing the intermolecular interactions. Extracted temperature- and field- dependencies of relaxation times were successfully reproduced by the direct, Raman and tunneling processes. The obtained Raman coefficient n larger than 2 implies the relaxation is the molecular origin and not induced by the bottleneck of exchanging energy between spin systems and lattice (phonon-bottleneck processes). However, the influence of intermolecular interactions was indicated by QTM coefficient.

In conclusion, the dynamic magnetic relaxations called slow magnetic relaxations of the series of mononuclear transition metal complexes with rigid bidentate ligand were successfully observed and the mechanisms were discussed. The consistency between the zero-field splitting and the relaxation energy barriers observed for **1** indicates that these rigid structures may be good candidates for the observation of slow magnetic relaxations at higher temperatures.

Appendix
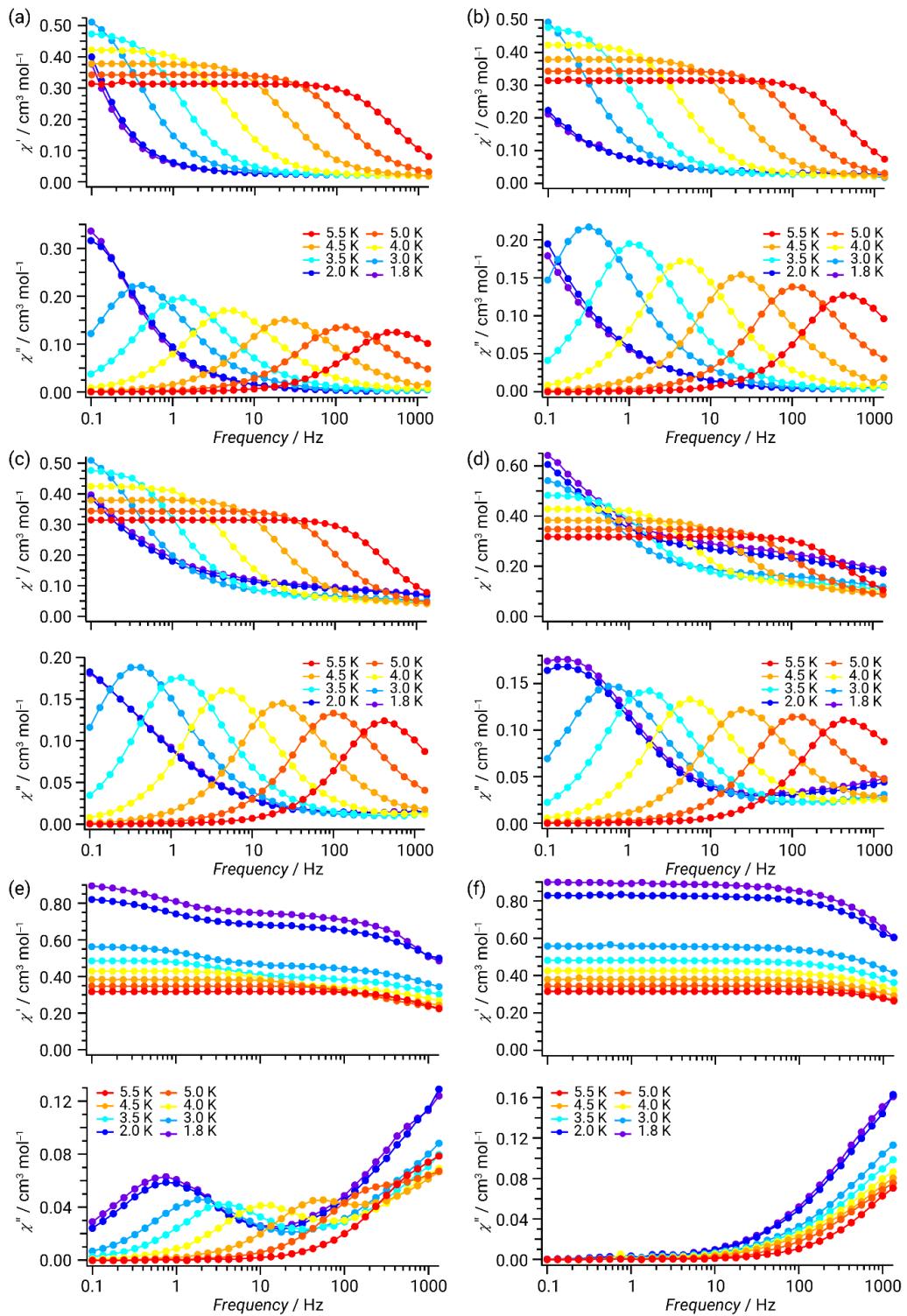
Figure S1. Plots of χ' (top) and χ'' (bottom) against applied ac frequency of **1** at H_{dc} of (a) 2000, (b) 1000, (c) 500, (d) 300, (e) 100, and (f) 0 Oe at the indicated temperatures

128
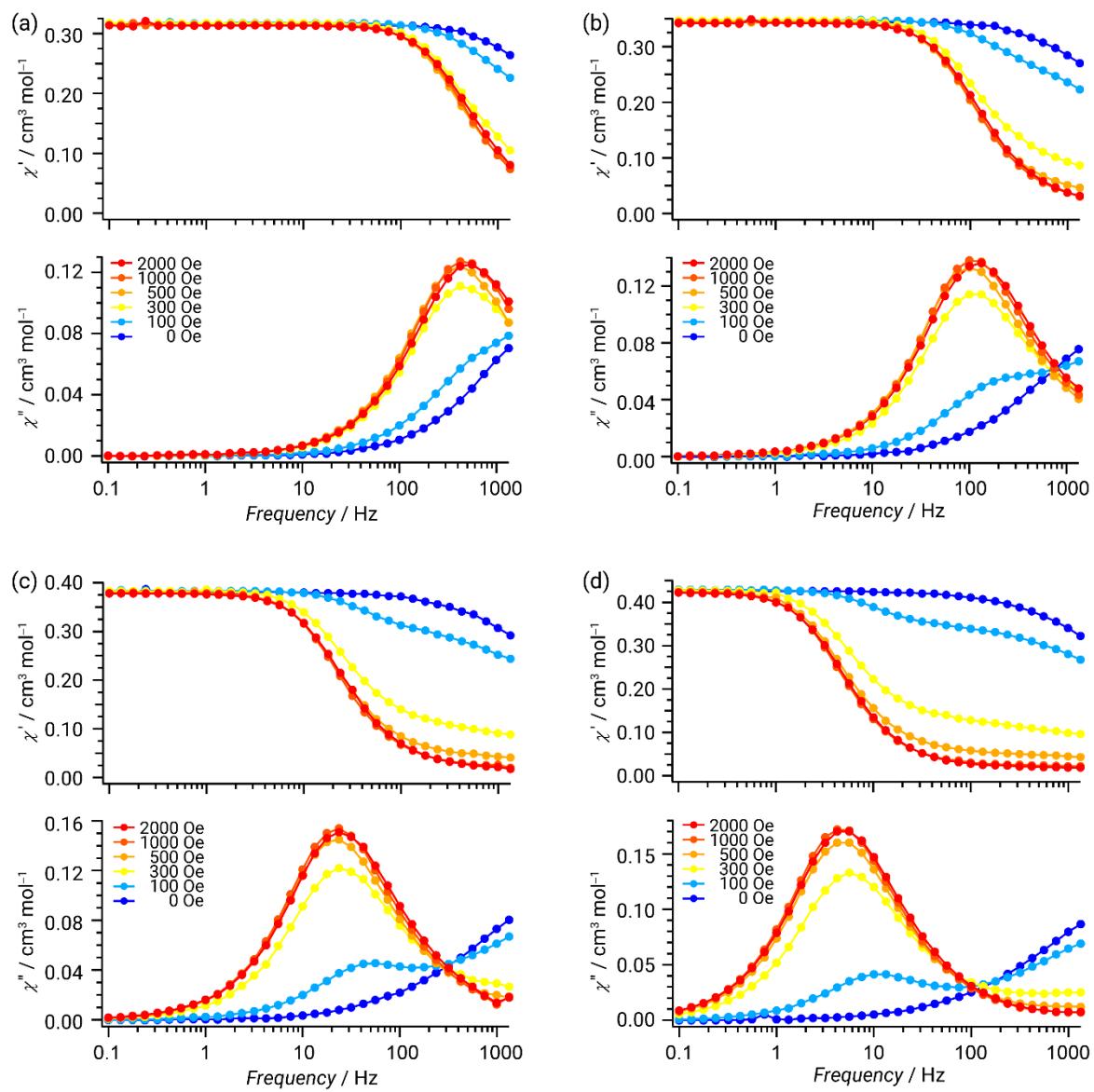
Figure S2. Plots of χ' (top) and χ'' (bottom) against applied ac frequency of **1** at (a) 5.5, (b) 5.0, (c) 4.5, and (d) 4.0 K at the indicated H_{dc}'s.
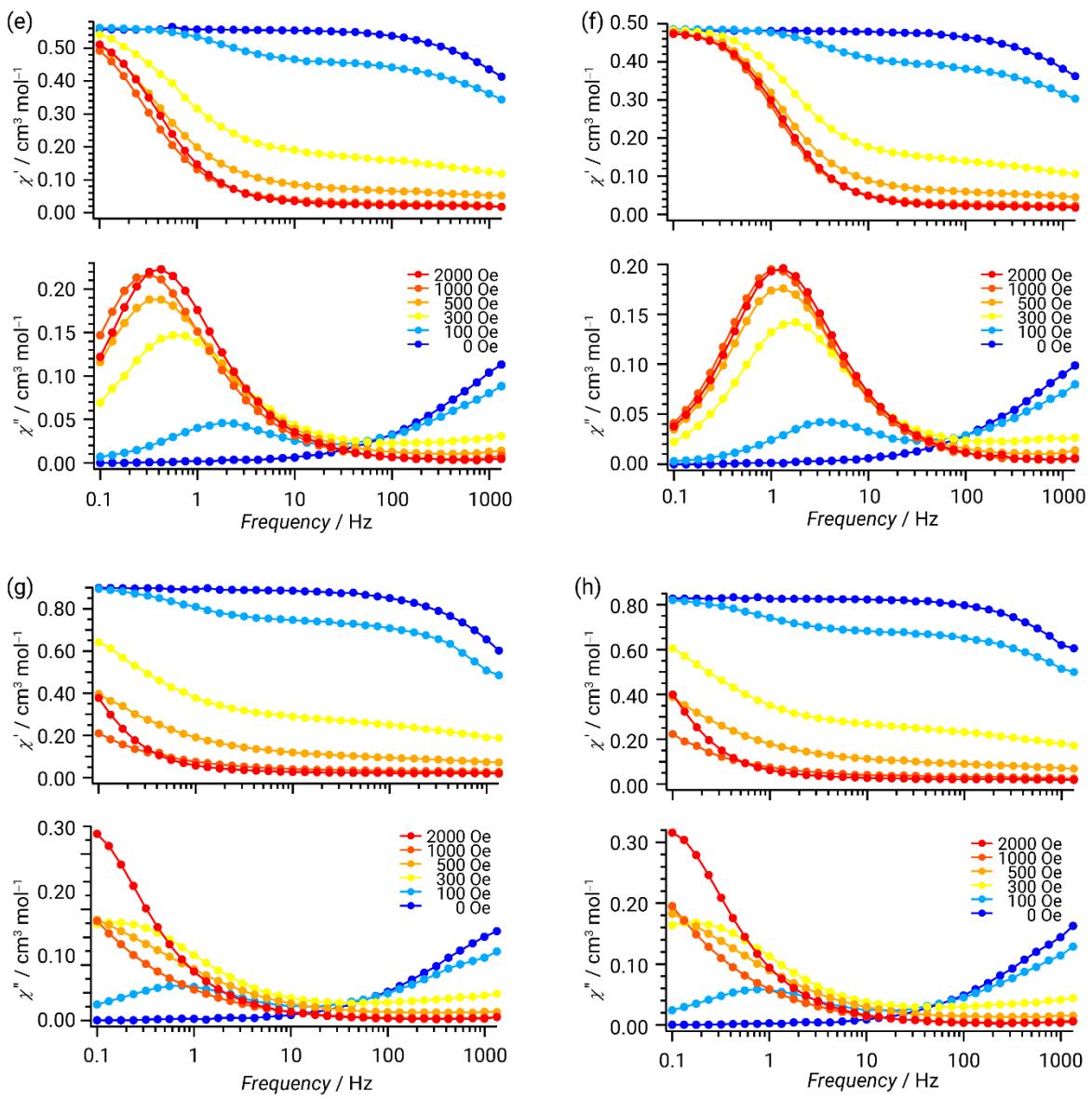
Figure S3. Plots of χ' (top) and χ'' (bottom) against applied ac frequency of **1** at (e) 3.5, (f) 3.0, (g) 2.0, and (h) 1.8 K at the indicated H_{dc}'s.
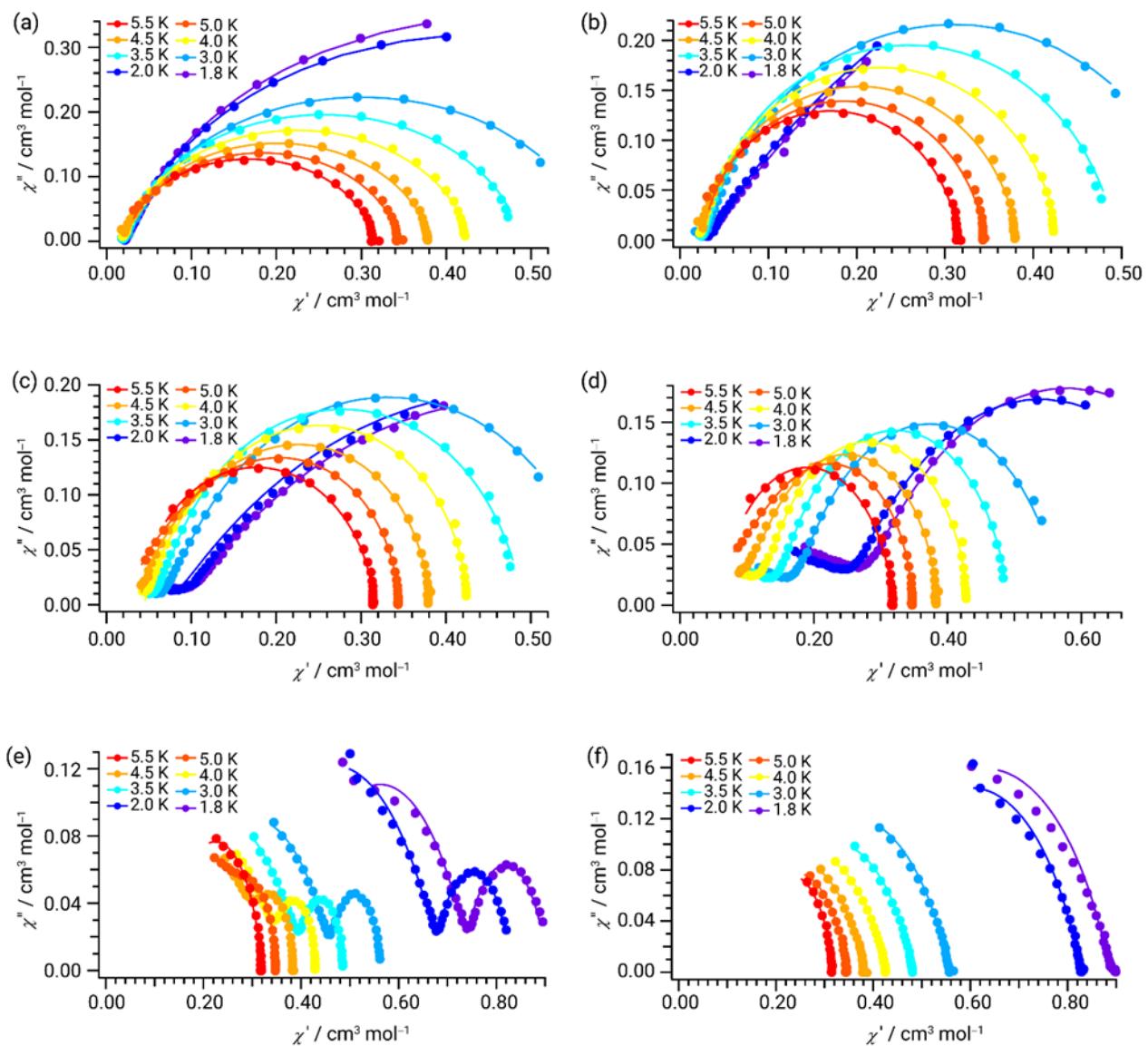
Figure S4. Cole-Cole plots of **1** at H_{dc} of (a) 2000, (b) 1000, (c) 500, (d) 300, (e) 100, and (f) 0 Oe at the indicated temperatures. Results of the fittings are depicted by the solid lines.
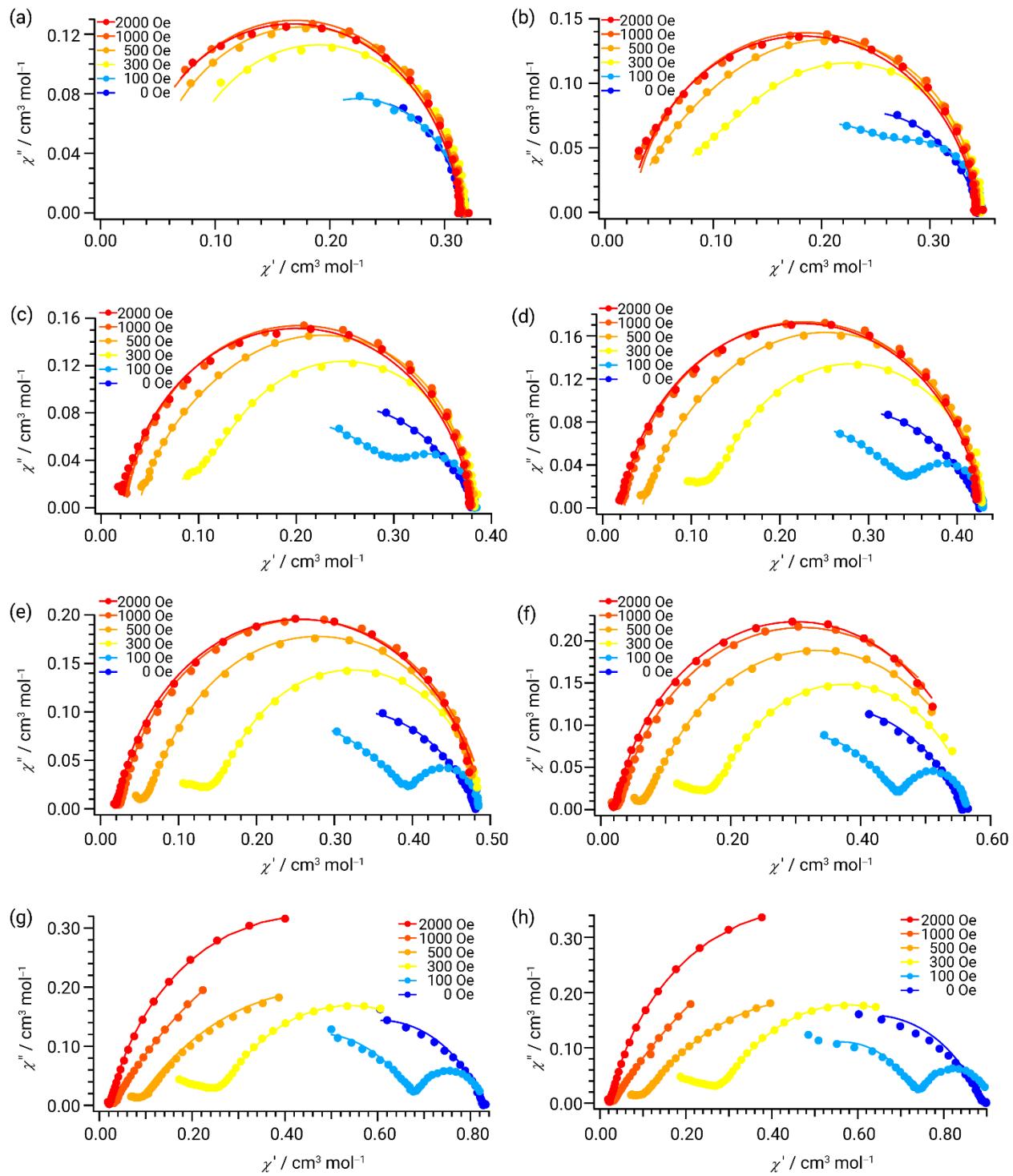
Figure S5. Cole-Cole plots of **1** at (a) 5.5, (b) 5.0, (c) 4.5, (d) 4.0, (e) 3.5, (f) 3.0, (g) 2.0, and (h) 1.8 K at the indicated H_{dc}'s. Results of the fittings are depicted by the solid lines.

Table S1. Parameters obtained from the fitting procedures for **1** at H_{dc} = 2000 Oe.

T / K	χ_t / cm³ mol⁻¹	χ_s / cm³ mol⁻¹	α	τ / s
5.5	0.31	0.020	0.095	2.96×10^{-4}
5.0	0.35	0.022	0.11	1.21×10^{-3}
4.5	0.38	0.021	0.11	5.87×10^{-3}
4.0	0.43	0.021	0.11	2.96×10^{-2}
3.5	0.49	0.021	0.11	1.21×10^{-1}
3.0	0.58	0.022	0.14	3.85×10^{-1}
2.0	0.85	0.023	0.17	1.84
1.8	0.92	0.023	0.16	2.20

Table S2. Parameters obtained from the fitting procedures for **1** at H_{dc} = 1000 Oe.

T / K	χ_t / cm³ mol⁻¹	χ_s / cm³ mol⁻¹	α	τ / s
5.5	0.32	0.025	0.074	3.27×10^{-4}
5.0	0.35	0.025	0.088	1.32×10^{-3}
4.5	0.38	0.025	0.094	6.35×10^{-3}
4.0	0.43	0.024	0.10	3.15×10^{-2}
3.5	0.49	0.026	0.11	1.34×10^{-1}
3.0	0.59	0.027	0.17	5.08×10^{-1}
2.0	1.4	0.029	0.39	1.73×10^{1}
1.8	1.6	0.029	0.42	2.95×10^{1}

Table S3. Parameters obtained from the fitting procedures for **1** at H_{dc} = 500 Oe.

T / K	χ_t / cm^3 mol^{-1}	χ_s / cm^3 mol^{-1}	α	τ / s
5.5	0.32	0.037	0.068	3.62×10^{-4}
5.0	0.34	0.026	0.10	1.78×10^{-3}
4.5	0.38	0.038	0.00006	8.45×10^{-3}
4.0	0.43	0.044	0.017	3.64×10^{-2}
3.5	0.49	−0.002	0.10	1.21×10^{-1}
3.0	0.59	−0.018	0.18	4.08×10^{-1}
2.0	0.89	0.037	0.43	3.33
1.8	0.89	0.045	0.44	3.13

Table S4. Parameters obtained from the fitting procedures for **1** at H_{dc} = 300 Oe.

H / Oe	χ_t / cm^3 mol^{-1}	χ_s / cm^3 mol^{-1}	α_1	τ_1 / s	Weight of τ_1	α_2	τ_2 / s
5.5	0.32	0.062	0.081	3.25×10^{-4}	-	-	-
5.0	0.35	0.049	0.022	1.58×10^{-3}	0.71	0.21	1.80×10^{-4}
4.5	0.38	0.058	0.049	6.36×10^{-3}	0.77	0.36	2.43×10^{-4}
4.0	0.43	0.038	0.063	2.70×10^{-2}	0.72	0.52	1.15×10^{-4}
3.5	0.49	−0.022	0.097	9.47×10^{-2}	0.62	0.652	2.22×10^{-5}
3.0	0.57	−0.094	0.17	2.57×10^{-1}	0.57	0.68	5.80×10^{-6}
2.0	0.82	0.052	0.32	9.43×10^{-1}	0.73	0.53	7.41×10^{-5}
1.8	0.88	0.053	0.33	9.72×10^{-1}	0.72	0.52	7.22×10^{-5}

Table S5. Parameters obtained from the fitting procedures for **1** at H_{dc} = 100 Oe.

H / Oe	χ_t / cm^3 mol^{-1}	χ_s / cm^3 mol^{-1}	α_1	τ_1 / s	Weight of τ_1	α_2	τ_2 / s
5.5	0.329	0.13	0.13	1.28×10^{-4}	-	-	-
5.0	0.35	0.11	0.0059	9.61×10^{-4}	0.31	0.16	6.72×10^{-5}
4.5	0.38	0.059	0.0012	3.82×10^{-3}	0.21	0.034	4.46×10^{-5}
4.0	0.43	0.042	0.0073	1.58×10^{-2}	0.18	0.40	3.58×10^{-5}
3.5	0.49	0.025	0.034	4.57×10^{-2}	0.18	0.41	3.02×10^{-5}
3.0	0.56	0.14	0.089	8.91×10^{-2}	0.24	0.35	6.46×10^{-5}
2.0	0.83	0.25	0.16	2.11×10^{-1}	0.26	0.34	7.64×10^{-5}
1.8	0.90	0.38	0.18	2.35×10^{-1}	0.31	0.29	1.31×10^{-4}

Table S6. Parameters obtained from the fitting procedures for **1** at H_{dc} = 0 Oe.

T / K	χ_t / cm^3 mol^{-1}	χ_s / cm^3 mol^{-1}	α	τ / s
5.5	0.32	0.14	0.097	7.31×10^{-5}
5.0	0.35	0.14	0.19	8.07×10^{-5}
4.5	0.38	0.11	0.28	5.97×10^{-5}
4.0	0.43	0.13	0.30	6.26×10^{-5}
3.5	0.48	0.16	0.29	6.85×10^{-5}
3.0	0.56	0.16	0.31	5.90×10^{-5}
2.0	0.83	0.38	0.27	1.04×10^{-4}
1.8	0.89	0.38	0.29	8.84×10^{-5}

Acknowledgement